JOURNAL OF PETROLOGY | VOLUME 51 | NUMBER 8 | PAGES 1617–1654 | 2010 | doi:10.1093/petrology/egq032

Mineralogical and Geochemical Constraints on the Petrogenesis of Post-collisional Potassic and Ultrapotassic Rocks from Western Yunnan, SW China

XIAO-LONG HUANG[1]*, YAOLING NIU[2], YI-GANG XU[1], LIN-LI CHEN[1] AND QI-JUN YANG[1]

[1]KEY LABORATORY OF ISOTOPE GEOCHRONOLOGY AND GEOCHEMISTRY, GUANGZHOU INSTITUTE OF GEOCHEMISTRY, CHINESE ACADEMY OF SCIENCES, GUANGZHOU 510640, CHINA

[2]DEPARTMENT OF EARTH SCIENCES, DURHAM UNIVERSITY, DURHAM DH1 3LE, UK

RECEIVED JULY 23, 2009; ACCEPTED MAY 20, 2010
ADVANCE ACCESS PUBLICATION JUNE 11, 2010

Paleogene mafic potassic and ultrapotassic volcanic rocks in western Yunnan, China, show a compositional spectrum from potassic trachybasalt to latite (MgO = 6·24–21·8 wt %; SiO_2 = 44·5–59·1 wt %). These rocks have high K_2O (3·07–5·28 wt %), relatively low Na_2O (0·99–4·18 wt %) and high K_2O/Na_2O ratios (0·91–3·89). They share geochemical features such as depletion of Ta, Nb and Ti relative to other similarly incompatible elements and enriched Sr–Nd isotopic compositions (initial $^{87}Sr/^{86}Sr$ of 0·7056–0·7101; $\varepsilon_{Nd}(t)$ of −0·97 to −4·36). The rocks contain abundant olivine and clinopyroxene phenocrysts and xenocrysts. Clinopyroxene phenocrysts show complex zoning patterns (e.g. normal, reverse and oscillatory) and are all characterized by high Mg-number (0·77–0·90), low TiO_2 (0·13–0·29 wt %), Al_2O_3 (0·73–1·68 wt %) and Na_2O (0·22–0·42 wt %) with similar Ti/Al (0·06–0·16) and convex-upward rare earth element (REE) patterns, which are apparently in equilibrium with the host melts. Green cores in some clinopyroxene phenocrysts are characterized by low Mg-number (0·50–0·74) and Ti/Al (<0·05), high Al_2O_3 (1·66–3·63 wt %), Na_2O (0·87–2·17 wt %) and Al^{VI}/Al^{IV} (0·38–0·76), and have chondrite-normalized REE patterns convex-upward from La to Dy and convex-downward from Dy to Lu. We interpret these green cores as xenocrysts from the wall-rocks. All these observations indicate complex magma chamber processes including extensive fractional crystallization, phenocryst accumulation and multiple melt replenishment of similar parental melts with discernible, but limited crustal contamination. All the olivine crystals (Fo = 94–75%) have high CaO contents (>0·1 wt %), indicative of a magmatic origin. The NiO decrease with decreasing Fo is consistent with the effect of fractional crystallization. High-Mg olivines (i.e. those with Fo > 90) are best interpreted as having crystallized from the ultrapotassic magma system (vs mantle olivines) because their spinel inclusions have high Cr-number and low Al_2O_3 and TiO_2, consistent with a magmatic (vs mantle) origin. High fO_2 values calculated from the spinels indicate that the parental melts were oxidized, with high Fe^{3+}/Fe_{Tot} or low Fe^{2+}/Fe_{Tot}, which explains the high Mg-number [= Mg/(Mg + Fe^{2+})] of the melts and the high-Mg olivines. The high fO_2 of the ultrapotassic magmas is probably inherited from their high fO_2 metasomatically enriched lithospheric mantle source. Very low-degree partial melting of metasomatized mantle lithosphere best explains the petrogenesis of these ultrapotassic rocks. The metasomatism may have been relatively recent, probably since the Emeishan flood basalt magmatism in the late Paleozoic in the region. The metasomatic agent may be dominated by a carbonatitic melt, which has imprinted the enriched Sr–Nd–Pb isotopic signature and incompatible element enrichments with conspicuous negative Ta–Nb–Ti anomalies seen in the resulting potassic and ultrapotassic volcanic rocks. Fractionation of Ti-rich amphiboles during melt ascent may have also magnified the geochemical signatures of these rocks.

*Corresponding author. E-mail: xlhuang@gig.ac.cn

© The Author 2010. Published by Oxford University Press. All rights reserved. For Permissions, please e-mail: journals.permissions@oxfordjournals.org

Downloaded from https://academic.oup.com/petrology/article/51/8/1617/1456692 by U.S. Department of Justice user on 17 August 2022

KEY WORDS: *green-core clinopyroxene; high-Mg olivine; mantle metasomatism; potassic and ultrapotassic rocks; Tibetan Plateau*

INTRODUCTION

Potassium-rich igneous rocks with high K_2O (>3 wt %) and high K_2O/Na_2O (>2) are classified as ultrapotassic (Foley *et al.*, 1987) and are characterized by very high concentrations of incompatible elements and volatiles (Foley *et al.*, 1987; Wilson, 1989). Such magmas are volumetrically rare, but nevertheless widespread (Wilson, 1989).

Paleogene ultrapotassic rocks are common within the Greater Tibetan Plateau and its peripheral regions. Although these rocks are important in providing a genetic link between continental collision and continued post-collisional processes (Turner *et al.*, 1996; Chung *et al.*, 1998, 2005; Wang *et al.*, 2001; Guo *et al.*, 2005, 2006; Mo *et al.*, 2006; Zhao *et al.*, 2009), their petrogenesis remains inadequately understood, as reflected by the varying theories and hypotheses presented in recent literature (Chung *et al.*, 1998, 2005; Miller *et al.*, 1999; Wang *et al.*, 2001; Xu *et al.*, 2001*a*; Li *et al.*, 2002; Ding *et al.*, 2003; Guo *et al.*, 2005; Mo *et al.*, 2006; Zhao *et al.*, 2009). These rocks have been considered as the partial melting products of mixed layers of lower crustal and upper mantle materials in the crust–mantle transition zone (Deng & Zhong, 1997; Deng *et al.*, 1998*a*, 1998*b*), the upwelling asthenosphere (Zhang & Xie, 1997) or mantle lithosphere enriched by earlier subduction-derived fluids (e.g. Zhu *et al.*, 1992; Chung *et al.*, 1998; Guo *et al.*, 2005; Mo *et al.*, 2006) or by continental subduction temporally related to the major structures in the eastern segment of the India–Asia collision zone (Wang *et al.*, 2001). The proposed mechanisms that may have triggered melting include convective removal of sub-continental lithospheric mantle (Chung *et al.*, 1998, 2005), Cenozoic subduction of ancient continental lithosphere (Wang *et al.*, 2001; Ding *et al.*, 2003; Guo *et al.*, 2006) and delamination of a lithospheric root (Zhao *et al.*, 2009).

Mantle-derived melts inevitably undergo a variety of modifications during their ascent to the surface. These include melt–rock interactions in the mantle and cooling-induced crystallization, assimilation and mixing deep in the crust and in high-level magma chambers, resulting in the diversity of igneous rocks (Wilson, 1989). Post-collisional ultrapotassic lavas are arguably some of the best examples recording such complex magmatic histories (Barton & Van Bergen, 1981; Conticelli *et al.*, 1997; Conticelli, 1998; Cadoux & Pinti, 2009).

In western Yunnan, Palaeogene potassic and ultrapotassic magmatic rocks are widespread along, and in the vicinity of, the northern part of the Ailao Shan–Red River fault zone (Chung *et al.*, 1998; Guo *et al.*, 2005; Liang *et al.*, 2007). Despite some petrographic variations, these potassic and ultrapotassic rocks share some features in their geochemistry, such as their relative depletion in Nb, Ta and Ti and enriched Sr–Nd isotopic compositions (Chung *et al.*, 1998; Deng *et al.*, 1998*a*; Wang *et al.*, 2001; Xu *et al.*, 2001*a*; Li *et al.*, 2002; Guo *et al.*, 2005; Mo *et al.*, 2006), suggesting that they are products of varying degrees of evolution within similar magmatic systems, developed in the same or similar tectonic settings. An earlier study showed that some mafic ultrapotassic lavas from western Yunnan contain abundant high-Mg olivine and clinopyroxene with green cores, reflecting the complex origin and evolution of these lavas, yet their petrogenesis remains unclear (Xu *et al.*, 2003). In this study, we present new geochemical data, detailed petrographic observations and *in situ* major and trace element analyses of phenocrysts and xenocrysts within the Palaeogene potassic and ultrapotassic volcanic rocks from western Yunnan, and offer new perspectives on the petrogenetic history of these rocks in particular and on the petrogenesis of post-collisional ultrapotassic magmatism in general.

GEOLOGICAL SETTING, SAMPLES AND PETROGRAPHY

The Ailao Shan–Red River fault is a major sinistral strike-slip fault in the region that has displaced the Indochina block to the SE (Tapponnier *et al.*, 1982) by ~500–700 km in response to the India–Asia continental collision (Leloup *et al.*, 1995; Chung *et al.*, 1997). The Ailao Shan–Red River fault links to the NW with the Jinshajiang suture zone, which marks the Late Triassic closure of the Jinshajiang Ocean (Fang, 1993; Mo *et al.*, 1993; Zhang *et al.*, 1996; Wang *et al.*, 2000; Zhong *et al.*, 2000). The Ailao Shan–Red River fault is also the plate boundary separating the Yangtze Craton to the east from the Sanjiang Palaeo-Tethys region in the west (Wang *et al.*, 2000; Fig. 1).

Potassic and ultrapotassic magmatic rocks are most abundant at the northern end of the Ailao Shan–Red River fault zone (Fig. 1), including potassic trachybasalts, shoshonites, olivine latites, latites and trachytes. Some of these rocks have been dated using bulk-rock/mica $^{40}Ar/^{39}Ar$ or zircon U–Pb methods, giving eruption ages between ~40 and 30 Ma (Zhang & Xie, 1997; Chung *et al.*, 1998; Deng *et al.*, 1998*a*; Wang *et al.*, 2001; Guo *et al.*, 2005; Liang *et al.*, 2007). Most of the mafic potassic and ultrapotassic rocks occur as volcanic pipes or dykes closely controlled by subsidiary fractures or faults of the Ailao Shan–Red River fault system, such as those exposed in Wozhong, Wase, Houshan and Midu (Fig. 1b).

The rocks studied are all porphyritic (Fig. 2). The phenocryst assemblage is dominated by olivine and

Downloaded from https://academic.oup.com/petrology/article/51/8/1617/1456692 by U.S. Department of Justice user on 17 August 2022

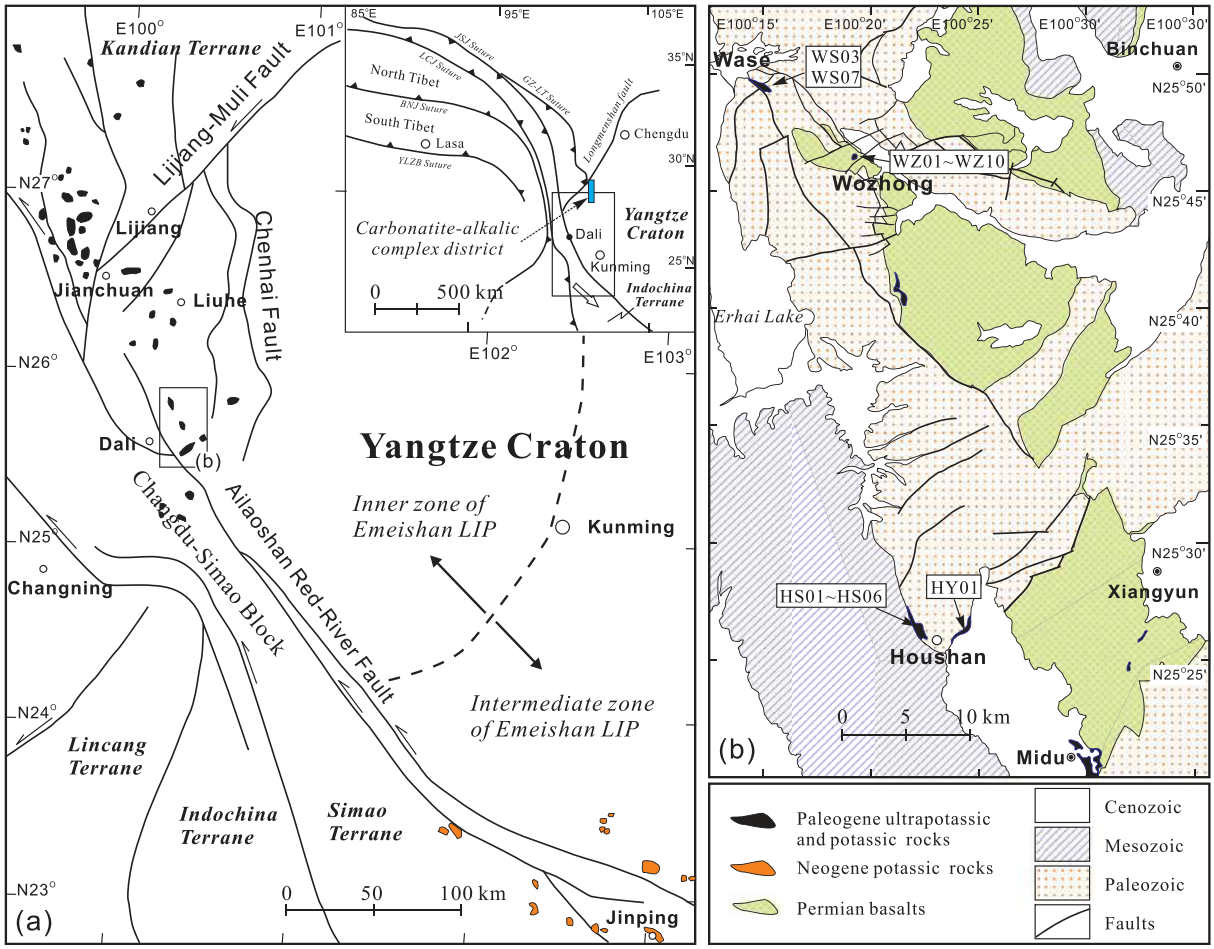

Fig. 1. (a) Tectonic framework of the western Yunnan, Inner Zone and Intermediate Zone of the late Permian Emeishan Large Igneous Province (Emeishan LIP; He *et al.*, 2003) in SW China. Sutures: JSJ, Jinshajiang; GZ-LT, Ganzi Litang; LCJ, Lancangjiang; BNJ, Bangong Nujian; YLZB, Yarlung Zangbo. The inset indicates the regional tectonic context. (b) Simplified geological map of Dali, illustrating the distribution of Cenozoic potassic and ultrapotassic volcanic rocks and sample locations. Modified after Qian & Lu (2000), Xu *et al.* (2003) and the Dali geological map of 1:200 000 scale (BGMR, 1975).

clinopyroxene with rare phlogopite. Microlitic clinopyroxene, sanidine and Fe–Ti oxides are the major phases in the groundmass (Table 1). Olivine phenocrysts are mostly euhedral–subhedral, with varying grain size (0·1–7 mm). Spinel occurs as inclusions (<100 μm) in the olivine phenocrysts from the Wozhong and Houshan samples (Fig. 2a). Clinopyroxene (cpx) phenocrysts occur as single crystals or aggregates (Fig. 2b and c). Most cpx phenocrysts are clean, pale green or colourless, and are partially resorbed in the core (Fig. 2b and c). Some cpx phenocrysts have green cores surrounded by colourless mantles (Fig. 2d). Phlogopite occurs as phenocrysts or inclusions in cpx (Fig. 2b, c and e). Most of the phlogopite crystals are oxidized with fine-grained magnetite aggregates at the rims (Fig. 2b, c and e). Additionally, some shoshonites contain abundant carbonatite veinlets or inclusions in other minerals (Fig. 2f).

SAMPLE PREPARATION AND ANALYTICAL TECHNIQUES

Samples were sawn into slabs and the central parts (>200 g) were used for bulk-rock analyses. The rocks were crushed into small fragments (<0·5 cm in diameter) before being further cleaned and powdered in a corundum mill. Bulk-rock major element oxides were analyzed using X-ray fluorescence (XRF) at the National Taiwan University with analytical uncertainties better than 3% for SiO_2, Al_2O_3, Fe_2O_3, MgO, CaO, Na_2O and K_2O and better than 5% for TiO_2, MnO and P_2O_5. Trace elements were analyzed using inductively coupled plasma-mass spectrometry (ICP-MS) in the Guangzhou Institute of Geochemistry, Chinese Academy of Sciences (GIG-CAS). Repeated runs give <3% RSD (relative standard deviation) for most trace elements analyzed. Sr–Nd isotopic

Downloaded from https://academic.oup.com/petrology/article/51/8/1617/1456692 by U.S. Department of Justice user on 17 August 2022

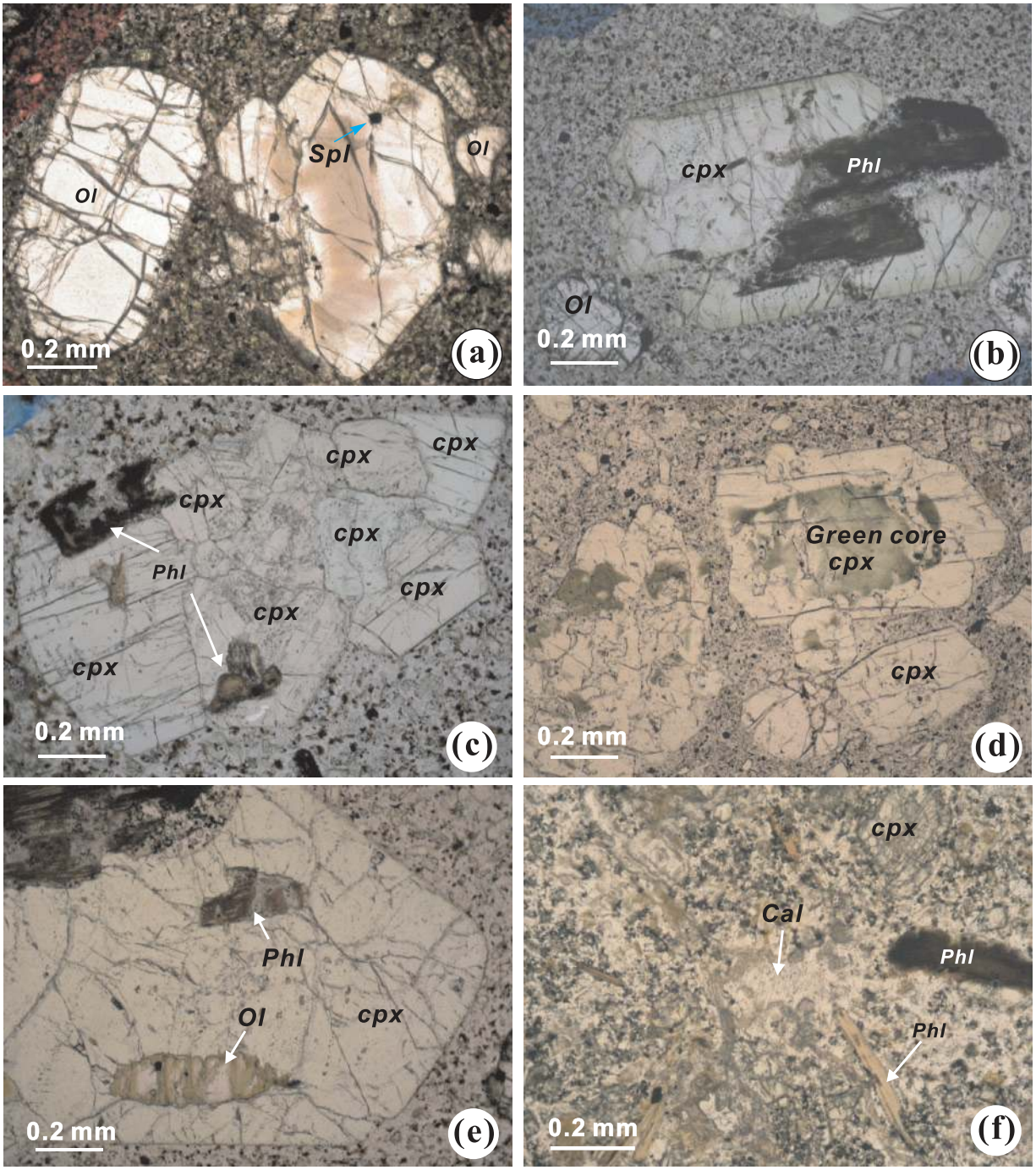

Fig. 2. Petrography of the western Yunnan potassic and ultrapotassic rocks (plane-polarized light): (a) coarse euhedral olivine (Ol) phenocrysts; (b) euhedral clinopyroxene (cpx) phenocrysts with a phlogopite (Phl) xenocryst; (c) cpx phenocryst clots; (d) cpx with green cores and euhedral cpx phenocrysts; (e) large euhedral cpx phenocrysts with Ol and Phl inclusions; (f) calcite (Cal) in the groundmass, Phl xenocryst and cpx phenocrysts.

compositions were measured on a subset of whole-rock samples by multi-collector (MC)-ICP-MS using a Micromass Isoprobe system at the GIG-CAS following the procedure of Wei *et al.* (2002) and Li *et al.* (2004). Reference standards were analyzed along with samples, and give $^{87}Sr/^{86}Sr = 0{\cdot}710243 \pm 14$ (2σ, the last 2 digits) for NBS987 and $^{143}Nd/^{144}Nd = 0{\cdot}512124 \pm 11$ (2σ) for Shin Etsu JNdi-1 ($0{\cdot}512115 \pm 7$; Tanaka *et al.*, 2000). Pb isotopic

Downloaded from https://academic.oup.com/petrology/article/51/8/1617/1456692 by U.S. Department of Justice user on 17 August 2022

Table 1: Samples and brief description

Sample	Rock type	Description
Wozhong (25°46′21″N, 100°19′13″E)		
WZ01	potassic trachybasalt	phenocryst: Ol(18), Cpx(2), Phl(<1); microlitic groundmass: Cpx, Sa, Mt
WZ02	shoshonite	phenocryst: Ol(13), Cpx(3), Phl(<1); microlitic groundmass: Cpx, Sa, Mt
WZ03	shoshonite	phenocryst: Ol(14), Cpx(3), Phl(<1); microlitic groundmass: Cpx, Sa, Mt
WZ04	potassic trachybasalt	phenocryst: Ol(20), Cpx(2), Phl(<1); microlitic groundmass: Cpx, Sa, Mt
WZ05	shoshonite	phenocryst: Ol(6), Cpx(6), Phl(1); microlitic groundmass: Cpx, Sa, Mt
WZ06	shoshonite	phenocryst: Ol(11), Cpx(4), Phl(<1); microlitic groundmass: Cpx, Sa, Mt
WZ07	shoshonite	phenocryst: Ol(3), Cpx(10), Phl(<1); microlitic groundmass: Cpx, Sa, Mt
WZ08	shoshonite	phenocryst: Ol(15), Cpx(2), Phl(<1); microlitic groundmass: Cpx, Sa, Mt
WZ09	shoshonite	phenocryst: Ol(3), Cpx(7), Phl(<1); microlitic groundmass: Cpx, Sa, Mt
WZ10	shoshonite	phenocryst: Ol(5), Cpx(5), Phl(<1); microlitic groundmass: Cpx, Sa, Mt
Houshan (25°26′09″N, 100°22′18″E)		
HS01	shoshonite	phenocryst: Ol(4), Cpx(2), Phl(1); microlitic groundmass: Cpx, Sa, Phl, Mt
HS02	potassic trachybasalt	phenocryst: Ol(10), Cpx(2), Phl(1); microlitic groundmass: Cpx, Sa, Phl, Mt
HS03	shoshonite	phenocryst: Cpx(1), Phl(1); carbonatite-bearing; microlitic groundmass: Cpx, Sa, Phl, Mt
HS04	shoshonite	phenocryst: Ol(4), Cpx(1), Phl(1); microlitic groundmass: Cpx, Sa, Phl, Mt
HS05	potassic trachybasalt	phenocryst: Cpx(1), Phl(1); carbonatite-bearing; microlitic groundmass: Cpx, Sa, Phl, Mt
HS06	latite	phenocryst: Phl(1); microlitic groundmass: Cpx, Sa, Phl, Mt
Houshan (25°26′10″N, 100°24′04″E)		
HY01	latite	phenocryst: Cpx(2), Phl(1); microlitic groundmass: Cpx, Sa, Phl, Mt
Wase (25°49′29″N, 100°14′57″E)		
WS03	olivine latite	phenocryst: Ol(2), Cpx(3), Phl(1); microlitic groundmass: Cpx, Sa, Mt
WS07	shoshonite	phenocryst: Ol(5), Cpx(2), Phl(1); microlitic groundmass: Cpx, Sa, Mt

Ol, olivine; Cpx, clinopyroxene; Sp, spinel; Sa, sanidine; Phl, phlogopite; Mt, Ti-bearing magnetite; proportions in per cent of phenocrysts shown in parentheses (vol. %).

ratios of selected samples were measured on a VG-354 mass spectrometer in the Institute of Geology and Geophysics, Chinese Academy of Sciences following the procedure of Guo *et al.* (2005). During the period of analysis, repeated analyses of international standard NBS981 yielded $^{206}Pb/^{204}Pb = 16{\cdot}9506 \pm 2$ (2σ), $^{207}Pb/^{204}Pb = 15{\cdot}5072 \pm 6$ (2σ) and $^{208}Pb/^{204}Pb = 36{\cdot}6786 \pm 4$ (2σ).

For $^{40}Ar/^{39}Ar$ dating, the rock sample was sawn into slabs and the central part was used. After crushed to 40–60 mesh size in a steel mortar with phenocrysts removed under a binocular microscope, the sample was cleaned with acetone followed by further cleaning with deionized water in an ultrasonic bath for 20 min. The cleaned sample was then dried at ~100°C. Each sample was wrapped in aluminum foil and sealed in a quartz ampoule that was evacuated afterwards before being irradiated for 90 h in the Mianyang reactor (Sichuan, China). The *J*-values for the samples were determined by using ZBH-2506 Biotite (132 Ma) as flux monitors. To obtain *J*-values for unknown samples, the monitor ZBH-2506 was packed between every four samples in quartz tubes, each tube containing four packets of ZBH-2506. Based on the *J*-values and the positions of ZBH-2506 in the sample tube, a regression line was obtained for each sample tube, and then the *J*-values for the unknown samples were calculated by interpolation from the regression line. A *J*-value uncertainty of 0·15% (1σ) was considered in the reported ages. The $^{40}Ar/^{39}Ar$ dating was carried out using a GV5400 mass spectrometer at the GIG-CAS. Argon gas was extracted from the sample by step-heating (50 s per step) using a MIR10 CO_2 continuing laser. The background of the sample holder is lower than 2 mV pre-experiment and 4–6 mV during the experiment after a 5 min evacuation, and the signal of the sample is mostly controlled within the range of 40–200 mV. The ArArCALC program (v.2.2; Koppers, 2002) was used for raw data reduction and age calculation.

Downloaded from https://academic.oup.com/petrology/article/51/8/1617/1456692 by U.S. Department of Justice user on 17 August 2022

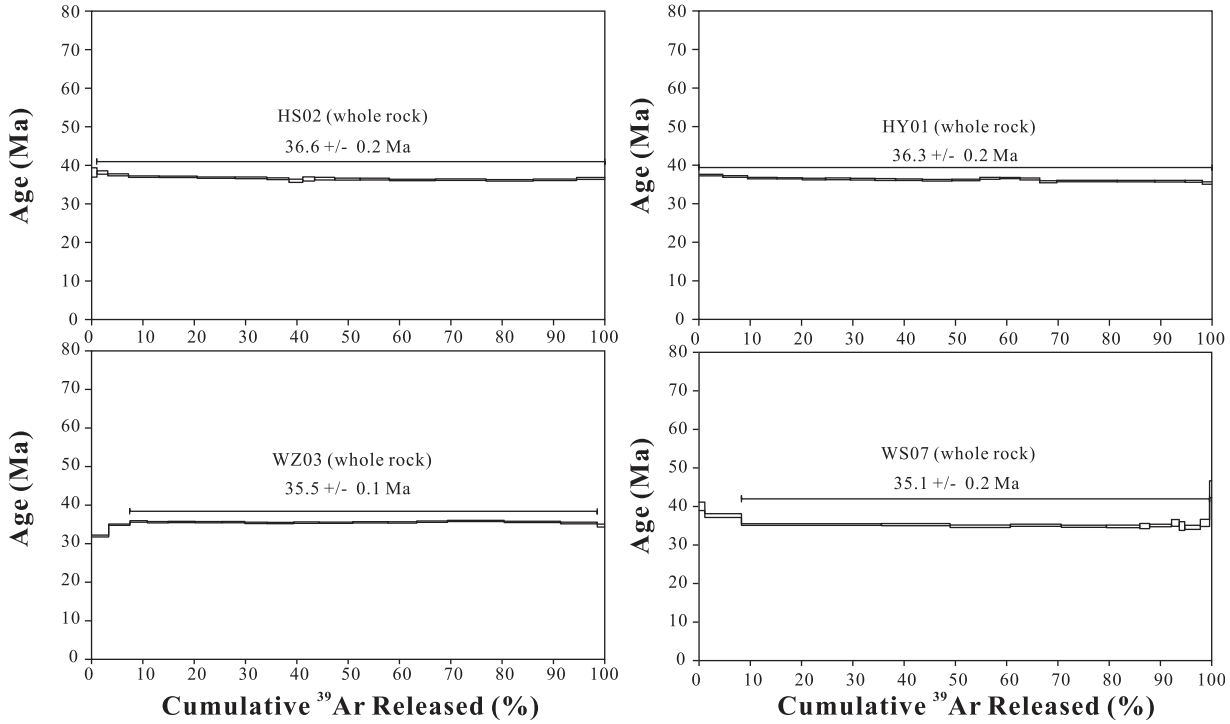

Fig. 3. Whole-rock $^{40}Ar/^{39}Ar$ plateau age spectra for four representative samples (see Table 2 for data).

Major element analysis and back-scattered electron (BSE) imaging of minerals were carried out using a JEOL JXA-8100 Superprobe at the GIG-CAS. The operating conditions are: 15 kV accelerating voltage, 20 nA beam current, 1–2 μm beam diameter, and 10 s peak counting time for most elements (30 s for Ca and Ni in olivine, 7 s for Na and 8 s for K). The data reduction was carried out using ZAF correction.

In situ trace element analysis of cpx was carried out using the laser-ablation (LA)-ICP-MS technique (using an Agilent 7500a ICP-MS system coupled with a GeoLas193 nm ArF-excimer laser sampler) in the State Key Laboratory of Geological Processes and Mineral Resources, China University of Geosciences in Wuhan. A spot size of 60 μm and repetition rate of 8 Hz were applied during analysis. Calibration was carried out externally using NIST SRM 610 with Ca as an internal standard to correct for drift if any. Repeated analyses of the USGS rock standards (BHVO-2G and BCR-2G) indicate precision and accuracy both better than 4% for most elements analyzed. For cpx, the relative standard deviations (RSDs) of rare earth elements (REE), Y, Zr, Hf, Sr, Pb, Sc, Ti and V are better than 6%, and those of Cr, Co, Ni, Ba, Th and U are 3–15%. RSDs of Nb, Ta, Rb and Cs range from 3% to 20%, and from 20% to 50% for low-concentration samples. Analytical details have been given by Liu *et al.* (2008).

RESULTS

$^{40}Ar/^{39}Ar$ age data

Four samples from Wozhong, Wase and Houshan were selected for dating, including one trachybasalt, two shoshonites and one latite. The plateau ages of all samples were obtained from more than 90% cumulative ^{39}Ar released (Fig. 3; Table 2). All the steps included in the plateau ages are strongly enriched in radiogenic ^{40}Ar because of the high K contents of the rocks. At Houshan, the age measured on the bulk-rock sample of potassic trachybasalt is 36·6 ± 0·2 Ma (HS02), which is the same as that of the latite (36·3 ± 0·2 Ma, HY01). The shoshonite samples from Wozhong and Wase give slightly younger plateau ages of 35·5 ± 0·1 Ma (WZ03) and 35·1 ± 0·2 Ma (WS07), respectively. Therefore, the $^{40}Ar/^{39}Ar$ ages of the western Yunnan mafic potassic and ultrapotassic volcanic rocks are essentially the same as the ages of the trachytes determined using the bulk-rock–mica $^{40}Ar/^{39}Ar$ or zircon U–Pb methods (Zhang & Xie, 1997; Chung *et al.*, 1998; Wang *et al.*, 2001; Liang *et al.*, 2007), which represent the timing of the early stage potassic magmatism in the Ailao Shan–Red River fault zone in western Yunnan (42–24 Ma; Wang *et al.*, 2001) and the post-collisional potassic and ultrapotassic magmatism on the Greater Tibetan Plateau in response to the India–Asia collision and continued convergence (Chung *et al.*, 1998).

Downloaded from https://academic.oup.com/petrology/article/51/8/1617/1456692 by U.S. Department of Justice user on 17 August 2022

Table 2: $^{40}Ar/^{39}Ar$ dating of the western Yunnan potassic and ultrapotassic rocks

Incremental heating		$^{36}Ar(a)$	$^{38}Ar(cl)$	$^{39}Ar(k)$	$^{40}Ar(r)$	Age (Ma)	±1σ	$^{40}Ar(r)$ (%)	$^{39}Ar(k)$ (%)
Steps	Laser (%)								
WZ03 (whole-rock); J = 0·00955; T1 = 35·5 ± 0·1 Ma; T2 = 35·4 ± 0·1 Ma; T3 = 36·2 ± 0·3 Ma; T4 = 36·1 ± 0·3 Ma									
05M2047B	4·0	0·053	0·043	39·873	74·568	31·94	±0·25	82·50	3·29
05M2047C	5·0	0·020	0·028	50·096	102·412	34·88	±0·17	94·47	4·14
05M2047D	6·0	0·008	0·016	41·068	85·974	35·71	±0·19	97·11	3·39
05M2047E	7·0	0·012	0·022	49·289	102·605	35·51	±0·17	96·52	4·07
05M2047G	8·5	0·014	0·039	63·631	132·736	35·59	±0·17	96·82	5·25
05M2047H	10·0	0·016	0·041	63·183	131·587	35·53	±0·16	96·41	5·22
05M2047I	11·5	0·016	0·032	53·944	112·390	35·54	±0·17	95·77	4·45
05M2047J	13·0	0·019	0·032	52·988	109·779	35·35	±0·18	95·17	4·38
05M2047L	14·5	0·017	0·042	62·753	129·852	35·30	±0·16	96·10	5·18
05M2047M	16·0	0·016	0·039	59·509	123·523	35·41	±0·18	96·19	4·91
05M2047N	17·5	0·021	0·056	79·668	165·229	35·38	±0·16	96·31	6·58
05M2047O	19·0	0·020	0·055	83·479	173·635	35·48	±0·16	96·70	6·89
05M2047Q	21·0	0·015	0·051	67·635	140·561	35·45	±0·18	96·87	5·58
05M2047R	25·0	0·014	0·053	72·619	151·827	35·67	±0·17	97·26	6·00
05M2047S	30·0	0·022	0·086	133·744	281·017	35·84	±0·16	97·64	11·04
05M2047T	35·0	0·024	0·098	133·170	277·936	35·60	±0·17	97·40	11·00
05M2047V	40·0	0·024	0·089	86·715	179·481	35·31	±0·21	96·05	7·16
05M2047W	45·0	0·009	0·013	17·646	35·832	34·65	±0·37	92·82	1·46
HS02 (whole-rock); J = 0·00887; T1 = 36·6 ± 0·2 Ma; T2 = 36·6 ± 0·1 Ma; T3 = 35·9 ± 0·4 Ma; T4 = 35·8 ± 0·4 Ma									
05M2048B	4·0	0·079	0·004	7·008	16·892	38·15	±1·21	42·10	0·98
05M2048C	5·0	0·040	0·000	14·980	36·098	38·14	±0·43	75·20	2·10
05M2048D	6·0	0·046	0·000	28·845	68·408	37·54	±0·26	83·25	4·05
05M2048E	7·5	0·046	0·000	42·735	100·050	37·07	±0·19	88·08	6·00
05M2048G	9·5	0·041	0·006	52·647	123·096	37·02	±0·19	90·96	7·39
05M2048H	11·5	0·042	0·010	52·312	121·603	36·81	±0·18	90·61	7·35
05M2048I	13·5	0·040	0·013	44·367	103·004	36·76	±0·22	89·62	6·23
05M2048J	15·0	0·029	0·005	30·608	70·611	36·53	±0·23	89·26	4·30
05M2048L	17·0	0·021	0·001	19·139	43·497	35·99	±0·41	87·34	2·69
05M2048M	19·0	0·017	0·000	16·426	37·825	36·47	±0·54	88·50	2·31
05M2048N	22·0	0·021	0·006	27·853	64·287	36·55	±0·35	91·09	3·91
05M2048O	26·0	0·029	0·008	35·726	82·201	36·44	±0·26	90·59	5·02
05M2048Q	32·0	0·029	0·015	40·327	92·800	36·44	±0·23	91·40	5·66
05M2048R	40·0	0·050	0·023	63·857	145·994	36·21	±0·18	90·79	8·97
05M2048S	50·0	0·053	0·025	70·100	160·631	36·29	±0·19	91·06	9·85
05M2048T	60·0	0·042	0·027	65·753	149·913	36·11	±0·20	92·33	9·24
05M2048V	70·0	0·027	0·025	60·001	137·356	36·25	±0·20	94·50	8·43
05M2048W	80·0	0·012	0·010	39·312	90·888	36·61	±0·24	96·04	5·52
HY01 (whole-rock); J = 0·00898; T1 = 36·3 ± 0·2 Ma; T2 = 36·2 ± 0·1 Ma; T3 = 36·2 ± 0·3 Ma; T4 = 36·0 ± 0·3 Ma									
05M2046C	5·5	0·028	0·091	32·034	74·684	37·38	±0·20	89·91	4·61
05M2046D	6·5	0·002	0·054	33·683	77·765	37·02	±0·21	99·33	4·84
05M2046E	7·5	0·004	0·054	39·874	90·982	36·60	±0·19	98·64	5·73
05M2046G	8·5	0·000	0·043	34·373	78·321	36·55	±0·16	99·93	4·94
05M2046H	9·5	0·003	0·037	31·548	71·518	36·36	±0·21	98·60	4·54

(continued)

Downloaded from https://academic.oup.com/petrology/article/51/8/1617/1456692 by U.S. Department of Justice user on 17 August 2022

Table 2: Continued

Incremental heating		^{36}Ar(a)	^{38}Ar(cl)	^{39}Ar(k)	^{40}Ar(r)	Age (Ma)	±1σ	^{40}Ar(r) (%)	^{39}Ar(k) (%)
Steps	Laser (%)								
05M2046I	10·5	0·004	0·035	33·775	76·695	36·42	±0·23	98·57	4·86
05M2046J	11·5	0·005	0·040	33·115	74·979	36·32	±0·22	97·99	4·76
05M2046L	12·5	0·001	0·032	27·986	63·223	36·24	±0·24	99·26	4·02
05M2046M	13·5	0·002	0·044	36·428	82·213	36·20	±0·20	99·24	5·24
05M2046N	14·5	0·003	0·041	39·902	89·680	36·05	±0·21	98·79	5·74
05M2046O	15·5	0·004	0·038	37·972	85·500	36·12	±0·20	98·57	5·46
05M2046Q	16·5	0·000	0·026	27·189	61·947	36·54	±0·24	99·79	3·91
05M2046R	18·0	0·000	0·025	27·303	62·321	36·61	±0·15	99·93	3·93
05M2046S	20·0	0·003	0·023	26·787	60·764	36·38	±0·25	98·64	3·85
05M2046T	25·0	0·003	0·017	23·084	51·315	35·66	±0·27	98·03	3·32
05M2046V	33·0	0·009	0·078	82·154	183·593	35·85	±0·18	98·48	11·81
05M2046W	41·0	0·009	0·048	50·622	113·054	35·83	±0·19	97·69	7·28
05M2046X	50·0	0·006	0·037	41·484	92·582	35·80	±0·21	97·98	5·96
05M2046Y	60·0	0·003	0·017	23·138	51·597	35·77	±0·25	97·97	3·33
05M2046Z	70·0	0·004	0·008	13·110	28·862	35·32	±0·32	95·93	1·88
WS07 (whole-rock); J = 0·0111; T1 = 35·1 ± 0·2 Ma; T2 = 35·4 ± 0·2 Ma; T3 = 35·0 ± 0·2 Ma; T4 = 35·0 ± 0·2 Ma									
05M2113B	3·0	0·009	0·003	3·576	7·234	40·03	±1·10	73·54	1·12
05M2113C	4·0	0·026	0·000	22·871	43·458	37·63	±0·48	84·67	7·15
05M2113D	5·0	0·028	0·000	87·376	155·671	35·31	±0·22	94·73	27·31
05M2113E	5·3	0·007	0·001	42·873	76·339	35·29	±0·28	97·02	13·40
05M2113G	5·8	0·002	0·003	37·640	66·209	34·86	±0·33	98·67	11·76
05M2113H	6·5	0·001	0·006	31·712	56·212	35·13	±0·27	98·98	9·91
05M2113I	7·5	0·004	0·009	28·222	49·640	34·86	±0·28	97·27	8·82
05M2113J	9·0	0·004	0·009	20·795	36·538	34·82	±0·34	96·42	6·50
05M2113L	9·0	0·001	0·001	6·149	10·834	34·92	±0·66	96·42	1·92
05M2113M	12·0	0·003	0·014	13·700	24·238	35·06	±0·32	96·69	4·28
05M2113N	12·5	0·002	0·005	4·823	8·695	35·73	±0·88	94·70	1·51
05M2113O	13·5	0·001	0·004	3·396	5·983	34·92	±1·13	94·07	1·06
05M2113Q	19·0	0·001	0·014	9·723	16·966	34·59	±0·54	97·34	3·04
05M2113R	30·0	0·010	0·008	5·806	10·471	35·73	±0·93	77·59	1·81
05M2113S	50·0	0·001	0·002	1·305	2·934	44·45	±2·20	90·80	0·41

T1, Weighted plateau age; T2, total fusion age; T3, normal isochron age; T4, inverse isochron.

Bulk-rock geochemical data

Major and trace elements

The mafic potassic and ultrapotassic rocks vary from low-SiO_2 and high-MgO potassic trachybasalts to high-SiO_2 and low-MgO latites (MgO = 6·24–21·8 wt %; SiO_2 = 44·5–59·1 wt %; Fig. 4a and Table 3). On a total alkalis–silica (TAS) diagram (Fig. 4b), most of the samples belong to the alkali series, ranging from potassic trachybasalts to shoshonites, olivine latites and latites. The rocks have high K_2O (3·07–5·28 wt %; Table 3) and relatively low Na_2O (0·99–4·18 wt %; Table 3) contents with high K_2O/Na_2O (0·91–3·89). The variable K_2O and Na_2O contents of the Houshan rocks (Fig. 4b–d) are probably caused by alteration in some samples as suggested by their high and variable loss on ignition (LOI; 1·47–11·04 wt %; Table 3). They are transitional between Group I (anorogenic lamproites) and III (orogenic ultrapotassic series) potassic rocks using the classification scheme of Foley *et al.* (1987; see Fig. 4e). However, as lamproites (Group I) are characterized by high K_2O/Al_2O_3 (>0·6) and high TiO_2 (2–8 wt %) (Foley *et al.*, 1987), our samples are clearly members of the orogenic ultrapotassic series with low TiO_2 (<1 wt %; Table 3) and K_2O/Al_2O_3 (0·28–0·50). As a whole, the western Yunnan mafic potassic and

Downloaded from https://academic.oup.com/petrology/article/51/8/1617/1456692 by U.S. Department of Justice user on 17 August 2022

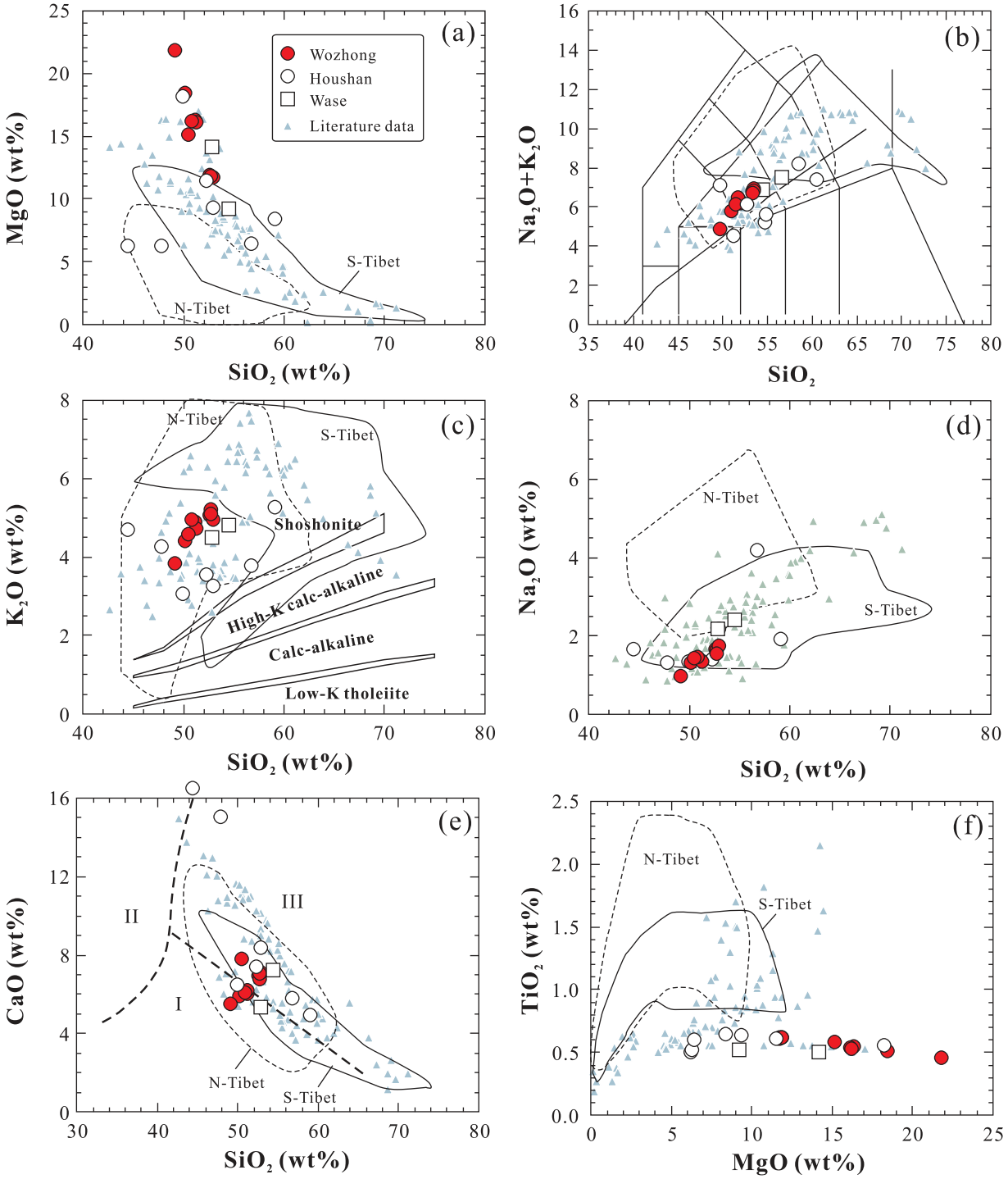

Fig. 4. Variation diagrams for representative major element oxides: (a) SiO_2 vs MgO; (b) TAS diagram (Le Maitre *et al.*, 1989); (c, d, e) K_2O, Na_2O and CaO vs SiO_2, respectively; in (e), Group I, II and III potassic rock fields are from Foley *et al.* (1987); (f) MgO vs TiO_2. Literature data for western Yunnan (including Ailao Shan–Red River and western Yangtze craton), North Tibet and South Tibet potassic rocks are shown for comparison. Data sources: Western Yunnan: Zhu *et al.* (1992), Deng *et al.* (1998*b*), Wang *et al.* (2001), Xu *et al.* (2001*a*), Li *et al.* (2002), Guo *et al.* (2005) and this study; North Tibet: Turner *et al.* (1996) and Ding *et al.* (2003); South Tibet, Turner *et al.* (1996), Miller *et al.* (1999), Ding *et al.* (2003), Guo *et al.* (2006) and Zhao *et al.* (2009).

Downloaded from https://academic.oup.com/petrology/article/51/8/1617/1456692 by U.S. Department of Justice user on 17 August 2022

Table 3: Major (wt %) and trace element (ppm) data for the western Yunnan mafic potassic and ultrapotassic rocks

Sample:	WZ01	WZ02	WZ03	WZ04	WZ05	WZ06	WZ07	WZ08	WZ09	WZ10	WS03	WS07	HS01	HS02	HS03	HS04	HS05	HS06	HY01
SiO_2	50·20	51·20	51·24	49·10	52·70	50·87	52·96	50·53	52·78	52·62	54·47	52·84	52·28	49·96	47·85	52·92	44·48	59·05	56·77
TiO_2	0·51	0·55	0·54	0·46	0·62	0·53	0·61	0·58	0·62	0·62	0·52	0·50	0·61	0·56	0·51	0·64	0·52	0·65	0·60
Al_2O_3	9·18	10·07	10·00	8·12	11·52	9·89	11·59	9·68	11·42	11·36	10·80	10·25	10·41	9·42	9·91	11·75	10·30	11·42	13·33
Fe_2O_3	8·06	7·86	7·91	8·42	7·91	7·87	7·68	7·94	8·02	8·01	6·19	6·69	7·82	7·99	4·83	7·29	4·38	5·30	5·66
MnO	0·13	0·13	0·13	0·14	0·14	0·13	0·13	0·13	0·14	0·14	0·14	0·12	0·13	0·14	0·36	0·12	0·43	0·08	0·10
MgO	18·43	16·33	16·16	21·82	11·71	16·22	11·71	15·12	11·84	11·90	9·20	14·17	11·50	18·21	6·24	9·33	6·26	8·39	6·43
CaO	5·89	6·01	6·20	5·52	6·76	6·11	7·10	7·83	7·04	6·93	7·25	5·34	7·39	6·49	15·02	8·38	16·25	4·96	5·79
Na_2O	1·31	1·37	1·36	0·99	1·65	1·46	1·76	1·44	1·56	1·67	2·40	2·18	1·42	1·35	1·31	2·19	1·66	1·93	4·18
K_2O	4·43	4·91	4·73	3·85	5·23	4·95	4·97	4·59	5·10	5·08	4·83	4·51	3·57	3·07	4·26	3·26	4·70	5·28	3·80
P_2O_5	0·42	0·45	0·45	0·37	0·43	0·45	0·45	0·43	0·44	0·44	0·46	0·43	0·43	0·40	0·40	0·54	0·49	0·60	0·34
LOI	0·98	0·66	0·69	0·95	0·36	0·59	0·48	0·81	0·28	0·36	3·52	2·68	3·03	2·71	9·86	2·56	11·04	1·47	2·54
Total	99·54	99·54	99·41	99·74	99·03	99·07	99·44	99·08	99·24	99·13	99·78	99·71	98·59	100·30	100·55	98·98	100·51	99·13	99·54
Mg-no.	0·819	0·805	0·802	0·837	0·746	0·803	0·751	0·791	0·745	0·747	0·747	0·808	0·745	0·819	0·719	0·717	0·739	0·759	0·693
Sc	18·0	17·5	18·1	16·6	18·1	16·0	21·2	20·4	22·4	23·3	15·3	13·9	21·4	19·0	18·0	24·3	15·7	14·7	13·5
V	121	125	126	108	115	107	127	123	146	143	101	93·5	125	118	102	158	95·7	90·8	88·6
Cr	1657	1464	1495	1626	818	1270	954	1153	1055	1039	1020	942	1663	1544	945	1258	348	373	477
Co	51·4	45·5	45·9	64·3	30·7	40·9	32·8	41·9	36·6	36·8	41·1	39·2	48·4	46·9	19·6	40·6	21·4	25·8	26·0
Ni	667	554	557	852	197	492	228	411	234	237	600	519	562	580	234	376	152	256	221
Rb	135	227	213	155	207	201	212	177	233	231	183	175	106	45	194	207	191	345	138
Ba	1224	1323	1325	1116	1137	1408	1173	1171	1089	1161	1538	1317	1379	1328	1006	1395	1309	1566	2439
Sr	970	1031	1043	868	678	994	750	834	768	784	1227	1017	1021	1000	601	951	839	1206	1244
Y	16·0	16·7	16·8	14·8	17·7	16·4	18·2	17·2	19·0	19·2	16·0	14·7	18·3	17·1	21·2	28·0	24·7	18·8	17·8
Zr	97	122	112	91	110	101	112	101	120	117	141	131	110	107	103	135	116	181	182
Hf	2·63	3·03	2·83	2·41	2·99	2·93	3·04	2·81	2·87	3·02	3·73	3·50	2·83	2·62	2·70	3·31	3·12	4·73	4·61
Nb	5·17	6·03	5·51	4·87	5·79	5·44	5·86	5·85	6·00	5·96	6·29	6·04	5·41	5·04	6·30	6·88	6·00	8·57	11·3
Ta	0·32	0·38	0·34	0·30	0·39	0·36	0·40	0·39	0·38	0·40	0·39	0·39	0·34	0·31	0·39	0·44	0·42	0·61	0·73
Pb	15·9	17·3	23·0	12·2	22·3	21·2	21·9	18·7	22·4	22·4	29·8	30·9	20·0	19·9	18·8	20·4	18·4	22·7	17·8
Th	8·20	9·63	8·87	7·68	8·75	9·36	8·66	7·94	8·53	8·40	9·84	9·19	7·01	6·74	8·09	7·96	10·8	10·2	15·0
U	3·01	3·64	3·29	2·82	3·28	3·58	3·20	3·00	3·08	3·11	3·27	2·94	2·29	2·17	3·12	3·17	4·01	4·17	4·49
La	23·2	24·2	23·7	19·9	19·0	21·4	20·6	20·5	22·1	21·4	30·9	28·3	21·5	19·7	22·8	25·7	29·6	31·5	48·5
Ce	44·5	46·5	45·5	38·7	37·6	42·1	40·8	40·2	42·9	41·8	63·6	58·1	42·5	39·7	42·9	47·6	55·8	61·9	93·1
Pr	5·61	5·80	5·76	4·94	4·71	5·42	5·22	5·12	5·40	5·37	7·75	7·18	5·54	5·19	5·40	6·27	7·05	7·55	9·88
Nd	22·8	23·9	23·8	20·1	19·7	22·1	21·2	21·5	22·0	22·4	31·6	29·1	23·5	21·7	22·2	26·4	29·7	31·3	37·3
Sm	4·79	4·88	4·86	4·16	4·27	4·65	4·58	4·60	4·75	4·83	6·11	5·81	4·98	4·65	4·58	5·56	6·24	6·35	6·55
Eu	1·33	1·39	1·38	1·17	1·17	1·35	1·29	1·31	1·32	1·36	1·43	1·38	1·45	1·31	1·22	1·57	1·68	1·79	1·99
Gd	4·03	4·16	4·10	3·51	3·87	4·13	4·14	4·15	4·20	4·42	5·08	4·75	4·40	4·04	4·18	5·19	5·47	5·40	5·24
Tb	0·57	0·56	0·57	0·48	0·57	0·57	0·60	0·58	0·61	0·63	0·65	0·63	0·62	0·57	0·60	0·74	0·75	0·72	0·67
Dy	2·94	3·04	3·02	2·67	3·11	3·06	3·28	3·11	3·36	3·42	3·49	3·24	3·31	3·04	3·29	3·91	3·89	3·63	3·32
Ho	0·55	0·57	0·58	0·49	0·61	0·57	0·64	0·59	0·64	0·66	0·65	0·58	0·63	0·57	0·64	0·78	0·76	0·65	0·60
Er	1·50	1·55	1·57	1·33	1·69	1·57	1·78	1·63	1·81	1·81	1·63	1·55	1·69	1·56	1·79	2·10	2·09	1·68	1·60
Tm	0·23	0·23	0·24	0·21	0·26	0·24	0·27	0·25	0·27	0·27	0·24	0·23	0·25	0·24	0·27	0·30	0·31	0·24	0·24
Yb	1·37	1·44	1·45	1·25	1·62	1·46	1·68	1·52	1·69	1·72	1·61	1·48	1·54	1·45	1·67	1·80	1·98	1·48	1·41
Lu	0·22	0·23	0·23	0·21	0·26	0·24	0·27	0·24	0·27	0·28	0·24	0·24	0·25	0·23	0·27	0·29	0·33	0·23	0·23
Eu/Eu*	0·90	0·92	0·92	0·92	0·86	0·93	0·89	0·90	0·89	0·89	0·77	0·78	0·93	0·90	0·84	0·88	0·86	0·91	1·01
$[Nb/La]_N$	0·21	0·24	0·22	0·24	0·29	0·25	0·27	0·27	0·26	0·27	0·20	0·21	0·24	0·25	0·27	0·26	0·20	0·26	0·26
Nb/Ta	16·0	15·9	16·3	16·3	14·8	15·0	14·7	15·0	15·8	15·0	16·1	15·6	16·1	16·3	16·0	15·7	14·1	14·0	15·4
Nb/Zr	0·053	0·050	0·049	0·054	0·053	0·054	0·052	0·058	0·050	0·051	0·045	0·046	0·049	0·047	0·061	0·051	0·052	0·047	0·062
Ti/Ti*	0·29	0·31	0·31	0·31	0·39	0·31	0·35	0·34	0·35	0·34	0·24	0·24	0·33	0·33	0·35	0·30	0·29	0·28	0·27

$Ti/Ti^* = 2Ti_{PM}/[Sm_{PM} + Tb_{PM}]$. Sample locations: WZ01–WZ10, Wozhong; WS03, WS07, Wase; HS01–HS06 and HY01, Houshan.

Downloaded from https://academic.oup.com/petrology/article/51/8/1617/1456692 by U.S. Department of Justice user on 17 August 2022

ultrapotassic volcanic rocks have relatively higher MgO but lower TiO_2 than Cenozoic shoshonites from the Tibetan Plateau (Fig. 4f).

All the samples show enriched ($[La/Yb]_N = 7{\cdot}8–22{\cdot}9$) light rare earth element (LREE) and flat heavy REE (HREE) patterns (Fig. 5a). The large ion lithophile elements (LILE), particularly Rb, Ba and K, are significantly enriched relative to the high field strength elements (HFSE) and HREE (Fig. 5b). In the primitive mantle-normalized multi-element diagram, all the samples exhibit strong negative Ta–Nb–Ti anomalies (e.g. $[Nb/La]_N = 0{\cdot}20–0{\cdot}29$) and positive Sr and Pb anomalies (Fig. 5b).

Sr–Nd–Pb isotopes

All the samples have relatively high initial $^{87}Sr/^{86}Sr$ (0·7056–0·7101) and low initial $^{143}Nd/^{144}Nd$ (0·51237–0·51254), corresponding to $\varepsilon_{Nd}(t)$ values of −0·97 to −4·36 (Table 4), plotting within the enriched quadrant of the conventional Sr–Nd isotope diagram (Fig. 6a), as shown

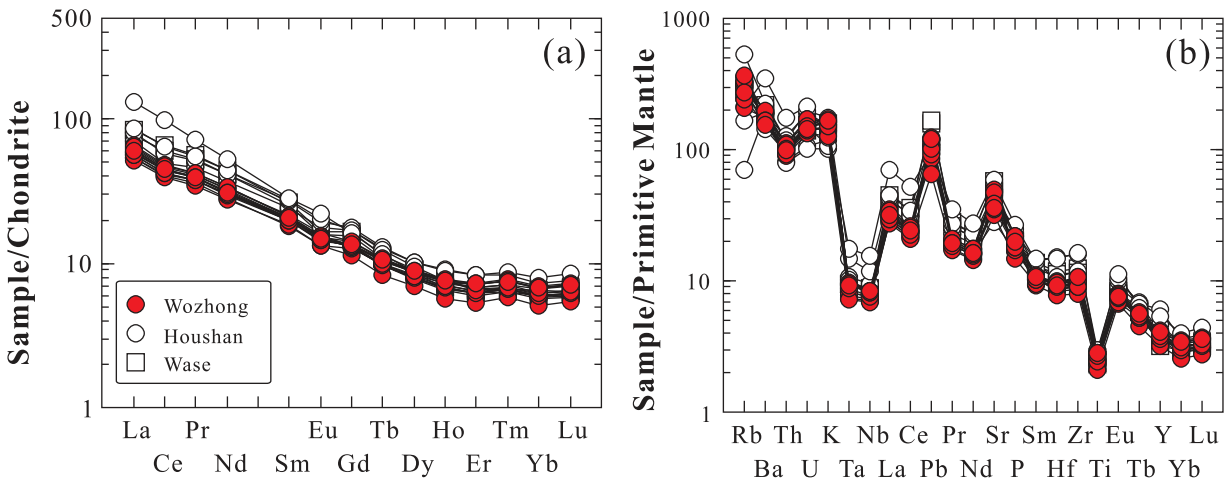

Fig. 5. Chondrite-normalized REE patterns (a) and primitive mantle (PM)-normalized multi-element patterns (b) of western Yunnan potassic and ultrapotassic rocks. Chondrite and PM normalization values are from Taylor & McLennan (1985) and Sun & McDonough (1989), respectively.

Table 4: Sr and Nd isotope data for the western Yunnan potassic and ultrapotassic rocks

Sample	$^{87}Rb/^{86}Sr$	$^{87}Sr/^{86}Sr$ (2σ)	$(^{87}Sr/^{86}Sr)_i$	$^{147}Sm/^{144}Nd$	$^{143}Nd/^{144}Nd$ (2σ)	$(^{143}Nd/^{144}Nd)_i$	T_{DM} (Ma)	$\varepsilon_{Nd}(t)$
WZ01	0·4010	0·706279 ± 10	0·706080	0·1273	0·512480 ± 7	0·512451	1183	−2·77
WZ03	0·5897	0·706297 ± 11	0·706004	0·1235	0·512481 ± 7	0·512453	1132	−2·73
WZ07	0·8197	0·706930 ± 13	0·706523	0·1306	0·512471 ± 7	0·512441	1247	−2·96
WZ08	0·6137	0·710449 ± 14	0·710144	0·1293	0·512461 ± 7	0·512432	1245	−3·15
HS01	0·2998	0·705722 ± 13	0·705573	0·1281	0·512533 ± 8	0·512503	1102	−1·75
HS02	0·1291	0·705761 ± 13	0·705697	0·1296	0·512573 ± 6	0·512543	1049	−0·97
HS06	0·8276	0·706807 ± 11	0·706396	0·1228	0·512397 ± 8	0·512369	1264	−4·36
HS-3	0·9329	0·706881 ± 14	0·706417	0·1247	0·512485 ± 7	0·512456	1141	−2·66
HS-3*	0·9329	0·706801 ± 17	0·706337	0·1247	0·512422 ± 10	0·512393	1249	−3·89
HS-5	0·6601	0·706842 ± 13	0·706514	0·1271	0·512492 ± 6	0·512463	1161	−2·54
HS-5*	0·6600	0·706740 ± 20	0·706412	0·1271	0·512421 ± 10	0·512392	1286	−3·92

$^{87}Rb/^{86}Sr$ and $^{147}Sm/^{144}Nd$ are calculated using whole-rock Rb, Sr, Sm and Nd contents in Table 3. $\varepsilon_{Nd}(t) = [(^{143}Nd/^{144}Nd)_s/(^{143}Nd/^{144}Nd)_{CHUR} - 1] \times 10000$. $T_{DM} = \ln[(^{143}Nd/^{144}Nd)_s - (^{143}Nd/^{144}Nd)_{DM}]/[(^{143}Sm/^{144}Nd)_s - (^{147}Sm/^{144}Nd)_{DM}]/\lambda$ (DePaolo, 1981). In the calculation, $(^{143}Nd/^{144}Nd)_{CHUR} = 0{\cdot}512638$, $(^{147}Sm/^{144}Nd)_{CHUR} = 0{\cdot}1967$, $(^{143}Nd/^{144}Nd)_{DM} = 0{\cdot}51315$, $(^{147}Sm/^{144}Nd)_{DM} = 0{\cdot}2136$ and $t = 35$ Ma. Sr–Nd isotope of HS-3* and HS-5* was obtained by acid leaching.

Downloaded from https://academic.oup.com/petrology/article/51/8/1617/1456692 by U.S. Department of Justice user on 17 August 2022

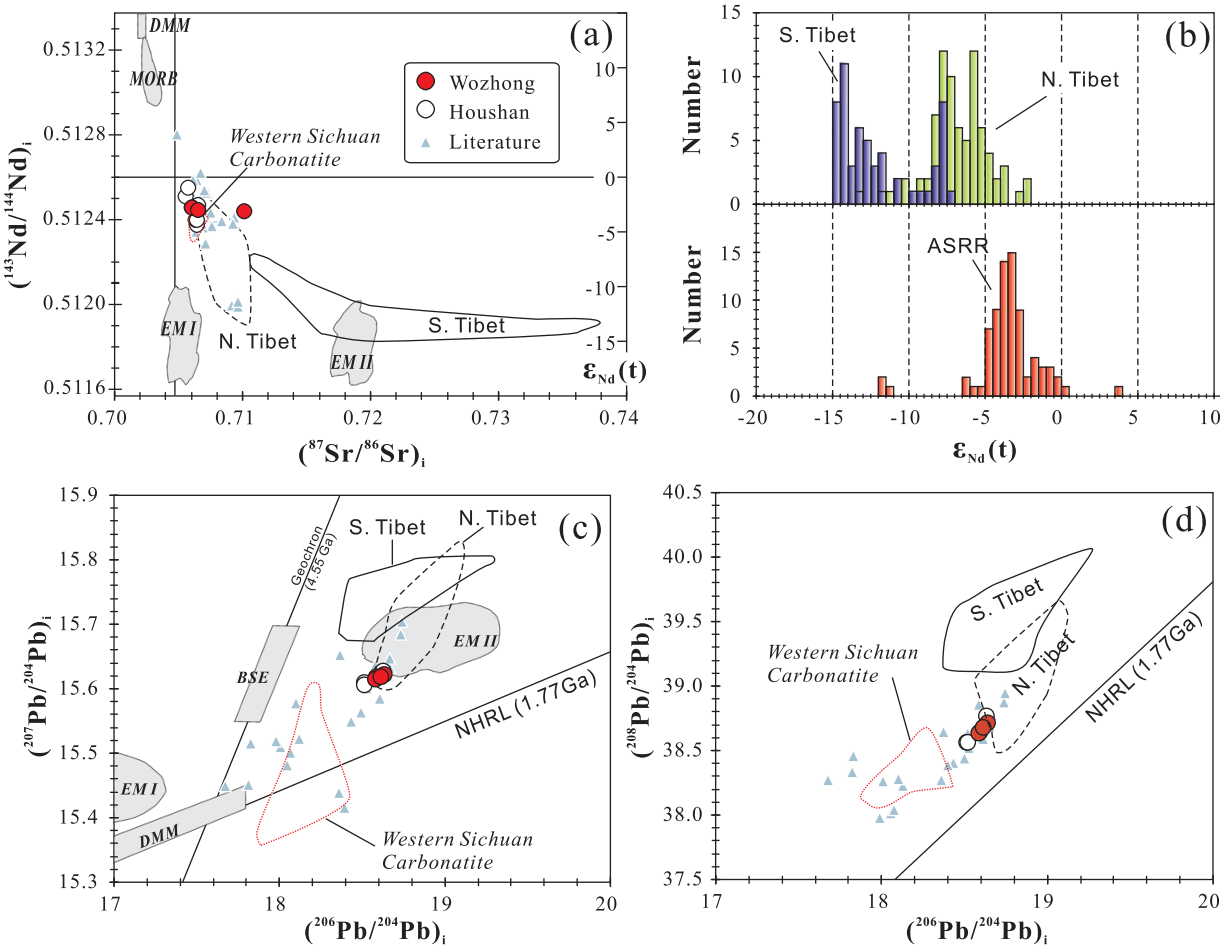

Fig. 6. $\varepsilon_{Nd}(t)$ vs $^{87}Sr/^{86}Sr_i$ (a), histogram of $\varepsilon_{Nd}(t)$ (b), $^{206}Pb/^{204}Pb$ vs $^{207}Pb/^{204}Pb$ and $^{208}Pb/^{204}Pb$ (c, d) for the western Yunnan and Tibetan Cenozoic K-rich rocks, showing that the western Yunnan Paleogene potassic and ultrapotassic rocks have restricted Sr–Nd–Pb isotopic compositions (Zhu *et al.*, 1992; Xu *et al.*, 2001*a*; Li *et al.*, 2002; Guo *et al.*, 2005) that differ from those of post-collisional potassic volcanic rocks from the Tibetan Plateau (South Tibet and North Tibet) (Arnaud *et al.*, 1992; Turner *et al.*, 1996; Miller *et al.*, 1999; Ding *et al.*, 2003; Guo *et al.*, 2006; Zhao *et al.*, 2009). The field of western Sichuan Cenozoic carbonatites is from Hou *et al.* (2006). Northern Hemisphere Reference Line (NHRL), mantle source 'reservoirs' BSE, PREMA, MORB, OIB, EM I and EM II are from Zindler & Hart (1986).

previously (Zhu *et al.*, 1992; Wang *et al.*, 2001; Xu *et al.*, 2001*a*; Li *et al.*, 2002; Guo *et al.*, 2005). The western Yunnan Paleogene potassic and ultrapotassic rocks have higher $\varepsilon_{Nd}(t)$ and lower initial $^{87}Sr/^{86}Sr$ (Fig. 6a and b) than the Cenozoic shoshonitic rocks from the Tibetan Plateau (Turner *et al.*, 1996; Miller *et al.*, 1999; Ding *et al.*, 2003; Guo *et al.*, 2006; Zhao *et al.*, 2009). The Nd-isotope model ages of the western Yunnan Paleogene potassic and ultrapotassic rocks (based on the depleted mantle) range from 1·05 to 1·29 Ga (Table 4).

The western Yunnan mafic potassic and ultrapotassic rocks have initial $^{206}Pb/^{204}Pb$ of 18·516–18·638 (Table 5). Both initial $^{207}Pb/^{204}Pb$ (15·607–15·627) and $^{208}Pb/^{204}Pb$ (38·564–38·766) are radiogenic and plot well above the Northern Hemisphere Reference Line (NHRL; Hart, 1984) in the conventional Pb isotope diagrams (Fig. 6c and d). The Pb isotopic compositions are restricted to within the range of Paleogene alkali-rich porphyries (Deng *et al.*, 1998*a*; Zeng *et al.*, 2002) and other potassic and ultrapotassic lavas (Zhu *et al.*, 1992; Wang *et al.*, 2001; Guo *et al.*, 2005) along, and in the vicinity of, the northern Ailao Shan–Red River fault (Fig. 6c and d). As a whole, the western Yunnan potassic and ultrapotassic rocks show distinctively lower initial $^{207}Pb/^{204}Pb$ and $^{208}Pb/^{204}Pb$ than the post-collisional shoshonitic volcanic rocks from Tibet (Fig. 6c and d) (Turner *et al.*, 1996; Miller *et al.*, 1999; Ding *et al.*, 2003).

Mineral compositions

Major element compositions of olivine and clinopyroxene phenocrysts in samples from the Wozhong mafic potassic and ultrapotassic rocks have been described previously (Xu *et al.*, 2003); we present new data here.

Downloaded from https://academic.oup.com/petrology/article/51/8/1617/1456692 by U.S. Department of Justice user on 17 August 2022

Table 5: Pb isotope data of the western Yunnan potassic and ultrapotassic rocks

Sample	$^{206}Pb/^{204}Pb$	$^{207}Pb/^{204}Pb$	$^{208}Pb/^{204}Pb$	μ	k	$(^{206}Pb/^{204}Pb)_i$	$(^{207}Pb/^{204}Pb)_i$	$(^{208}Pb/^{204}Pb)_i$	Δ7/4	Δ8/4
WZ01	18·6559 ± 09	15·6210 ± 9	38·7082 ± 22	12·10	34·07	18·590	15·618	38·649	11·18	54·68
WZ03	18·6334 ± 22	15·6180 ± 19	38·6844 ± 48	9·13	25·46	18·584	15·616	38·640	11·02	54·56
WZ07	18·6885 ± 07	15·6255 ± 07	38·7595 ± 24	9·33	26·10	18·638	15·623	38·714	11·18	55·43
WZ08	18·6705 ± 09	15·6212 ± 08	38·7259 ± 22	10·24	28·02	18·615	15·619	38·677	10·98	54·51
HS01	18·5560 ± 11	15·6111 ± 10	38·6085 ± 25	7·29	23·10	18·516	15·609	38·568	11·11	55·53
HS02	18·5562 ± 11	15·6086 ± 11	38·6031 ± 29	6·95	22·32	18·518	15·607	38·564	10·84	54·87
HS06	18·6947 ± 20	15·6303 ± 17	38·8173 ± 44	11·79	29·84	18·630	15·627	38·766	11·68	61·43

$\Delta 7/4 = [(^{207}Pb/^{204}Pb)_i - (^{207}Pb/^{204}Pb)_{NHRL}] \times 100$; $\Delta 8/4 = [(^{208}Pb/^{204}Pb)_i - (^{208}Pb/^{204}Pb)_{NHRL}] \times 100$; $(^{207}Pb/^{204}Pb)_{NHRL} = 0{\cdot}1084 \times (^{206}Pb/^{204}Pb)_i + 13{\cdot}491$; $(^{208}Pb/^{204}Pb)_{NHRL} = 1{\cdot}209 \times (^{206}Pb/^{204}Pb)_i + 15{\cdot}627$ (Hart, 1984). Initial Pb isotope ratios are calculated using whole-rock U, Th and Pb contents in Table 3, $t = 35$ Ma.

Olivine phenocrysts and spinel inclusions

The high-Mg samples contain abundant olivine phenocrysts with Fo contents in crystal cores varying over a wide range ($Fo_{94–75}$), which is somewhat correlated with their size and crystal shape (Table 6). In general, Fo contents decrease from large (>1 mm) crystals to medium (0·3–1 mm) and to small (<0·3 mm) crystals. The olivine phenocrysts contain varying amounts of the minor element oxides CaO, NiO and MnO (Fig. 7; Table 6), which correlate with their Fo contents (Fig. 7a–c). All the olivine phenocrysts contain higher CaO (>0·1 wt %; Table 6; Fig. 7a) than olivines in mantle xenoliths and orogenic peridotites (typically <0·1 wt % CaO; Simkin & Smith, 1978; Gurenko *et al.*, 1996), but are similar to olivines in boninites, picrites and lamproites (Krishnamurthy *et al.*, 2000; Larsen & Pedersen, 2000; Thompson & Gibson, 2000; Prelević & Foley, 2007). NiO decreases with decreasing Fo content, which differs from the mantle olivine array (Sato, 1977) (Fig. 7c). Large olivine phenocrysts are zoned (Fig. 7d), commonly with Fo and NiO decrease, but MnO and CaO increase from core via mantle to rim. Some olivines show reversed zoning with Fo increasing from cores to mantle, and then decreasing towards the rim (Fig. 7e). The reversely zoned olivine contains ~0·2 wt % CaO in its core, which is not like the mantle xenocrysts.

All spinels occur as inclusions in Wozhong and Houshan olivine phenocrysts and xenocrysts and have low Al_2O_3 (<10·5 wt %), high Cr-number (0·55–0·94) and variably low Mg-number (0·12–0·64) (Table 7; Fig. 8). The end-members are dominated by chromite (2·9–79·4%) and magnetite (7·9–89·2%), with minor spinel (1·2–20·5) and ulvöspinel (0·2–9·2%). The spinel inclusions and host olivines show compositional trends that depart from the mantle array (Arai, 1994). The spinel inclusions in small olivines are indistinguishable from those in large olivine crystals in terms of Cr-number (Fig. 8). There is a clear positive correlation between spinel Mg-number and the Fo content of the host olivine (Fig. 8b). The spinels all have variably high Fe^{3+}, with estimated fO_2 varying from 0·43 to 5·0 (with a mean of 2·00 ± 0·96) log units above the fayalite–magnetite–quartz (FMQ) buffer (Ballhaus *et al.*, 1990). Overall, the calculated $\Delta\log(fO_2)$ values from single spinels vary widely with decreasing host olivine Fo content, but they concentrate between 1·19 to 2·65 (with a mean of 1·81 ±0·66) for host olivines with Fo > 90% (Fig. 8c).

Clinopyroxene

Clinopyroxene (cpx) shows complex compositional zoning (normal, reverse and oscillatory) (Figs 9 and 10; Table 8). Cpx phenocrysts with normal zoning show a uniform composition with sharp Fe enrichment in the narrow rims (<50 μm) or a gradual core-to-rim Mg-number decrease (Fig. 9a). The cores of normally zoned cpx are all Ti–Al-poor diopside with an end-member composition of $Wo_{39–47}En_{45–53}Fs_{5–11}$, with low TiO_2, Al_2O_3, Na_2O and varying Cr_2O_3 contents, whereas the rims have high TiO_2, Al_2O_3 and low Cr_2O_3 (Fig. 9a).

Some cpx phenocrysts show reverse zoning with lower Mg-number in the core than in the mantle (Fig. 9b). The colourless mantles of reversely zoned cpx have compositions similar to those of normally zoned cpx phenocrysts. The cores of the reversely zoned crystals show a broad compositional range with relatively low Ti, Al, Na and Cr (Fig. 10). The cpx with green cores also shows reverse zoning with very low Mg-number cores (0·49–0·74) (Fig 9c and 10). The green cores have high FeO and Na_2O but low Cr_2O_3 and TiO_2 (Figs 9g and 10). There is a large compositional contrast between the green cores and the mantles (Fig. 9g). Na_2O and Al_2O_3 exhibit an abrupt decrease from nearly homogeneous Fe-rich cores to the Mg-rich mantles (Fig. 9g).

Some of the resorbed cpx phenocrysts show oscillatory zoning (Fig. 9d–f). Most of them record two or three episodes of correlated compositional variations such as the

Downloaded from https://academic.oup.com/petrology/article/51/8/1617/1456692 by U.S. Department of Justice user on 17 August 2022

Table 6: Representative electron probe analyses of olivine phenocrysts

Probe no.	SiO_2	TiO_2	Al_2O_3	Cr_2O_3	FeO	MnO	MgO	CaO	Na_2O	K_2O	NiO	Total	Fo%
Anhedral macrophyric Ol (>1 mm)													
WZ01-11C	40·95	b.d.l.	b.d.l.	0·09	8·11	0·16	50·02	0·17	b.d.l.	b.d.l.	0·37	99·89	91·7
WZ01-12R	40·38	0·04	b.d.l.	b.d.l.	10·28	0·16	47·93	0·22	b.d.l.	b.d.l.	0·34	99·39	89·3
WZ05-14C	41·49	0·03	0·04	0·05	6·78	0·08	51·54	0·16	b.d.l.	b.d.l.	0·50	100·69	93·2
WZ05-16R	38·36	b.d.l.	b.d.l.	b.d.l.	20·78	0·59	39·81	0·73	b.d.l.	b.d.l.	0·08	100·40	77·4
WZ09-16C	41·06	b.d.l.	b.d.l.	b.d.l.	7·39	0·04	50·83	0·22	b.d.l.	b.d.l.	0·40	99·97	92·5
WZ09-18R	38·74	b.d.l.	b.d.l.	b.d.l.	19·03	0·47	41·42	0·59	b.d.l.	b.d.l.	0·10	100·38	79·5
Euhedral macrophyric Ol (>1 mm)													
WZ01-09C	40·86	b.d.l.	b.d.l.	0·05	6·77	0·11	51·33	0·18	b.d.l.	b.d.l.	0·42	99·73	93·1
WZ01-10R	39·59	b.d.l.	0·03	0·03	11·17	0·26	46·87	0·32	b.d.l.	b.d.l.	0·29	98·58	88·2
WZ03-10C	41·00	b.d.l.	0·03	0·06	7·31	0·11	51·00	0·18	b.d.l.	b.d.l.	0·38	100·08	92·6
WZ03-11R	39·81	b.d.l.	b.d.l.	0·00	13·17	0·40	46·78	0·36	b.d.l.	b.d.l.	0·22	100·75	86·4
WZ04-04C	40·77	b.d.l.	b.d.l.	0·05	8·10	0·12	50·01	0·18	0·03	b.d.l.	0·42	99·69	91·7
WZ04-05R	39·18	b.d.l.	b.d.l.	b.d.l.	14·54	0·44	45·40	0·41	b.d.l.	b.d.l.	0·15	100·15	84·8
WZ07-46C	41·44	b.d.l.	0·03	b.d.l.	7·40	0·06	50·69	0·17	b.d.l.	b.d.l.	0·41	100·23	92·4
WZ07-47R	39·41	b.d.l.	b.d.l.	b.d.l.	14·14	0·26	45·75	0·28	0·03	b.d.l.	0·29	100·22	85·2
WZ10-20C	40·97	b.d.l.	b.d.l.	0·09	8·22	0·04	50·76	0·34	b.d.l.	b.d.l.	0·30	100·76	91·7
WZ10-21R	38·65	b.d.l.	b.d.l.	b.d.l.	20·14	0·51	40·96	0·53	b.d.l.	0·04	0·10	100·98	78·4
Euhedral medium-sized phenocrysts (0·3–1 mm)													
WZ01-15C	40·41	b.d.l.	b.d.l.	b.d.l.	9·02	0·12	49·62	0·21	b.d.l.	b.d.l.	0·43	99·87	90·8
WZ01-16R	39·85	b.d.l.	b.d.l.	b.d.l.	13·08	0·28	45·51	0·43	b.d.l.	b.d.l.	0·22	99·42	86·1
WZ05-17C	40·79	b.d.l.	0·04	0·13	7·23	0·08	51·06	0·23	0·03	b.d.l.	0·40	100·00	92·6
WZ05-18R	38·08	b.d.l.	b.d.l.	0·04	21·43	0·58	39·62	0·46	0·03	b.d.l.	0·07	100·31	76·7
WZ06-06C	40·56	b.d.l.	b.d.l.	0·07	9·76	0·09	49·22	0·30	0·03	b.d.l.	0·41	100·48	90·0
WZ06-07R	39·68	0·03	b.d.l.	0·03	12·28	0·27	47·29	0·38	0·04	b.d.l.	0·27	100·27	87·3
WZ07-51C	41·00	b.d.l.	0·03	0·05	6·62	0·11	51·30	0·14	b.d.l.	b.d.l.	0·34	99·63	93·2
WZ07-54R	39·39	b.d.l.	b.d.l.	b.d.l.	16·19	0·42	43·68	0·25	b.d.l.	b.d.l.	0·15	100·12	82·8
WZ08-45C	40·94	b.d.l.	0·04	b.d.l.	7·99	0·10	49·88	0·20	b.d.l.	b.d.l.	0·36	99·52	91·8
WZ08-47R	40·01	b.d.l.	0·03	b.d.l.	12·82	0·28	47·06	0·26	b.d.l.	b.d.l.	0·31	100·78	86·8
Euhedral small phenocrysts (<0·3 mm)													
WZ01-14C	40·27	b.d.l.	b.d.l.	0·04	12·19	0·29	47·13	0·22	b.d.l.	b.d.l.	0·31	100·46	87·3
WZ02-10C	40·38	b.d.l.	b.d.l.	b.d.l.	10·31	0·18	48·27	0·15	b.d.l.	b.d.l.	0·36	99·68	89·3
WZ03-18C	39·64	b.d.l.	0·03	b.d.l.	14·45	0·49	44·65	0·36	b.d.l.	b.d.l.	0·13	99·80	84·6
WZ05-28C	38·62	b.d.l.	b.d.l.	0·13	20·86	0·55	39·71	0·41	b.d.l.	b.d.l.	0·14	100·43	77·2
WZ06-20C	40·18	b.d.l.	b.d.l.	b.d.l.	13·12	0·32	45·30	0·45	b.d.l.	b.d.l.	0·20	99·59	86·0
WZ07-38C	40·40	b.d.l.	b.d.l.	b.d.l.	10·64	0·16	47·71	0·13	b.d.l.	b.d.l.	0·28	99·33	88·9
WZ08-64C	39·81	b.d.l.	b.d.l.	b.d.l.	13·25	0·26	46·25	0·28	0·05	b.d.l.	0·21	100·14	86·2
WZ09-22C	38·37	0·03	b.d.l.	0·05	21·16	0·44	39·22	0·53	b.d.l.	0·03	0·07	99·91	76·8
WZ10-10C	39·35	b.d.l.	b.d.l.	b.d.l.	17·58	0·42	42·35	0·35	b.d.l.	b.d.l.	0·17	100·29	81·1

C and R after probe numbers indicate core and rim of Ol phenocrysts, respectively; b.d.l., below detection limit.

core-to-rim Mg-number, Al_2O_3 and Na_2O systematics (Fig. 9h). Despite the complex zoning in these resorbed cpx phenocrysts, Cr, Al, Na and Ti all plot in compositional ranges defined by cpx with simple zoning (Fig. 10).

Cpx phenocrysts in Jianchuan trachyte (Fig. 1a) all show normal zoning with varying compositions, and they have relatively lower Mg-number and Cr and higher Al, Ti and Na than those in the mafic samples (Fig. 10).

Downloaded from https://academic.oup.com/petrology/article/51/8/1617/1456692 by U.S. Department of Justice user on 17 August 2022

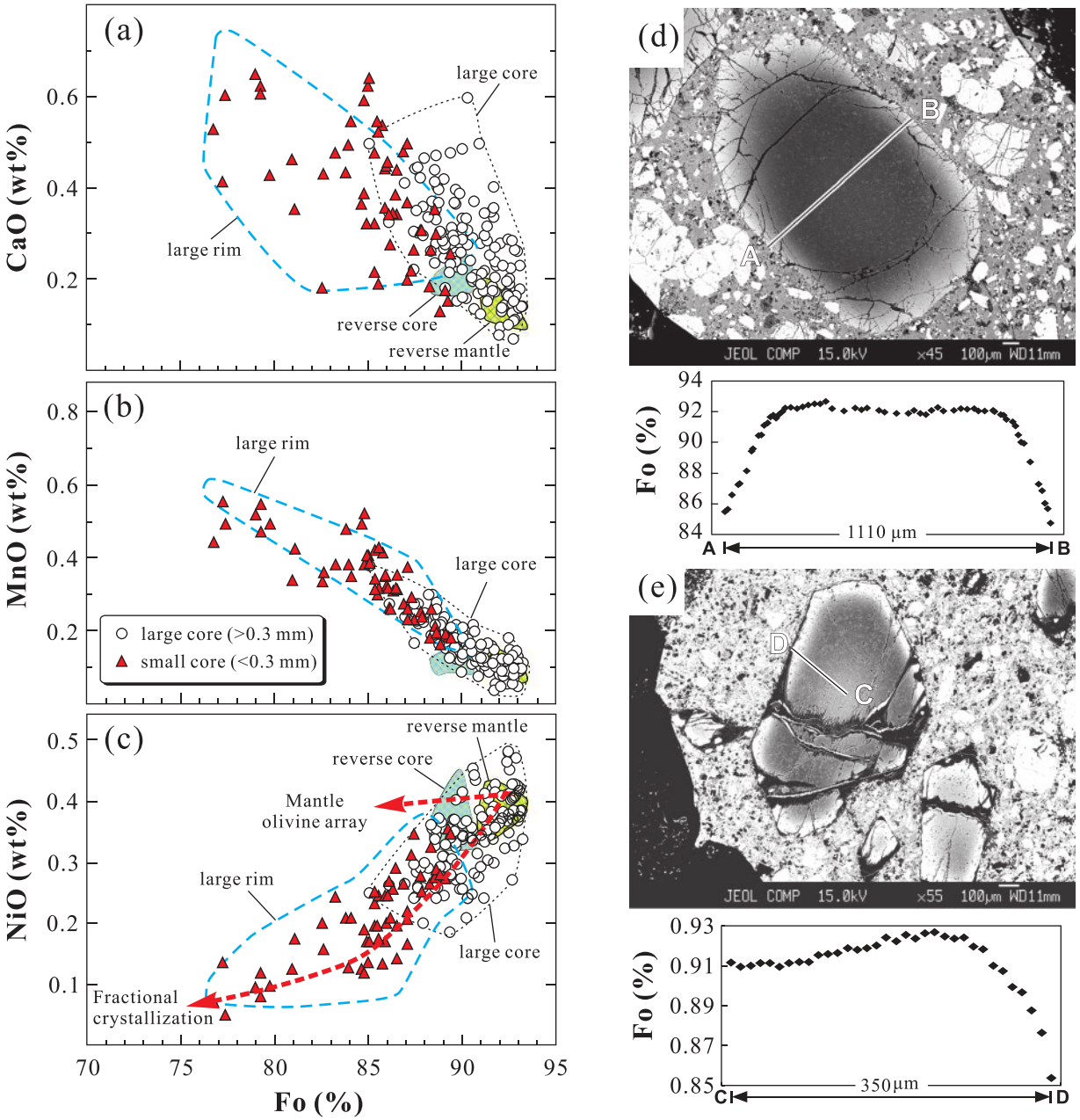

Fig. 7. (a–c) Chemical variations of olivine phenocrysts. Mantle olivine array and fractional crystallization trend in (c) are from Sato (1977). (d, e) back-scattered electron images of olivine phenocrysts, and compositional traverses, showing normal (line A–B) and reverse zoning (line C–D).

In situ trace element analyses have been obtained for cpx crystals with complex zoning and with green cores (Table 9). The mantles of both reversely zoned cpx and cpx with green cores have similar trace element concentrations to the normally zoned cpx (Fig. 10). The green cores have distinctively low REE and Y (Table 8; Fig. 10) and nearly constant Nb/La (0·036–0·054), whereas the mantles of the cpx with green cores and other cpx crystals have variable Nb/La (Fig. 10h). The chondrite-normalized REE patterns are parallel and convex-upward for all cpx crystals, except for the green cores, which have patterns convex-upward from La to Dy and convex-downward from Dy to Lu (Fig. 11). Trace element patterns of both reversely and normally zoned cpx crystals are similar to those of diopsidic cpx from potassic igneous rocks (Francalanci *et al*, 2005; Fedele *et al.*, 2009), but different

Downloaded from https://academic.oup.com/petrology/article/51/8/1617/1456692 by U.S. Department of Justice user on 17 August 2022

Table 7: Representative electron probe analyses of spinel inclusions in olivines

Sample:	WZ01	WZ02	WZ02	WZ03	WZ04	WZ05	WZ05	WZ06	WZ07	WZ09	WZ09
Probe no.:	01_11	02_1	02_27	03_31	04_11	05_19	05_25	06_15	07_5	09_1	09_5
Host (Fo):	90·6	89·7	92·6	93·0	92·9	91·2	83·2	91·7	91·8	91·4	83·1
Cr_2O_3	57·3	54·8	57·9	54·5	57·6	56·2	34·7	54·0	56·0	57·0	40·1
Al_2O_3	5·81	5·10	5·65	5·69	5·91	8·36	6·95	5·29	7·61	7·27	7·58
TiO_2	0·20	0·22	0·21	0·62	0·26	0·25	1·87	0·29	0·30	0·62	2·13
FeO	24·0	28·4	20·7	24·8	22·4	21·9	46·0	27·4	22·6	22·8	41·9
MgO	10·4	8·68	12·7	11·3	12·2	10·7	5·02	9·30	10·7	10·7	6·13
MnO	0·49	0·55	0·38	0·41	0·41	0·41	0·59	0·55	0·41	0·49	0·60
NiO	0·36	0·12	0·38	0·53	0·34	0·12	0·14	0·21	0·11	0·07	0·10
Total	98·56	97·87	97·92	97·85	99·12	97·94	95·27	97·04	97·73	98·95	98·54
Cations based on 4 oxygens per formula unit											
Cr^{3+}	1·534	1·498	1·537	1·458	1·515	1·494	0·985	1·481	1·497	1·508	1·092
Al^{3+}	0·232	0·208	0·224	0·227	0·232	0·332	0·294	0·216	0·303	0·287	0·308
Ti^{4+}	0·005	0·006	0·005	0·016	0·006	0·006	0·050	0·007	0·008	0·016	0·055
Fe^{3+}	0·224	0·282	0·229	0·284	0·240	0·161	0·620	0·289	0·184	0·173	0·489
Fe^{2+}	0·456	0·539	0·350	0·418	0·382	0·455	0·760	0·505	0·454	0·464	0·720
Mg^{2+}	0·525	0·448	0·634	0·572	0·604	0·536	0·269	0·481	0·538	0·536	0·315
Mn^{2+}	0·014	0·016	0·011	0·012	0·012	0·012	0·018	0·016	0·012	0·014	0·017
Ni^{2+}	0·010	0·003	0·010	0·014	0·009	0·003	0·004	0·006	0·003	0·002	0·003
Mg-no.	0·535	0·454	0·644	0·578	0·613	0·541	0·261	0·488	0·542	0·536	0·305
Cr-no.	0·869	0·878	0·873	0·865	0·867	0·818	0·770	0·873	0·832	0·840	0·780
End-members											
Spinel	11·6	10·4	11·2	11·4	11·6	16·6	15·1	10·8	15·2	14·5	15·8
Magnetite	11·2	14·2	11·5	14·3	12·1	8·1	31·8	14·5	9·2	8·7	25·2
Ulvöspinel	0·2	0·3	0·3	0·8	0·3	0·3	2·6	0·4	0·4	0·8	2·8
Chromite	76·9	75·1	77·0	73·5	76·0	75·0	50·5	74·3	75·2	76·0	56·2
$\Delta\log(fO_2)$	1·61	1·95	1·94	2·62	2·20	1·22	2·63	2·41	1·57	1·37	2·16

Fe^{2+} and Fe^{3+} are recalculated with the charge balance method of Droop (1987); $\Delta\log(fO_2)$ values are calculated relative to the FMQ buffer (Ballhaus *et al.*, 1990) at conditions of $T = 1100°C$ and $P = 10$ kbar.

from those of kimberlites or kamafugites (Melluso *et al.*, 2008), whereas the green cores have different REE patterns from the cpx of these potassic or ultrapotassic rocks (Francalanci *et al.*, 2005; Melluso *et al.*, 2008; Fedele *et al.*, 2009). The calculated REE patterns of the parental melts in equilibrium with the green cores (assumed to be of magmatic origin) are distinct from those of the host-rocks with a convex-downward shape from Gd to Lu, whereas those in equilibrium with cpx of reverse, oscillatory and normal zoning are very similar to the host-rocks except for the elevated REE contents (Fig. 11).

The cores of cpx with reverse, oscillatory and normal zoning, the mantles of cpx with reverse zoning and the green cores all have similar primitive mantle normalized trace element patterns with strong negative Nb, Ta, Zr, Hf, Ti and Ba anomalies. Most of the green cores show a positive Sr anomaly, and one green core shows positive Zr, Hf and Ti anomalies relative to adjacent REE (Fig. 11).

Phlogopite

Phlogopite phenocrysts and inclusions in cpx phenocrysts are compositionally similar, and are all characterized by high MgO (20·7–22·9 wt %) and Al_2O_3 (13·8–15·9 wt %), low TiO_2 (1·02–2·26 wt %) and FeO (5·32–7·96 wt %), with a small range in Mg-number (0·83–0·87) (Table 10). The high Al_2O_3 and low TiO_2 characteristics are similar to phlogopite in typical kimberlite, but differ from lamproitic micas (Fig. 12). It is probable that the phlogopite crystals are xenocrysts. A xenocrystal origin is also consistent with the petrography in that the phlogopite occurs as anhedral crystals with fine-grained magnetite aggregates at their rims or on the surfaces, and is probably oxidized (Fig 2b, c and e) during magma transport.

Downloaded from https://academic.oup.com/petrology/article/51/8/1617/1456692 by U.S. Department of Justice user on 17 August 2022

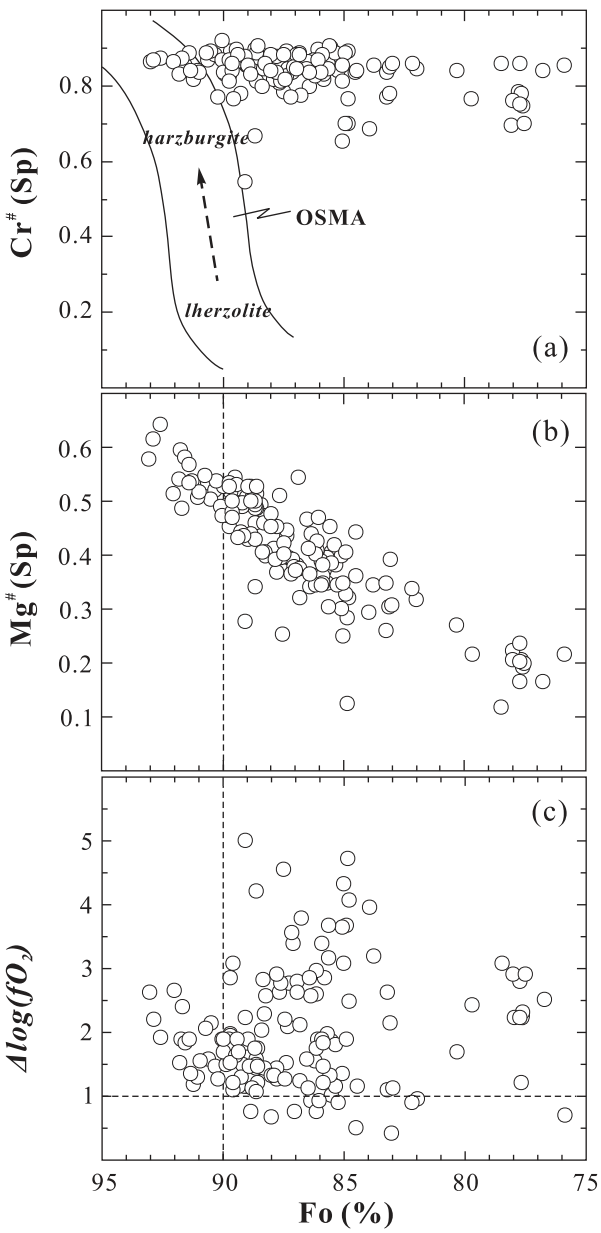

Fig. 8. Plots of Cr-number, Mg-number, $\Delta\log(fO_2)$ for spinel inclusions as a function of Fo mol % of the host olivine phenocrysts; Olivine–Spinel Mantle Array (OSMA) from Arai (1994); $\Delta\log(fO_2)$ values are relative to the FMQ buffer calculated using Ballhaus *et al.* (1990) at conditions of $T = 1100°C$ and $P = 10$ kbar.

Feldspar

The microlitic feldspars in the groundmass of the mafic potassic and ultrapotassics rocks show a broad compositional range ($An_{2-10}Ab_{24-44}Or_{50-74}$; broadly sanidine).

Oxides

The oxides in the groundmass are mostly titanomagnetite containing varying amounts of TiO_2 (2·17–10·64 wt %), Al_2O_3 (0·21–3·18 wt %) and Cr_2O_3 (0·02–2·0 wt %).

DISCUSSION

Magmatic evolution

Fractional crystallization and accumulation

The western Yunnan potassic and ultrapotassic rocks exhibit a large range of major element compositional variation, yet all have similar Sr–Nd–Pb isotopic and trace element characteristics (Figs 5 and 6), suggesting that the parental magmas may have formed in the same tectonic setting with similar magma sources, but experienced varying degrees of fractional crystallization and crystal accumulation.

The relatively narrow range of Fe_2O_3 (5·30–8·42 wt %) yet highly variable MgO (6·43–21·82 wt %) (Table 3) in rocks with strong positive MgO–Ni–Cr correlations (Fig. 13a and b) suggests the effect of fractional crystallization or accumulation of olivine in the bulk-rock samples (Feldstein & Lange, 1999). This is consistent with the correlated Fo–NiO–MnO–CaO variations in olivine phenocryst core compositions (Fig. 7). However, the high-Mg large olivine phenocrysts are not in equilibrium with 'melts' corresponding to the whole-rock compositions of the host lavas (Xu *et al.*, 2003). We suggest that there are at least two stages of olivine crystallization involved in the petrogenesis of the western Yunnan mafic potassic and ultrapotassic rocks. The cores of the large olivine phenocrysts (>0·3 mm) may have crystallized from early highly magnesian melts. In contrast, the rims of the large phenocrysts are compositionally similar to the fine-grained olivines (Fig. 7) and are probably in equilibrium with the host melt prior to or during eruption. It is also possible that some small olivines are of earlier origin, but have been re-equilibrated with the host melt in response to the later or latest event. The fast diffusion and re-equilibration of olivine with the host melt makes olivine less effective than cpx in recording magmatic histories. Additionally, CaO is negatively correlated with MgO for the mafic potassic and ultrapotassic rocks with MgO > ~10 wt %, which is consistent with the dilution effect of olivine accumulation (Fig. 13c). Together with the published data from the literature (Zhu *et al.*, 1992; Wang *et al.*, 2001; Xu *et al.*, 2001*a*; Li *et al.*, 2002; Guo *et al.*, 2005), a positive correlation between CaO and MgO is well defined for samples with <10 wt % MgO, pointing to the clinopyroxene-dominated fractionation (Fig. 13c), whereas some samples with >10 wt % MgO are mostly consistent with clinopyroxene accumulation (Fig. 13c). Figure 13c also suggests that the primitive (not primary) melts parental to the mafic potassic and ultrapotassic rocks may have ~10 wt % MgO.

Magma mixing

Magmatic evolution in post-collisional ultrapotassic rock series often involves crustal contamination and magma mixing (Varekamp & Kalamarides, 1989; Turbeville, 1993; Conticelli *et al.*, 1997). The compositional variation of the

Downloaded from https://academic.oup.com/petrology/article/51/8/1617/1456692 by U.S. Department of Justice user on 17 August 2022

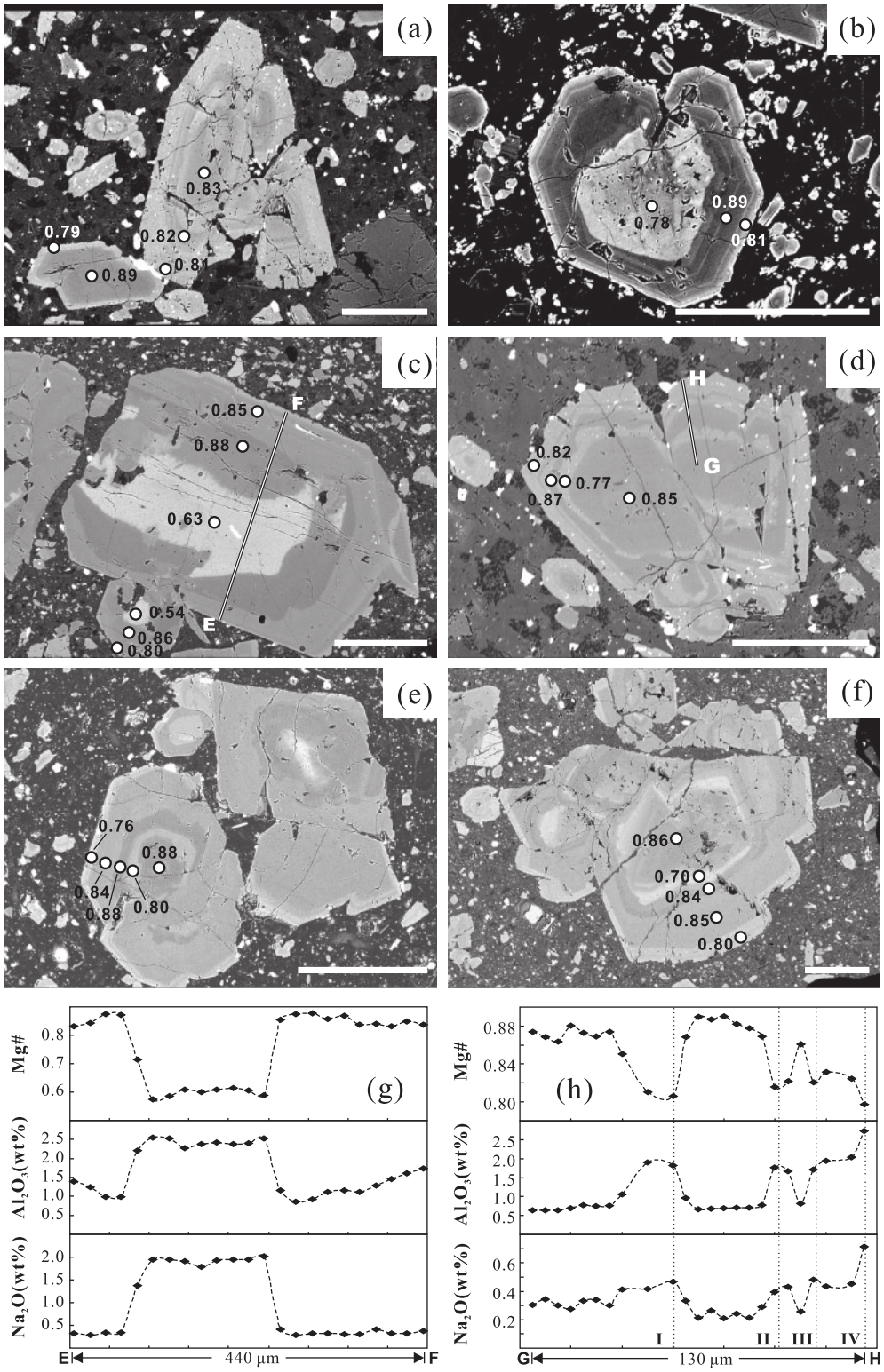

Fig. 9. Back-scattered electron images of normal zoning (a), reverse zoning (b), green-core (c), oscillatory zoning of cpx phenocrysts (d–f) and compositional sections of cpx green cores (g, from c) and oscillatory-zoned cpx phenocrysts (h, from d). Analysis spots and Mg-number values are also indicated; lines E–F and G–H are compositional traverses for (g) and (h). The scale bar represents 200 μm.

Downloaded from https://academic.oup.com/petrology/article/51/8/1617/1456692 by U.S. Department of Justice user on 17 August 2022

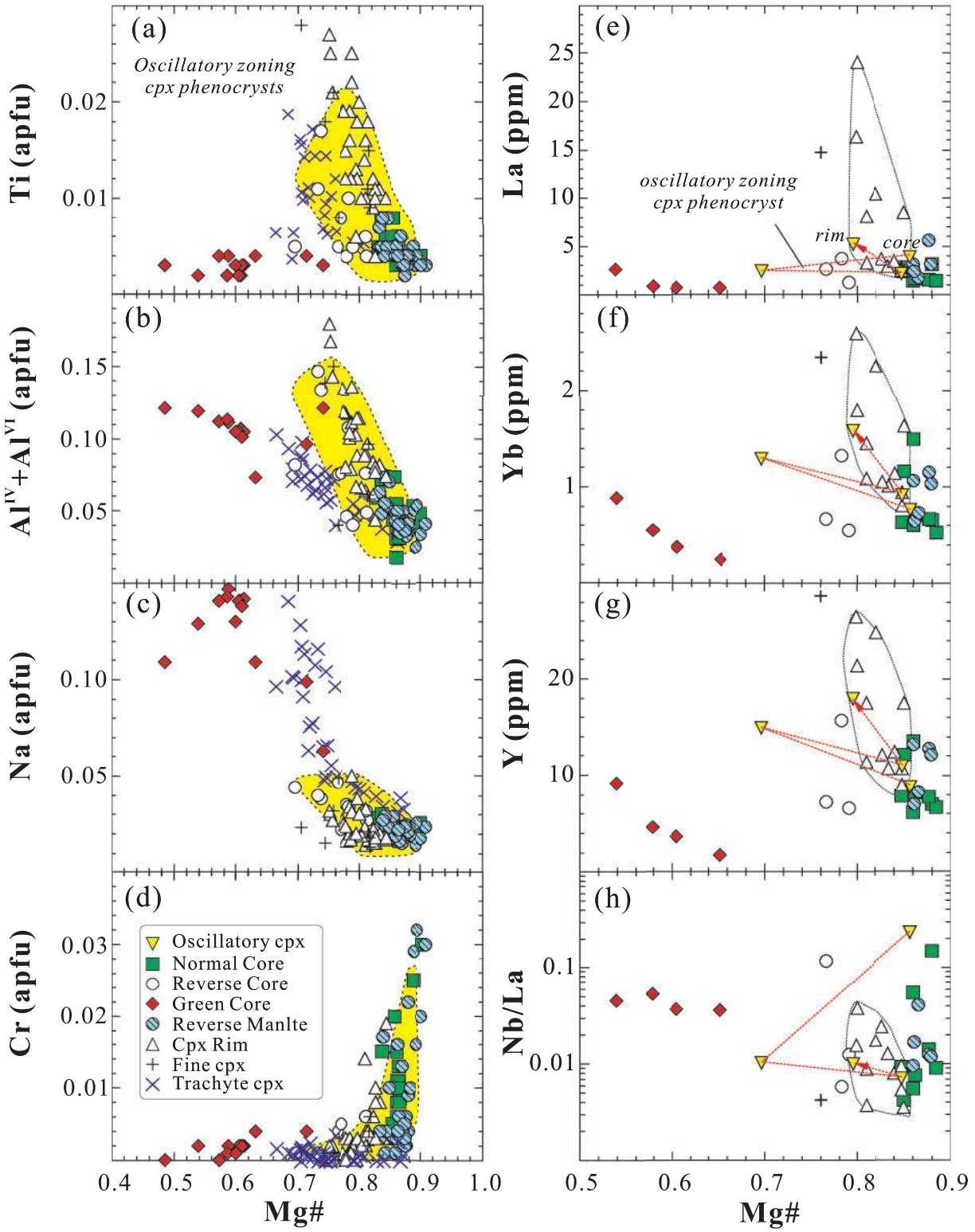

Fig. 10. Chemical variations of Cpx phenocrysts. Vectors indicate core-to-rim variation of oscillatory zoning. apfu, atoms per formula unit.

Downloaded from https://academic.oup.com/petrology/article/51/8/1617/1456692 by U.S. Department of Justice user on 17 August 2022

Table 8: Representative electron probe analyses of clinopyroxene with normal and reverse zoning and green cores

Cpx:	Normal zoning phenocryst				Reverse zoning phenocryst									Green-core xenocryst					Fine	Trachyte
Probe no.:	WZ05-4		WZ07-2		WZ02-1			WZ10-9			WZ07-3			WZ07-7			WZ07-9		WZ05-F1	JC03-11
Location:	core	rim	core	rim	core	mantle	rim	core	mantle	rim	core	mantle	rim	core	mantle	rim	core	mantle		
SiO_2	52·8	50·4	53·4	50·0	51·8	53·9	50·8	52·2	53·2	51·0	51·9	53·3	51·6	50·9	53·7	51·4	51·5	53·9	49·2	52·1
TiO_2	0·13	0·77	0·15	0·96	0·38	0·10	0·67	0·18	0·24	0·57	0·29	0·15	0·44	0·12	0·11	0·42	0·08	0·16	0·99	0·23
Al_2O_3	1·13	3·28	1·27	4·13	2·50	0·81	2·64	0·90	0·95	2·43	1·75	0·99	1·81	2·72	0·85	1·80	2·71	0·96	3·92	1·61
Cr_2O_3	1·02	0·08	0·88	0·08	0·01	0·30	0·10	0·03	0·44	0·05	0·16	0·03	0·03	0·02	0·16	b.d.l.	0·05	0·15	0·06	0·03
FeO	3·61	8·20	4·09	8·15	7·10	4·51	6·82	7·42	4·55	7·57	8·07	5·15	7·44	15·00	4·80	7·74	14·09	5·08	8·58	9·86
MnO	0·13	0·22	0·11	0·21	0·14	0·17	0·17	0·22	0·14	0·17	0·26	0·17	0·26	0·44	0·17	0·20	0·34	0·14	0·23	0·25
MgO	18·1	14·2	17·8	13·8	14·4	18·0	15·1	15·8	16·8	15·5	15·3	17·3	15·4	8·47	18·0	15·2	9·25	17·9	14·3	12·4
CaO	21·8	22·6	22·8	22·4	22·6	22·0	22·9	20·6	23·5	22·6	22·0	21·9	22·7	20·4	22·4	21·3	20·7	21·8	22·3	21·9
Na_2O	0·36	0·38	0·33	0·44	0·48	0·30	0·53	0·25	0·22	0·28	0·31	0·27	0·23	1·48	0·33	0·32	1·77	0·32	0·37	1·39
K_2O	b.d.l.	0·13	b.d.l.	0·22	b.d.l.	b.d.l.	0·04	b.d.l.	b.d.l.	0·08	b.d.l.	b.d.l.	b.d.l.	b.d.l.	b.d.l.	0·03	0·03	b.d.l.	0·08	b.d.l.
NiO	b.d.l.	b.d.l.	b.d.l.	b.d.l.	b.d.l.	0·03	b.d.l.	b.d.l.	b.d.l.	b.d.l.	b.d.l.	b.d.l.	b.d.l.	b.d.l.	b.d.l.	b.d.l.	b.d.l.	b.d.l.	b.d.l.	b.d.l.
Total	99·08	100·26	100·83	100·39	99·41	100·12	99·77	97·60	100·04	100·25	10·04	99·26	99·91	99·55	100·52	98·41	100·52	100·41	100·03	99·77
Cations based on 6 oxygens per formula unit																				
Si	1·934	1·863	1·928	1·846	1·925	1·958	1·873	1·972	1·944	1·875	1·918	1·957	1·907	1·949	1·940	1·929	1·939	1·953	1·823	1·938
Al^{IV}	0·049	0·137	0·054	0·154	0·075	0·035	0·115	0·028	0·041	0·105	0·076	0·043	0·079	0·051	0·036	0·071	0·061	0·041	0·171	0·062
Al^{VI}	0·000	0·006	0·000	0·025	0·034	0·000	0·000	0·012	0·000	0·000	0·000	0·000	0·000	0·072	0·000	0·009	0·058	0·000	0·000	0·016
Ti	0·004	0·021	0·004	0·027	0·011	0·003	0·018	0·005	0·006	0·016	0·008	0·004	0·012	0·003	0·003	0·012	0·002	0·004	0·028	0·010
Cr	0·030	0·002	0·025	0·002	0·000	0·009	0·003	0·001	0·013	0·001	0·005	0·001	0·001	0·000	0·004	0·002	0·004	0·002	0·003	
Fe^{3+}	0·073	0·119	0·080	0·115	0·055	0·057	0·140	0·023	0·061	0·136	0·088	0·053	0·098	0·082	0·097	0·063	0·127	0·063	0·156	0·099
Fe^{2+}	0·038	0·135	0·044	0·137	0·166	0·080	0·070	0·212	0·078	0·097	0·160	0·105	0·132	0·398	0·049	0·179	0·316	0·091	0·110	0·196
Mn	0·004	0·007	0·003	0·007	0·004	0·005	0·005	0·007	0·004	0·005	0·008	0·005	0·008	0·014	0·005	0·006	0·011	0·004	0·007	0·011
Mg	0·987	0·783	0·957	0·760	0·795	0·975	0·831	0·888	0·918	0·849	0·842	0·949	0·848	0·484	0·973	0·848	0·519	0·969	0·790	0·755
Ca	0·856	0·893	0·881	0·885	0·900	0·856	0·905	0·833	0·919	0·892	0·870	0·862	0·898	0·837	0·868	0·857	0·833	0·848	0·884	0·834
Na	0·026	0·027	0·023	0·032	0·035	0·021	0·038	0·018	0·015	0·020	0·022	0·019	0·017	0·110	0·023	0·024	0·129	0·022	0·027	0·076
K		0·006		0·011			0·002			0·004						0·001	0·002		0·004	
Ni						0·001														
Mg-no.	0·899	0·756	0·886	0·751	0·783	0·877	0·798	0·791	0·868	0·785	0·771	0·857	0·787	0·502	0·870	0·778	0·539	0·863	0·748	0·719
Fe^{3+}/Fe^{2+}	1·92	0·88	1·82	0·84	0·33	0·71	2·00	0·11	0·78	1·40	0·55	0·50	0·74	0·21	1·98	0·35	0·40	0·69	1·42	0·51
Wo	43·7	46·2	44·8	46·5	46·9	43·4	46·4	42·4	46·4	45·1	44·1	43·6	45·3	43·1	43·6	43·8	46·1	42·9	45·4	44·3
En	50·4	40·4	48·7	39·9	41·4	49·4	42·6	45·2	46·4	42·9	42·8	48·1	42·7	26·6	48·9	43·4	28·7	49·1	40·6	40·1
Fs	5·9	13·4	6·5	13·6	11·7	7·2	11·0	12·4	7·2	12·0	13·1	8·3	12·0	27·3	7·5	12·8	25·2	8·0	14·0	15·6

Fe^{2+} and Fe^{3+} are recalculated with the charge balance method of Droop (1987); b.d.l., below detection limit.

Downloaded from https://academic.oup.com/petrology/article/51/8/1617/1456692 by U.S. Department of Justice user on 17 August 2022

Table 9: Representative LA-ICP-MS analyzed trace elements (ppm) of clinopyroxenes

Cpx:	Green-core xenocryst						Normal zoning phenocryst					Oscillatory zoning phenocryst				Reverse zoning phenocryst			Fine
No.:	WZ07-1	WZ07-2	WZ07-3	WZ05-1	WZ05-2	WZ05-3	WZ07-14	WZ02-4	WZ05-5	WZ05-6	WZ10-8	WZ07-5	WZ07-6	WZ07-7	WZ07-8	WZ02-1	WZ02-2	WZ02-3	WZ07-9
Position:	core	mantle	core	core	mantle	rim	core	core	core	rim	core	core1	core2	mantle	rim	core	mantle	rim	
Mg-no.	0·605	0·860	0·580	0·652	0·879	0·820	0·860	0·847	0·880	0·756	0·877	0·857	0·697	0·847	0·795	0·783	0·877	0·798	0·760
Sc	74·8	70·9	106	67·8	64·1	88·4	55·1	45·2	46·2	61·7	55·5	47·9	77·3	60·2	87·5	57·1	61·7	72·7	92·4
Ti	532	1198	1179	694	1029	2234	1376	1126	957	1093	849	953	1004	967	1760	1002	1281	2651	2125
V	294	94·7	328	437	97·6	137	219	72·0	178	154	58·6	104	170	85·7	98·0	129	69·8	95·3	124
Cr	634	1208	259	186	1113	297	1044	3746	3287	2338	2852	1852	153	1340	1303	475	3025	2516	456
Co	24·5	34·9	27·5	40·1	35·3	33·2	43·9	33·4	43·4	40·6	30·2	35·9	39·3	34·3	33·2	28·0	30·1	29·6	32·1
Ni	50·0	135	36·5	58·1	135	88·0	169	180	155	152	163	153	74·7	156	105	91·9	167	138	82·8
Rb	0·234	0·259	0·582	21·1	1·70	31·9	5·10	0·302	29·7	<0·138	0·093	17·7	0·966	0·046	0·804	10·3	2·93	7·05	0·725
Ba	1·06	0·592	2·16	0·979	0·475	3·57	20·0	0·485	44·5	0·115	0·213	5·92	1·11	0·063	3·48	0·187	0·783	15·7	4·18
Sr	176	147	162	64·3	140	194	96·3	202	121	138	135	118	113	133	168	207	260	386	244
Y	3·70	13·2	4·67	1·72	12·2	24·8	13·6	7·87	7·03	9·09	7·74	8·80	14·9	11·0	18·0	15·7	12·8	26·5	28·6
Zr	12·1	10·3	21·2	90·6	9·63	35·5	13·7	7·77	8·89	6·81	3·83	26·5	14·1	6·10	22·7	14·2	14·4	49·6	30·6
Hf	0·551	0·504	1·11	2·45	0·466	1·54	0·494	0·282	0·271	0·221	0·245	0·736	0·700	0·277	1·09	0·671	0·711	2·09	1·50
Nb	0·025	0·030	0·047	0·023	0·037	0·185	0·139	<0·026	0·458	0·013	0·021	0·906	0·024	0·016	0·052	0·022	0·070	0·259	0·063
Ta	<0·001	0·003	<0·002	<0·001	0·002	0·015	0·006	<0·003	0·014	<0·001	0·001	0·044	0·003	0·001	0·005	0·003	0·005	0·021	0·004
Pb	1·96	0·381	1·57	1·79	0·413	0·750	1·26	0·617	6·00	0·334	0·347	2·06	0·481	0·314	0·446	0·568	0·518	1·87	0·533
Th	0·069	0·078	0·016	0·053	0·169	1·16	0·580	0·048	0·471	0·025	0·014	2·19	0·037	0·021	0·216	0·051	0·213	1·71	0·675
U	0·039	0·027	0·016	0·045	0·066	0·479	0·235	0·013	0·118	0·009	0·004	0·614	0·023	0·005	0·070	0·008	0·043	0·298	0·147
La	0·690	3·11	0·869	0·64	3·11	10·4	2·54	2·78	3·12	2·46	1·52	3·86	2·35	2·21	5·16	3·71	5·58	16·4	14·7
Ce	2·64	10·8	3·38	1·75	11·3	31·9	11·0	11·0	9·28	11·0	5·53	10·4	9·41	8·02	16·4	13·6	16·6	43·1	38·0
Pr	0·533	1·99	0·686	0·253	1·96	4·98	1·89	1·81	1·20	1·74	1·05	1·52	1·75	1·47	2·79	2·50	2·74	6·44	5·91
Nd	2·78	11·3	4·39	1·31	10·9	25·9	10·0	10·1	6·17	9·84	6·30	7·70	10·4	8·75	15·5	14·4	15·0	32·9	31·5
Sm	0·906	3·48	1·17	0·339	3·40	7·29	3·29	2·38	1·58	2·72	2·16	2·12	3·51	2·80	4·82	4·32	4·20	8·50	8·39
Eu	0·279	0·934	0·349	0·092	1·02	1·94	1·04	0·840	0·510	0·870	0·592	0·633	0·964	0·802	1·34	1·10	1·16	2·38	2·21
Gd	0·906	3·10	1·10	0·277	3·04	6·45	3·01	2·06	1·85	2·65	1·88	2·00	3·35	2·50	4·45	3·94	3·59	7·07	7·90
Tb	0·139	0·457	0·169	0·043	0·496	0·980	0·540	0·348	0·246	0·409	0·304	0·298	0·543	0·413	0·636	0·620	0·540	1·03	1·12
Dy	0·756	2·77	1·06	0·30	2·63	5·22	3·08	1·73	1·48	2·17	1·79	1·78	3·30	2·40	3·74	3·39	2·90	5·69	6·08
Ho	0·142	0·538	0·193	0·058	0·513	1·03	0·583	0·328	0·314	0·381	0·337	0·385	0·612	0·455	0·729	0·643	0·527	1·11	1·15
Er	0·384	1·29	0·504	0·19	1·24	2·50	1·57	0·806	0·736	0·925	0·800	0·890	1·63	1·03	1·67	1·62	1·27	2·72	2·75
Tm	0·066	0·162	0·067	0·023	0·155	0·326	0·209	0·105	0·099	0·121	0·107	0·131	0·213	0·148	0·230	0·218	0·173	0·369	0·343
Yb	0·493	1·07	0·547	0·247	1·03	2·25	1·49	0·640	0·654	0·813	0·665	0·764	1·30	0·914	1·58	1·32	1·15	2·60	2·34
Lu	0·067	0·155	0·117	0·047	0·150	0·322	0·194	0·119	0·086	0·105	0·099	0·124	0·194	0·123	0·219	0·193	0·166	0·353	0·321

Downloaded from https://academic.oup.com/petrology/article/51/8/1617/1456692 by U.S. Department of Justice user on 17 August 2022

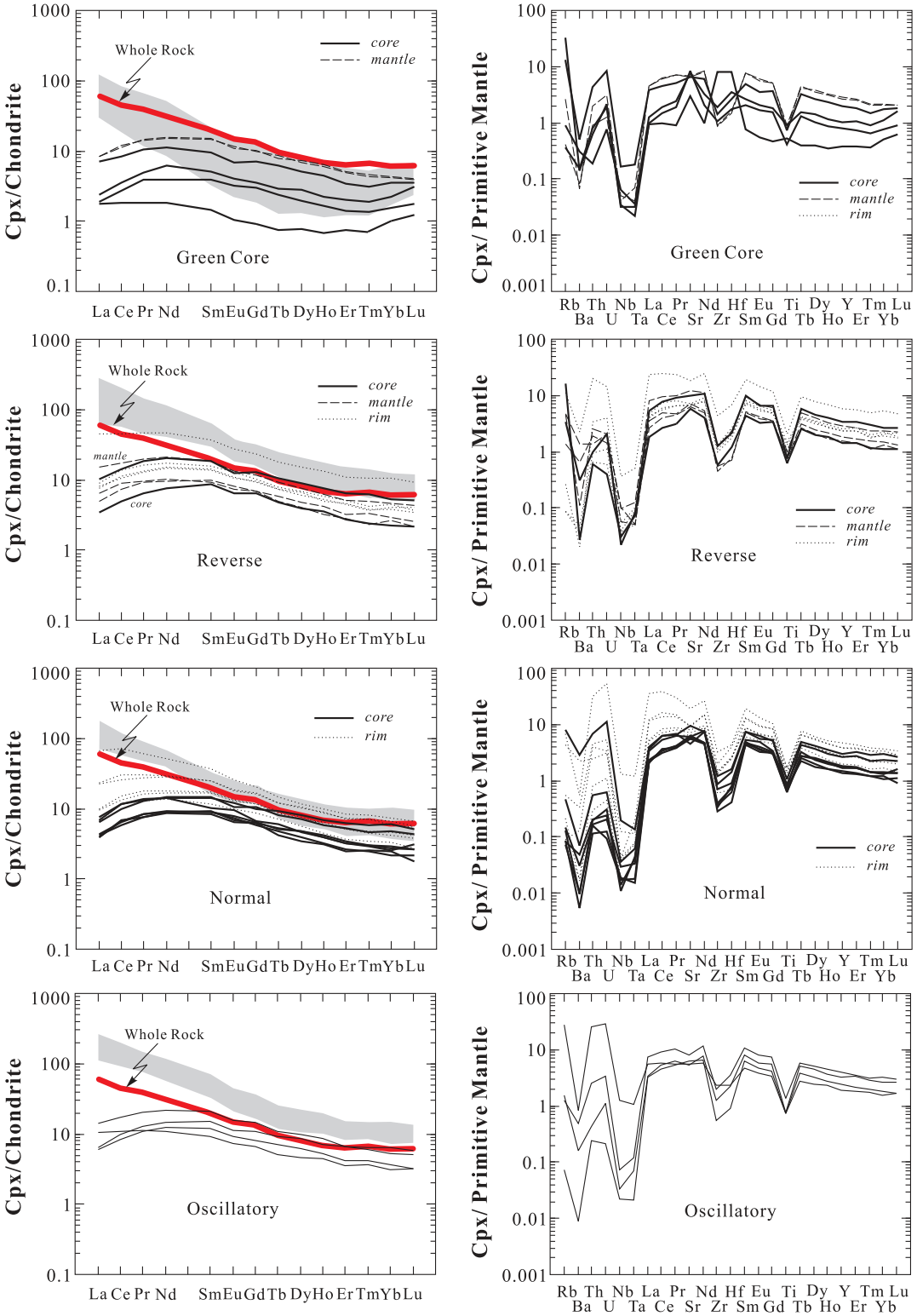

Fig. 11. Chondrite-normalized REE patterns and primitive mantle-normalized multi-element patterns for Cpx of the western Yunnan potassic and ultrapotassic rocks. The shaded areas show REE patterns for hypothetical silicate melts in equilibrium with Cpx phenocrysts in the corresponding panels, calculated using partition coefficients ($D^{cpx/melt}$) from the compilation of Ionov *et al.* (2002). Chondrite and primitive mantle normalization values are from Taylor & McLennan (1985) and Sun & McDonough (1989), respectively.

Downloaded from https://academic.oup.com/petrology/article/51/8/1617/1456692 by U.S. Department of Justice user on 17 August 2022

Table 10: Electron probe analyses of mica phenocrysts and inclusions in cpx phenocrysts

Mineral:	Mica phenocryst						Mica inclusion in cpx phenocryst				
Sample:	WZ10	WZ08	WZ07	WZ07	WZ05	WZ05	WZ05	WZ05	WZ05	WZ10	WZ10
Probe no.:	10-11	08-51	07-32	07-33	05-10	05-11	05-45	05-52	05-55	10-90	10-91
SiO_2	38·9	40·0	38·7	40·0	38·9	40·0	40·0	39·2	39·4	39·5	39·0
TiO_2	1·40	1·68	2·26	1·02	1·72	2·17	1·14	1·66	1·52	1·85	1·75
Al_2O_3	14·2	14·4	15·5	14·1	14·8	15·9	13·8	14·3	14·0	14·1	13·8
Cr_2O_3	1·21	0·34	0·17	0·55	0·34	0·49	1·34	1·16	1·11	0·95	1·25
FeO	6·36	7·77	7·78	6·19	7·11	5·32	7·40	7·22	7·13	6·92	7·96
MnO	b.d.l.	0·07	0·03	b.d.l.	b.d.l.	0·03	0·07	b.d.l.	0·06	0·05	0·04
MgO	22·1	20·9	20·8	22·9	22·7	20·7	21·6	22·0	22·0	21·9	21·2
CaO	0·07	b.d.l.	0·03	b.d.l.	0·10	b.d.l.	b.d.l.	b.d.l.	b.d.l.	b.d.l.	0·06
Na_2O	0·64	0·70	0·47	0·49	0·76	0·17	0·48	0·15	0·23	0·37	0·60
K_2O	9·70	9·68	10·01	10·09	9·68	10·45	10·06	10·55	10·46	10·26	9·76
NiO	b.d.l.	0·11	0·03	0·07	0·14	0·04	0·09	0·07	0·03	0·04	0·04
Total	94·58	95·65	95·78	95·41	96·25	95·27	95·98	96·31	95·94	95·94	95·46
Cations based on 22 oxygens per formula unit											
Si	5·639	5·776	5·612	5·771	5·710	5·846	5·829	5·632	5·683	5·664	5·634
Ti	0·154	0·184	0·248	0·112	0·191	0·239	0·125	0·181	0·166	0·201	0·192
Al^{IV}	2·361	2·224	2·388	2·229	2·290	2·154	2·171	2·271	2·317	2·336	2·366
Al^{VI}	0·095	0·258	0·277	0·200	0·119	0·578	0·204	0·000	0·095	0·069	0·011
Cr	0·140	0·039	0·019	0·063	0·039	0·056	0·155	0·133	0·127	0·109	0·144
Fe^{3+}	0·000	0·000	0·000	0·000	0·000	0·000	0·000	0·000	0·000	0·000	0·000
Fe^{2+}	0·778	0·949	0·951	0·633	0·881	0·649	0·903	0·875	0·869	0·838	0·971
Mn		0·008	0·004			0·004	0·008		0·008	0·006	0·005
Mg	4·824	4·545	4·545	4·972	4·781	4·499	4·695	4·866	4·775	4·718	4·621
Ca	0·011		0·005		0·015						0·009
Na	0·181	0·198	0·134	0·139	0·217	0·047	0·137	0·042	0·066	0·104	0·170
K	1·812	1·803	1·812	1·868	1·736	1·920	1·760	1·988	1·889	1·949	1·871
Ni		0·013	0·004	0·008	0·017	0·005	0·011	0·008	0·003	0·004	0·005
Mg/Fe	6·20	4·79	4·78	7·86	5·42	6·93	5·20	5·56	5·49	5·63	4·76

Fe^{2+} and Fe^{3+} are recalculated with the charge balance method of Droop (1987); b.d.l., below detection limit.

phenocrysts records magma compositional variation during crystal growth. Thus zoning in the clinopyroxenes of the western Yunnan potassic and ultrapotassic rocks can provide insights into the magma evolution processes.

All the cpx crystals studied are characteristically depleted in Al_2O_3. The amount of Al is insufficient to compensate for the deficiency of Si in the tetrahedral site (Table 8). This peculiar characteristic resembles that of cpx from lamproitic and kamafugitic rocks (e.g. Mitchell & Bergman, 1991; Cellai *et al.*, 1994; Conticelli, 1998; Perini & Conticelli, 2002; Çoban & Flower, 2006). The essentially constant Ti/Al ratios within a given lava suite make Ti/Al a useful parameter (Cundari & Salviulo, 1989; Dobosi & Fodor, 1992) in classifying calcic cpx in potassic rocks (e.g. Conticelli, 1998; Mitchell & Bergman, 1991; Perini & Conticelli, 2002; Streck *et al.*, 2005) (Fig. 14). The western Yunnan cpx, except for the green cores, defines a trend plotting in the transitional region between lamproites and Group III potassic lavas (Fig. 14).

The green cores in the western Yunnan cpx are sub-rounded and show strong resorption textures (Fig 2d and 9c). The green cores could be xenocrysts from surrounding wall-rocks (Barton & Van Bergen, 1981; Dobosi, 1989; Dobosi & Fodor, 1992) or have crystallized from an evolved magma that subsequently mixed with a more primitive magma (Barton & Van Bergen, 1981; Duda & Schmincke, 1985; Dobosi, 1989). Their distinctively different Ti/Al ratios (Fig. 14) and low Mg-number (<0·7; Fig. 10)

Downloaded from https://academic.oup.com/petrology/article/51/8/1617/1456692 by U.S. Department of Justice user on 17 August 2022

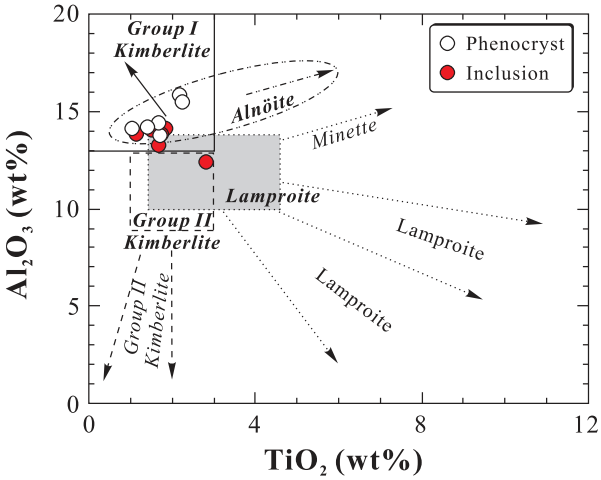

Fig. 12. Variation of Al_2O_3 and TiO_2 in phlogopite of the western Yunnan potassic and ultrapotassic rocks. Group I kimberlites, Group II kimberlites (orangeite), lamproite and alnöite phlogopite compositional fields (outlines) and evolutionary trends (arrows) are modified after Mitchell (1995).

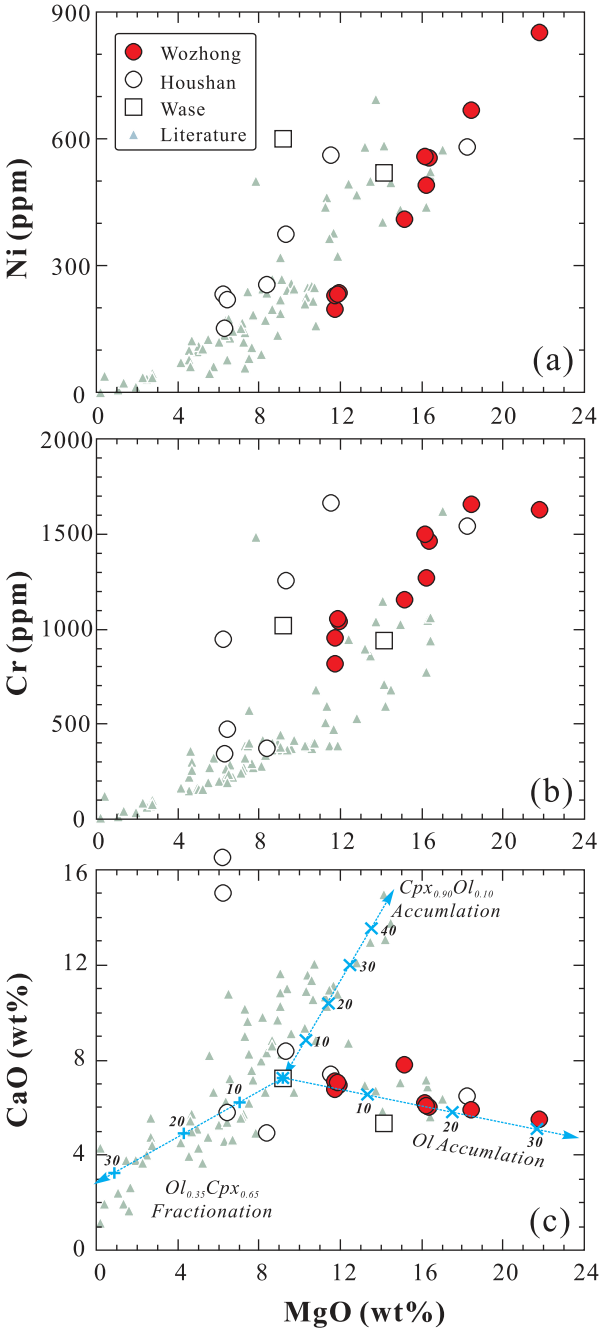

Fig. 13. (a, b) Ni and Cr vs MgO; (c) CaO vs MgO, indicating olivine and/or clinopyroxene accumulation in high-Mg samples and extensive fractionation of clinopyroxene, olivine for low-Mg samples; mineral compositions of Ol (Fo = 92), Cpx (Mg-number = 0·90) were assumed in the calculation.

indicate that the green cores are likely to have a different origin from the other cpx crystals and may have crystallized from a highly evolved melt (e.g. Mg-number < ~0·35; Stone & Niu, 2009) depleted in incompatible elements. Although the cpx phenocrysts in the trachytes also have high Na and low Cr contents (Fig. 10c and d), the green cores could not be derived from such evolved trachyte melts because of their very low Mg-number and Ti (Fig. 10). Therefore, the green cores in the western Yunnan cpx may be of xenocrystal origin. This inference is supported by *in situ* trace element data (Fig. 11), which show that the melts in equilibrium with the green cpx cores (assumed to be of magmatic origin) are distinct from the host rocks with a convex-downward REE pattern from Gd to Lu (Fig. 11). Because high Na, Al, Al^{VI}/Al^{IV} and Cr and low Ti/Al are characteristic of cpx crystallized at high pressures (i.e. with a high jadeitic component; Wass, 1979; Dobosi & Fodor, 1992; Haase *et al.*, 1996), the green cores of the western Yunnan cpx could have crystallized at high pressures; however, their low Cr values could be due to the highly evolved (Mg-number < ~0·35) nature of the parent melt (e.g. Schiano *et al.*, 1998; Ishimaru & Arai, 2008). As most Na is balanced by Fe^{3+} (Table 8), the green cores have a large aegirine component (~10 mol %) but not a significant jadeite component (<2%); thus, they are not 'omphacitic' in composition like pyroxenes of high-pressure metamorphic origin.

In summary, we interpret the green cores of the western Yunnan cpx as xenocrysts entrained from adjacent wall-rocks during magma ascent. The melts in equilibrium with the other cpx compositions all show LREE-enriched REE patterns resembling those of the whole-rocks, though at higher concentration levels (Fig. 11), suggesting a genetic affinity with the host-rocks. The reverse zoning reflects replenishment of a more primitive melt into an evolving or already fairly evolved magma body. The oscillatory

Downloaded from https://academic.oup.com/petrology/article/51/8/1617/1456692 by U.S. Department of Justice user on 17 August 2022

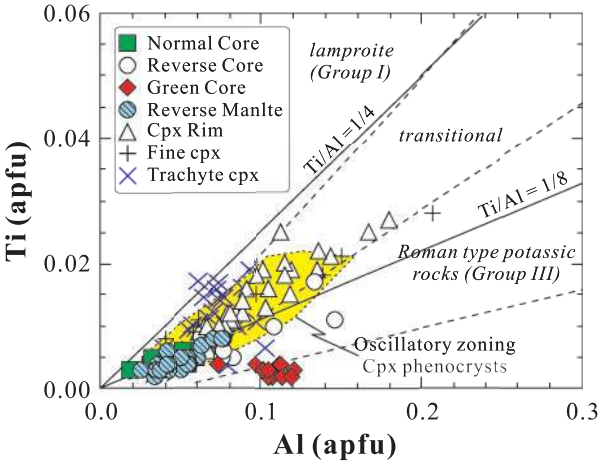

Fig. 14. Variation of Al and Ti cations per formula unit in Cpx. Fields (separated by dashed lines) indicate Cpx compositions for lamproite (Group I), Roman type potassic and ultrapotassic rocks (Group III) and transitional rock types (Conticelli, 1998; Perini & Conticelli, 2002).

zoning indicates multi-stage injection of primitive magma into evolved or evolving magma chambers, which can be described by processes in 'periodically replenished, periodically tapped, and continuously fractionated magma chambers' (O'Hara & Mathews, 1981). Magma mixing is a common phenomenon of such magma chamber processes in the western Yunnan mafic potassic and ultrapotassic rocks.

Spinel constraints on magma sources

The significant correlation between spinel Mg-number and host olivine Fo content (Fig. 8b) suggests one of the following scenarios: (1) the spinel and olivine are both liquidus phases whose changing Mg-number reflects magmatic evolution, or (2) there is significant post-magmatic re-equilibration between the two phases. For spinels included in low-Fo olivine, scenario (1) is unlikely because the Cr-number of the spinel is very high (mostly >0·75) with no correlation with olivine Fo content and spinel cannot be a liquidus phase in a highly evolved melt. This is consistent with scenario (2) in which primitive spinel (high Cr-number) has re-equilibrated with the host olivine in terms of Fe–Mg exchange (Fig. 8b). The fact that Ti, Al and Cr are incompatible in olivine (vs spinel) explains why these elements are unaffected by the spinel–olivine re-equilibration and have little or limited variation in the spinels (Table 7; Fig. 8a). This implies that all these spinel inclusions are of a common origin, and their original compositions (prior to the re-equilibration) are likely to have an Mg-number of ~0·6 and Cr-number of ~0·85 (Fig. 8a and b). Although such spinels would plot in the field of highly depleted mantle harzburgite (Fig. 8a), the very high Cr-number of these spinels is more consistent with their being a liquidus phase (i.e. chromite-rich) co-precipitated with Mg-rich olivine as in most dunite suites (e.g. Dick & Bullen, 1984).

The abundances of Al_2O_3, Cr_2O_3 and TiO_2 in spinels can be used to infer the compositions of their parental melts (Kamenetsky *et al.*, 2001). The high Cr-number (mostly >0·75) and low Al_2O_3 contents (<10 wt %) indicate that the western Yunnan Cr-spinels may have crystallized from highly depleted parental melts, probably derived from a harzburgite source (Green *et al.*, 2001; Kamenetsky *et al.*, 2001) (Fig. 8a). The diagram of Al_2O_3 vs TiO_2 has been used to discriminate between spinels crystallized from magmas in different geodynamic settings (Fig. 15a; Kamenetsky *et al.*, 2001). The TiO_2 content in most of the western Yunnan spinels is <1·0 wt %, and they mostly plot in the ARC field (Fig. 15a), suggesting that the majority of the olivine phenocrysts may have crystallized from melts derived from a metasomatized lithospheric mantle source.

A small number of the western Yunnan spinels have high TiO_2 contents (>1·0 wt %), and plot close to the field of spinels from large igneous provinces (LIPs; Fig. 15a). Xu *et al.* (2001*a*, 2001*b*, 2004) have suggested that high-Mg basalts may have underplated and intruded the lower crust during the Emeishan LIP magmatism in the late Permian. The high-Ti spinels are unlikely to have been derived from cumulate rocks associated with the LIP magmatism because their low Al_2O_3 content distinguishes them from the high-Ti and -Cr spinels in high-Mg olivine phenocrysts in the Emeishan picrites (TiO_2 = 1·85–1·96 wt %, Cr-number = 0·73–0·75; Zhang *et al.*, 2006) (Fig. 15a). Additionally, the TiO_2 content of the high-Ti spinels shows a negative correlation with Al_2O_3 (Fig. 15a) and with the chromite component (Fig. 15b), and a positive correlation with the magnetite component (Fig. 15b), suggesting that high-TiO_2 spinel inclusions have high magnetite contents. Some high-Ti spinels are actually titanomagnetites because their magnetite component is even higher than the chromite component (Fig. 15b). Titanomagnetite is a liquidus phase in highly evolved melts at the basaltic-andesite stage, where Ti–Fe oxide crystallization leads to Ti–Fe depletion and SiO_2 enrichment in the melt (e.g. Stone & Niu, 2009). However, high-Cr spinel or chromite along with high-Mg olivine is the earliest liquidus phase, which explains why chromite deposits are always associated with dunites (e.g. Dick & Bullen, 1984; Stone & Niu, 2009). Thus the continuing and inverse chromite–magnetite trend with increasing TiO_2 in Fig. 15b is consistent with magma chamber processes—involving mixing between primitive and highly evolved melts and re-equilibration of their 'liquidus phases'. The positive magnetite–TiO_2 trend is consistent with the spinels having crystallized from highly evolved melts with varying TiO_2 contents. The inverse chromite–TiO_2 trend is best interpreted as evidence for earlier primitive chromite

Downloaded from https://academic.oup.com/petrology/article/51/8/1617/1456692 by U.S. Department of Justice user on 17 August 2022

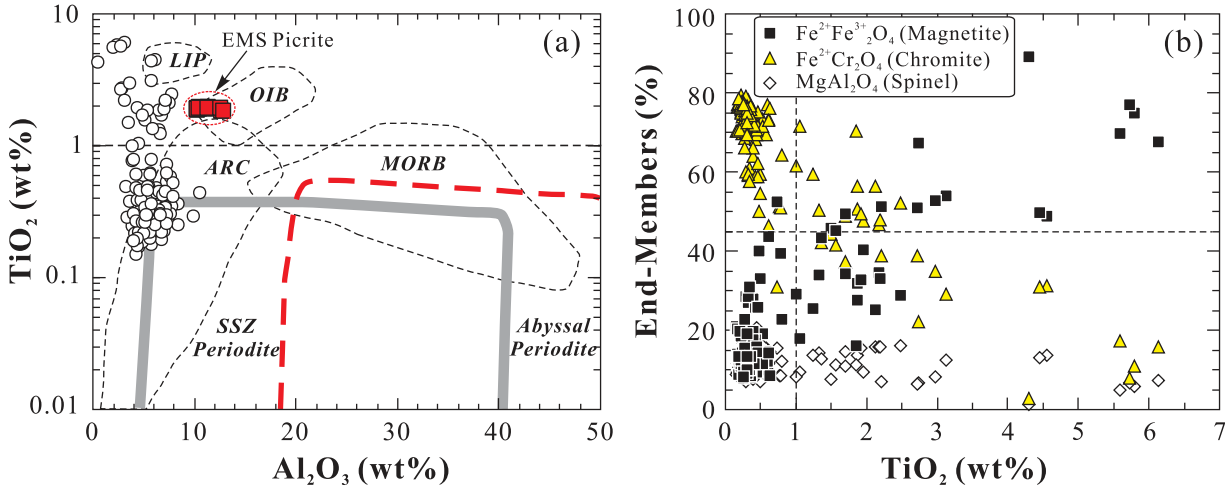

Fig. 15. (a) Al_2O_3 vs TiO_2 diagram, discriminating spinels crystallized from basaltic melts associated with large igneous provinces (LIP), intra-plate ocean islands (OIB), island arcs (ARC) and ocean ridges (MORB) (after Kamenetsky *et al.*, 2001) and spinels in mantle peridotites from supra-subduction zone (SSZ) and ocean ridge settings (i.e. abyssal peridotites) (Kamenetsky *et al.*, 2001). Spinel inclusions in olivine phenocrysts in the Emeishan picrites are plotted for comparison (Zhang *et al.*, 2006). (b) Plot of end-member percentage vs TiO_2 of spinel inclusions; the high TiO_2 contents of a small number of spinel inclusions correlate with complementary trends of chromite and magnetite, indicating that these spinels are liquidus phases in a progressively more evolved melt from chromite to titanomagnetite.

re-equilibrated with a highly evolved TiO_2-rich melt. Obviously, these two scenarios are not in isolation, and both are consequences of complex magma chamber processes.

Origin of high magnesian olivine in ultrapotassic magmas

Some olivine phenocrysts in the western Yunnan potassic and ultrapotassic rocks have very high forsterite contents ($Fo_{93–94}$). A genetic link with the late Permian Emeishan flood basalt province was favored in our earlier interpretation of these olivines as xenocrysts from the lithospheric mantle because the Emeishan flood basalt magmatism is the only known geological event in the region that could have produced high-Mg olivines (Xu *et al.*, 2003). In addition, available seismic tomography data show the presence of a thick (~20 km) high-velocity lower crust (HVLC) ($V_p = 7·1–7·8$ km/s) in the west Yangtze craton (Liu *et al.*, 2001), which may be genetically associated with the Emeishan LIP magmatism (Xu *et al.*, 2003, 2004). However, the presence of abundant low-Ti spinel inclusions with high Cr-number and low Al_2O_3 in olivine phenocrysts in the western Yunnan potassic and ultrapotassic rocks suggests that these cannot come from the HVLC but instead formed as phenocrysts within the ultrapotassic magmas.

The compositions of liquidus olivines can be used to calculate the Mg-number of the parental melts using the well-established olivine–melt Fe–Mg exchange phase equilibrium (Roeder & Emslie, 1970). For example, to produce olivine with Fo = 93–94, a melt with Mg-number = 0·799–0·825 is needed if using the exchange partition coefficient K_D $([Fe^{2+}/Mg]^{ol}/[Fe^{2+}/Mg]^{melt}) = 0·30 \pm 0·03$ (Roeder & Emslie, 1970). The calculation would give as much as 17·9–21·1 wt % MgO in the melt if FeO = 8 wt % is assumed. This would then give unrealistically high liquidus (eruption) temperatures in excess of 1500°C. Magma with such high liquidus temperatures is unlikely in the western Yunnan region during the Cenozoic in the absence of evidence for mantle plumes. High-Fo olivine has also been reported in boninites (Crawford, 1989) and olivine lamproites (Jaques *et al.*, 1984; Mitchell & Bergman, 1991) that are derived from metasomatized refractory mantle lithosphere. The composition of the spinel inclusions (Figs 8 and 15) and the whole-rock geochemical data all suggest that the magmas result from partial melting of a metasomatized harzburgite source. Thus we conclude that the high-Mg olivines in the western Yunnan potassic and ultrapotassic rocks are phenocrysts from magmas derived from metasomatized refractory mantle lithosphere. Because the olivine Fo content is proportional to the Mg-number of the melt (i.e. $[Fe^{2+}/Mg]^{ol} = K_D\ [Fe^{2+}/Mg]^{melt}$), the high-Mg olivines must reflect the high Mg-number of the parental melt. Although this is conceptually straightforward, to derive the Mg-number of the parental melt from the compositions of the bulk-rock samples is not straightforward because the bulk-rock samples do not represent liquids (unless they are aphyric) but mixtures of melt and phenocrysts. Additionally, because Mg-number (melt) = $Mg/[Mg + Fe^{2+}]$ (melt), and most analytical methods only give total Fe rather than both Fe^{2+} and Fe^{3+}, a further source of uncertainty is introduced.

Downloaded from https://academic.oup.com/petrology/article/51/8/1617/1456692 by U.S. Department of Justice user on 17 August 2022

The above simple analysis is conceptually important and argues against the commonly made statement that 'the olivine phenocrysts are in equilibrium with bulk-rock Mg-number', which is misleading because the bulk-rocks are not melts, but mechanical mixtures of melt and phenocrysts. Furthermore, assuming that $K_D = 0{\cdot}30 \pm 0{\cdot}03$ (Roeder & Emslie, 1970) is applicable to the western Yunnan potassic and ultrapotassic magmas, then a parental melt Mg-number of 0·799–0·825 is required to explain the primitive olivine compositions of Fo_{93-94}. This in turn requires very low Fe^{2+}/Fe_{Tot} in the melt. This is, however, not obvious from the bulk-rock analyses. If the groundmass of the porphyritic samples did represent the quenched melt in equilibrium with the olivine crystals, then the groundmass (or melt) must be very oxidized with a very high Fe^{3+}/Fe_{Tot} or $Fe^{3+}/[Fe^{3+} + Fe^{2+}]$, hence very low Fe^{2+}/Fe_{Tot} or very high Mg-number. Because spinel–olivine re-equilibration by means of Fe^{2+}–Mg exchange (see Fig. 8b) will not affect Fe^{3+} in the spinels, the calculated $\Delta\log(fO_2)$ using spinel–olivine pairs (Ballhaus *et al.*, 1990) for the high-Mg olivine (Fo > 90%) gives a likely fO_2 for the melt, which varies from 1·19 to 2·65 (with a mean of 1·81 ±0·66) log units above the FMQ buffer. By assuming that the fO_2 calculated from the liquidus spinels (i.e. those inclusions in olivines of Fo > 90; see Fig. 8 and discussion above) represents the fO_2 of the melt (groundmass) of the samples, we can calculate Fe^{2+}/Fe_{Tot} in the melt using the equation ($Fe^{2+}/Fe_{Tot} = 0{\cdot}1386e^{0{\cdot}3772X}$; X is $\Delta\log(fO_2)$ for the FMQ buffer; $R^2 = 0{\cdot}94$) derived from Botcharnikov *et al.* (2005). For example, for a high-fO_2 system at 1·8 log units above the FMQ buffer (see Fig. 8c), the Fe^{2+}/Fe_{Tot} ratio or Mg-number of the melt would be about 0·73. The Mg-number of the melt can be derived from the bulk-rock by eliminating the effects of olivine accumulation. However, the proportion of olivine phenocrysts estimated from thin section (Table 1) cannot be used for the calculation because what is observed in thin section cannot reflect the composition of the sample powders used for the analysis of such highly porphyritic rocks. Ni is strongly compatible in olivine, and the strong linear correlation of bulk-rock MgO with Ni in the western Yunnan mafic potassic and ultrapotassic rocks is a straightforward consequence of olivine accumulation in the bulk-rock samples (Fig. 13). The bulk-rock Ni contents can be used for evaluating the effect of olivine accumulation for each sample (Fig. 16). The calculated Mg-number values for the 'melt' are high enough for the melt to be in equilibrium with the high-Fo olivines (Fig. 16). That is, high-Fo olivines in ultrapotassic melts may very well result from the high Mg-number of the melt as a result of the high fO_2 of the system (high Fe^{3+}/Fe_{Tot}, thus low Fe^{2+}/Fe_{Tot} and high Mg-number). This also suggests that caution is necessary when discussing olivine–melt phase equilibria without knowing the fO_2 of the magmatic system.

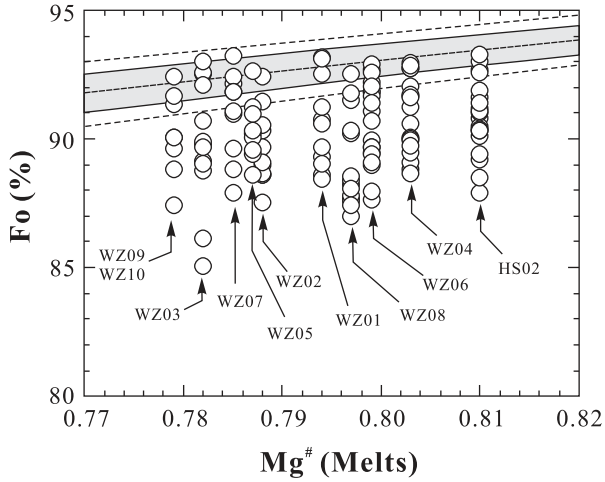

Fig. 16. Variation range of Fo in olivine phenocrysts plotted as a function of 'host melt' Mg-number for single samples of the western Yunnan mafic potassic and ultrapotassic rocks. Mg-number (Melts) is derived from modified bulk-rock MgO and FeO (Table 3) by eliminating olivine accumulation effects and calculating Fe^{2+}/Fe_{Tot} at $\Delta\log(fO_2)$ of +1·8 (FMQ buffer, which is the mean value for spinels in olivines with Fo > 90 in Fig. 4c) based on the relation between Fe^{2+}/Fe_{Tot} ratio and $\Delta\log(fO_2)$ in hydrous ferro-basaltic melts (Botcharnikov *et al.*, 2005). Proportion of olivine accumulation in each sample was calculated by assuming (1) Ni = 120 ppm in the 'actual melt' without olivine accumulation; (2) Ni = 3000 ppm and Fo = 92 for average olivines with Fo > 90% (Fig. 7c). The shaded area defines the range of olivine compositions calculated to be in equilibrium with melts of varying Mg-number. In the calculation, K_D ($[Fe^{2+}/Mg]^{ol}/[Fe^{2+}/Mg]^{melt}$) = 0·30 ± 0·03 (Roeder & Emslie, 1970) is used, and the limits with $K_D = 0{\cdot}30 \pm 0{\cdot}05$ (dashed line) are shown for reference.

In addition, estimates from spinel inclusions in olivine phenocrysts (Table 7) and high Fe^{3+}/Fe^{2+} ratios in cpx (Table 8) all suggest a high fO_2 in the magmas. The high fO_2 of the parental magmas is most probably inherited from the more oxidized mantle source material, for which mantle metasomatism is the best candidate process (e.g. Ballhaus *et al.*, 1990; McGuire *et al.*, 1991; Sato & Wright, 1996; McCammon *et al.*, 2001; Holloway, 2004; Lee *et al.*, 2005).

Origin of Ta–Nb–Ti depletion and implication for lithosphere evolution beneath western Yangtze craton

The western Yunnan potassic and ultrapotassic rocks exhibit strong relative depletion of Nb, Ta and Ti (Fig. 5) and have enriched Sr–Nd isotopic compositions (Fig. 6) (Chung *et al.*, 1998; Deng *et al.*, 1998*a*; Wang *et al.*, 2001; Xu *et al.*, 2001*a*; Li *et al.*, 2002; Guo *et al.*, 2005; Mo *et al.*, 2006; this study). The origin of such geochemical features could be due to the presence of recycled terrigenous sediments in the mantle source region (Peccerillo, 1985; Conticelli & Peccerillo, 1992; Hawkesworth *et al.*, 1993; Zhao *et al.*, 2009), supra-subduction zone fluid metasomatism

Downloaded from https://academic.oup.com/petrology/article/51/8/1617/1456692 by U.S. Department of Justice user on 17 August 2022

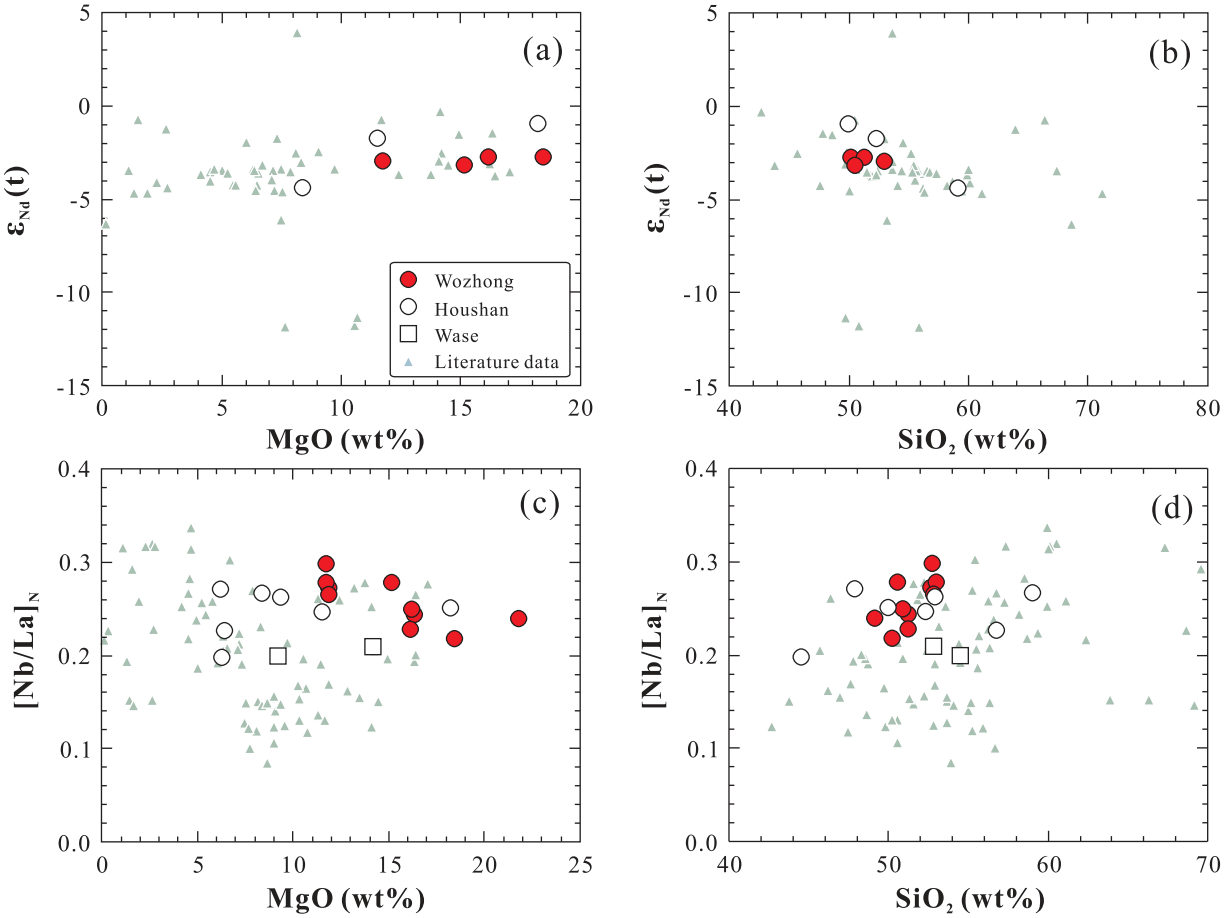

Fig. 17. (a, b) Variation of $\varepsilon_{Nd}(t)$ vs MgO and SiO_2; (c, d) $[Nb/La]_N$ vs MgO and SiO_2. Data sources are as Fig. 4.

(Tatsumi, 1986; Donnelly *et al.*, 2004) or crustal contamination during magma ascent (Nelson *et al.*, 1986; Bernard-Griffiths *et al.*, 1991).

Crustal contamination?

Crustal contamination of mantle-derived melts during their ascent and eruption from magma chambers is inevitable. This is also true for the western Yunnan potassic and ultrapotassic rocks, as indicated by the slight decrease in $\varepsilon_{Nd}(t)$ with increasing SiO_2 and decreasing MgO except for some samples from Wang *et al.* (2001) and Guo *et al.* (2005) (Fig. 17a and b). Thus crustal contamination might be a possibility to explain the negative Ta–Nb–Ti anomalies of the western Yunnan potassic and ultrapotassic rocks. However, the $[Nb/La]_N$ values of the western Yunnan samples (Table 3; Fig. 17c and d) are even lower than the mean value of the lower continental crust ($[Nb/La]_N = 0{\cdot}6$; Rudnick & Gao, 2003), indicating that the strong negative Nb–Ta anomalies in the trace element patterns of the western Yunnan potassic and ultrapotassic rocks cannot be caused by crustal contamination or assimilation, although the latter could have an added effect. Crustal contamination, if any, might have enhanced the $[Nb/La]_N$ of the western Yunnan potassic and ultrapotassic rocks, as suggested by an weak increase of $[Nb/La]_N$ with increasing SiO_2 and decreasing MgO (Fig. 17c and d). In short, crustal assimilation must have played a role in the petrogenesis of the western Yunnan potassic and ultrapotassic rocks, but the effect is insignificant in explaining the distinctive negative Ta–Nb–Ti anomalies in these rocks.

Subduction-related mantle metasomatism?

Wang *et al.* (2001) suggested that continental subduction during an early period of transpression along the Ailao Shan–Red River fault zone may have induced fluid infiltration into the mantle wedge, which later became the source for the western Yunnan potassic and ultrapotassic magmatism. However, the western Yunnan potassic and ultrapotassic rocks are not restricted to the Ailao Shan–Red River fault zone, but are distributed widely into the far interior of the western Yangtze Craton (Guo *et al.*, 2005). On the other hand, others have suggested that the western Yunnan mantle source region for these rocks must

Downloaded from https://academic.oup.com/petrology/article/51/8/1617/1456692 by U.S. Department of Justice user on 17 August 2022

have experienced enrichment by subduction-derived fluids in its geological past because the western Yunnan potassic and ultrapotassic magmatism is spatially removed from contemporaneous subduction zones (Zhu *et al.*, 1992; Chung *et al.*, 1998; Li *et al.*, 2002; Guo *et al.*, 2005; Mo *et al.*, 2006). Guo *et al.* (2005) considered two separate enrichment events, one associated with Proterozoic subduction and the other with Paleozoic Paleo-Tethyan seafloor subduction. However, in the western region of the Yangtze craton, the Late Paleozoic Emeishan LIP magmatism (Xu *et al.*, 2001*b*, 2004, 2007) would have affected the lithospheric mantle beneath the Yangtze craton and purged the lithospheric mantle of all or much of its fusible constituents (Gallagher & Hawkesworth, 1992; Xu *et al.*, 2001*a*, 2001*b*, 2004, 2007). Both the high Cr-number of the chromium spinels and high Cr, Ni and low TiO_2 contents of the rocks further indicate that the mantle source region for the western Yunnan potassic and ultrapotassic rocks may have been highly depleted, perhaps representing melting residues associated with melt extraction of the Emeishan LIP magmatism (Xu *et al.*, 2004). Importantly, there is no evidence for ocean crust subduction beneath, and to the west of, the Yangtze craton since the late Paleozoic (Wang *et al.*, 2000). Although the Jinshajiang–Ailaoshan suture zone is interpreted to represent the Palaeo-Tethyan ocean from the early Carboniferous to middle Triassic (Wang *et al.*, 2000; Sun & Jian, 2004), there is evidence for westward subduction of that ocean floor beneath the eastern margin of the Changdu–Simao Block (Mo *et al.*, 1993; Wang *et al.*, 2000; Sun & Jian, 2004) (Fig. 1a). Thus, Paleozoic Paleo-Tethyan westward seafloor subduction cannot be responsible for the metasomatism of the western Yunnan mantle lithosphere. In addition, the western Yunnan potassic and ultrapotassic rocks have distinctively lower initial $^{207}Pb/^{204}Pb$ and $^{208}Pb/^{204}Pb$ but higher initial $^{143}Nd/^{144}Nd$ ratios than post-collisional shoshonitic volcanic rocks from Tibet (Fig. 6), which is in contradiction to the interpretation of ancient subduction processes being responsible for the metasomatism of the Tibetan sub-continental lithospheric mantle source of the subsequent K-rich magmatism (Turner *et al.*, 1996; Miller *et al.*, 1999; Ding *et al.*, 2003; Chung *et al.*, 2005; Guo *et al.*, 2006; Mo *et al.*, 2006).

Carbonatite metasomatism

Long-term isolation of a metasomatized mantle lithospheric domain (McKenzie, 1989; Thompson & Gibson, 1994) could produce extremely enriched Sr–Nd isotopic compositions. Such processes, however, cannot account for the highly fractionated LILE and HFSE observed in the ultrapotassic rocks (Peccerillo, 1985; Conticelli *et al.*, 2009). On the other hand, carbonatitic melts are considered to be effective metasomatic agents to account for Ta–Nb–Ti relative depletion (Ionov *et al.*, 1993; Yaxley *et al.*, 1998; Guzmics *et al.*, 2008). Carbonatite metasomatism can also explain the enriched Sr–Nd isotopic compositions because the carbonatites have high Rb/Sr and low Sm/Nd as well as high Sr and LREE abundances relative to ocean island basalt (OIB) and mid-ocean ridge basalt (MORB)-like melts (Table 11). The western Yunnan potassic and ultrapotassic rocks show very similar Sr–Nd–Pb isotope compositions to Paleogene carbonatites in western Sichuan, SW China (Hou *et al.*, 2006; see Fig. 6). Thus it is possible that the mantle lithosphere beneath the western Yangtze craton may have undergone H_2O–CO_2-rich melt modification. The model calculations shown in Fig. 18 and Table 11 also suggests that addition of a very small amount (2%) of carbonatitic melt to a depleted mantle source can lead to enrichment in many incompatible elements but relative Ta–Nb–Ti depletion in the resultant melt (Fig. 18).

The strong enrichment of LILE (e.g. K, LREE, Th and U) can result in apparent Ta–Nb–Ti depletion. However, carbonatite-related enrichment cannot account for the marked enrichment of Ba, K, Rb, Cs, Th and U in the western Yunnan potassic and ultrapotassic rocks (Fig. 18); a pure carbonatite-metasomatized source is also inadequate in explaining the Ti depletion (Fig. 18). In addition, the mafic samples are characterized by low Al_2O_3 and FeO_{Tot} (Table 3) similar to magmas from cpx-poor lithospheric mantle sources. The occurrence of a carbonatitic component would have re-fertilized the mantle source with newly formed cpx. Thus although carbonatite melts may exist they cannot be the primary metasomatic agent within the mantle lithosphere beneath the western Yangtze craton (Fig. 6).

Fractional crystallization of Ti-bearing minerals

The positive correlation between $[Nb/La]_N$ and Ti/Ti* ($=2Ti_{PM}/[Sm_{PM} + Tb_{PM}]$) of the western Yunnan mafic potassic and ultrapotassic rocks (Fig. 19a) indicates that Ti-bearing minerals (e.g. Ti-bearing amphiboles, ilmenite or rutile) play an important role in the petrogenesis of these rocks either as liquidus phases during fractional crystallization or as residual phases during partial melting in the source region. Fractional crystallization of ilmenite and rutile can induce negative Ta–Nb–Ti anomalies in the melt (e.g. Foley *et al.*, 1987; Klemme *et al.*, 2005, 2006; Xiong *et al.*, 2005). However, the mostly subchondritic Nb/Ta ratios in ilmenite or rutile suggest that crystallization of these phases will result in high and superchondritic Nb/Ta ratios in the residual melts (Xiong *et al.*, 2005; Klemme *et al.*, 2006). Nevertheless, the western Yunnan mafic potassic and ultrapotassic rocks have subchondritic (vs superchondritic) Nb/Ta ratios of 13·9–16·3 (Table 2; Fig. 19b; compared with the chondritic value of 17·4 (Sun & McDonough, 1989)). We thus infer that ilmenite or rutile crystallization cannot be the primary cause of the Ti-depletion in these rocks.

Pargasite and kaersutite amphiboles are stable up to 1150°C and ~3·0 GPa under water-undersaturated

Downloaded from https://academic.oup.com/petrology/article/51/8/1617/1456692 by U.S. Department of Justice user on 17 August 2022

Table 11: Average and model compositions

	N-MORB [1]	OIB [1]	Carbonatite [2]	Amphibole [3]	Melt-1 10%FC	Melt-2 20%FC	Melt-3 30%FC	Melt-4 40%FC	Melt-5 50%FC
Ba	6·3	350	13882	297	335	372	420	483	570
Th	0·12	4	5·5	0·55	0·51	0·57	0·65	0·76	0·91
U	0·047	1·02	9·62	0·22	0·33	0·37	0·42	0·49	0·59
Ta	0·132	2·7	0·11	3·69	0·30	0·32	0·35	0·38	0·42
Nb	2·33	48	13·5	78·3	5·51	5·77	6·07	6·45	6·92
La	2·5	37	941	13·4	25·4	27·9	31·1	35·2	40·7
Ce	7·5	80	1522	49·2	44·9	48·3	52·4	57·6	64·4
Pb	0·3	3·2	963		21·7	24·1	27·2	31·3	36·9
Pr	1·32	9·7	139	7·36	4·79	5·05	5·35	5·73	6·21
Nd	7·3	38·5	427	35·4	18·05	18·61	19·26	20·04	21·01
Sr	90	660	23028	681	633	693	769	866	998
Sm	2·63	10	50·1	9·41	3·86	3·68	3·49	3·28	3·04
Hf	2·05	7·8	0·33	3·64	2·46	2·59	2·73	2·91	3·13
Zr	74	280	10·1	121	90·7	97·5	106	116	130
Ti	7600	17200	240	24526	6298	4801	3530	2475	1626
Eu	1·02	3	13·9	3·21	1·34	1·28	1·22	1·15	1·08
Gd	3·68	7·62	41·4	8·50	4·33	3·98	3·62	3·24	2·84
Tb	0·67	1·05	3·68	1·17	0·68	0·60	0·53	0·45	0·37
Dy	4·55	5·6	14·1	5·76	4·22	3·66	3·11	2·58	2·06
Ho	1·01	1·06	2·34	1·11	0·91	0·78	0·66	0·54	0·43
Y	28	29	72·3	28·7	25·5	22·0	18·7	15·5	12·4
Er	2·97	2·62	6·82	2·67	2·64	2·27	1·91	1·56	1·23
Tm	0·456	0·35	0·76	0·32	0·39	0·33	0·27	0·22	0·17
Yb	3·05	2·16	3·98	1·96	2·54	2·10	1·69	1·32	0·98
Lu	0·455	0·3	0·52	0·26	0·38	0·32	0·26	0·20	0·16
Nb/Ta	17·7	17·8	123	21·2	18·2	17·8	17·4	16·9	16·4
Nb/Zr	0·031	0·171	1·33	0·645	0·061	0·059	0·057	0·055	0·053
Ti/Ti*	0·96	0·82	0·003	1·18	0·65	0·53	0·43	0·33	0·24
$[Nb/La]_N$	0·91	1·27	0·014	5·71	0·21	0·20	0·19	0·18	0·17

Model calculation is described in Fig. 18. Data sources: [1] Sun & McDonough (1989); [2] average of Daluxiang (Xu *et al.*, 2008) and Daluocao (Hou *et al.*, 2006) carbonatite veins at western Yangtze Craton; [3] average of Ti-rich amphibole in mantle xenoliths of Antarctica from Coltorti *et al.* (2004).

conditions (Niida & Green, 1999); these amphiboles can be important hosts for Ta, Nb and Ti (Ionov & Hofmann, 1995; Tiepolo *et al.*, 2000, 2001; Coltorti *et al.*, 2007) (Fig. 19a). During melt ascent through the lithosphere, cooling can cause amphibole to crystallize, which can deplete Ta–Nb–Ti while enriching SiO_2, alkalis and other incompatible elements (e.g. Th, U, LREE) in the residual or ascending melt (Tiepolo *et al.*, 2000, 2001). Thus, the 'open-system' precipitation of amphibole will fractionate trace elements and generate low (Nb,Ta)/(Th,U,LREE) ratios in the residual fluids. The flat HREE patterns for all the western Yunnan mafic potassic and ultrapotassic rocks are consistent with amphibole (vs garnet) fractionation or amphibole as a residual phase (Figs 5a and 18). The effects of amphibole fractionation on the Nb/Ta and Zr/Hf ratio depends on the amphibole compositions (Tiepolo *et al.*, 2001). Low-Mg amphibole has $D(\mathrm{Nb})/D(\mathrm{Ta}) > 1$ and $D(\mathrm{Zr})/D(\mathrm{Hf}) < 1$ (Tiepolo *et al.*, 2001); fractionation of such amphibole would lower the Nb/Ta ratio in the remaining melt, but increase the Zr/Hf ratio, which is not observed in the western Yunnan mafic potassic and ultrapotassic rocks (Fig. 19b and c). In contrast, fractionation of high-Mg amphibole causes similar shifts in Zr/Hf and Nb/Ta. Thus the positive correlation between Zr/Hf and Nb/Ta in the western Yunnan mafic potassic and ultrapotassic rocks (Fig. 19d) suggests the fractionation of

Downloaded from https://academic.oup.com/petrology/article/51/8/1617/1456692 by U.S. Department of Justice user on 17 August 2022

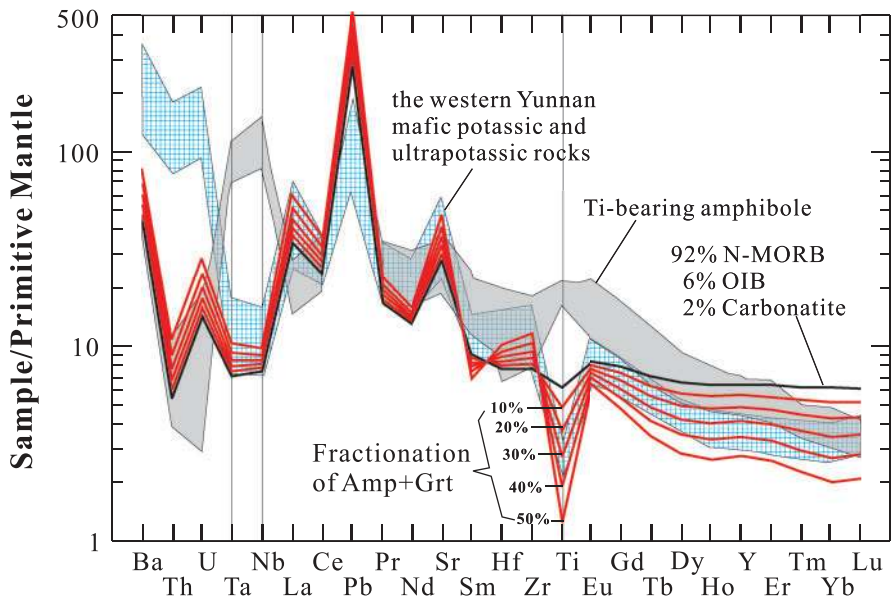

Fig. 18. Primitive mantle (PM)-normalized multi-element patterns of the western Yunnan mafic ultrapotassic volcanic rocks, Ti-rich amphibole and the assumed melts (92% N-MORB + 6% OIB + 2% carbonatite) and their derivatives by 10–50% Rayleigh fractionation of 80% amphibole + 20% garnet. Ti-rich amphibole is from Coltorti *et al.* (2004). Partition coefficients of amphiboles used were summarized by Niu & O'Hara (2009), except for Nb, Ta, Zr, Hf and Ti (0·708, 0·483, 0·419, 0·679 and 4·06, respectively) for bulk-rock composition of $SiO_2 = 50–52\%$ (Tiepolo *et al.*, 2000, 2001); partition coefficients of garnet are from Johnson (1994, 1998). PM normalization values are from Sun & McDonough (1989). Ba and Th are underestimated in the model calculation because they mainly occur in accessory minerals (e.g. monazite, barites and bastnaesite) associated with the Sichuan carbonatites (Xu *et al.*, 2008).

high-Mg amphibole. In addition, most Ti-bearing amphiboles have higher partition coefficient ratios, i.e. $D(Nb)/D(Zr)$ (Tiepolo *et al.*, 2000, 2001), and amphibole fractionation or its presence as a residual phase can explain low Nb/Zr in the melts as observed in the western Yunnan mafic potassic and ultrapotassic rocks (Fig. 5b). Although the high-pressure crystal-fractionation of 'amphibole + garnet' is capable of decreasing Ta–Nb–Ti in the melt, the unrealistic amounts (20–50 vol. %) of 'amphibole + garnet' separation would deplete FeO and MgO in the melt. Thus we suggest that Ti-bearing amphibole fractionation or its presence as residual phase may play an important role in causing Ti (as well as Nb and Ta) depletion in the western Yunnan mafic potassic and ultrapotassic rocks; however, this process must be superimposed on the effects of inherited source compositions (i.e. depletion of Ta–Nb–Ti relative to Ba, Rb, Cs, Th, U, etc.) as a result of mantle metasomatism.

Evolution of mantle lithosphere beneath western Yangtze craton

Parts of the mantle lithosphere could be highly depleted in terms of a basaltic component as widely recognized by the decoupled major–trace element characteristics of the subcontinental lithosphere (e.g. Menzies, 1983; Menzies & Hawkesworth, 1987; O'Reilly & Griffin, 1988; McDonough, 1990). The western Yunnan potassic and ultrapotassic rocks are probably derived from such a highly depleted refractory source modified by subsequent metasomatic enrichment. This interpretation is consistent with the mineralogy and geochemistry of the western Yunnan potassic and ultrapotassic rocks. For example, the compositionally depleted spinel (e.g. high Cr-number, 0·77–0·94 and low Al_2O_3, <10%) and the low Al_2O_3 and FeO_{Tot} in these samples is consistent with derivation from a major element-depleted harzburgitic source; however, the highly enriched incompatible element characteristics are consistent with and actually require metasomatism by an enriched melt. In addition to subduction-related mantle metasomatism, the mantle lithosphere can also become extremely enriched locally, by migrating melts from the seismic low-velocity zone (LVZ) (Niu *et al.*, 2002; Niu & O'Hara, 2003; Niu, 2008). The LVZ might in fact be the most dynamic region in the upper mantle, causing metasomatism in the growing superjacent lithosphere (Niu, 2008; Niu & O'Hara, 2008, 2009), because the small melt fraction in the LVZ would be enriched in volatiles and incompatible elements (Niu *et al.*, 2002; Niu & O'Hara, 2003). As the melt is buoyant it tends to concentrate towards the top of the LVZ, where it can metasomatize the thickening lithosphere from its base (Niu, 2008). Such melts may, in fact, exist throughout the LVZ (Lambert & Wyllie, 1968, 1970; Green & Liebermann, 1976; Niu & O'Hara, 2003; Niu, 2008), causing the observed low seismic velocity (Green & Liebermann, 1976).

Downloaded from https://academic.oup.com/petrology/article/51/8/1617/1456692 by U.S. Department of Justice user on 17 August 2022

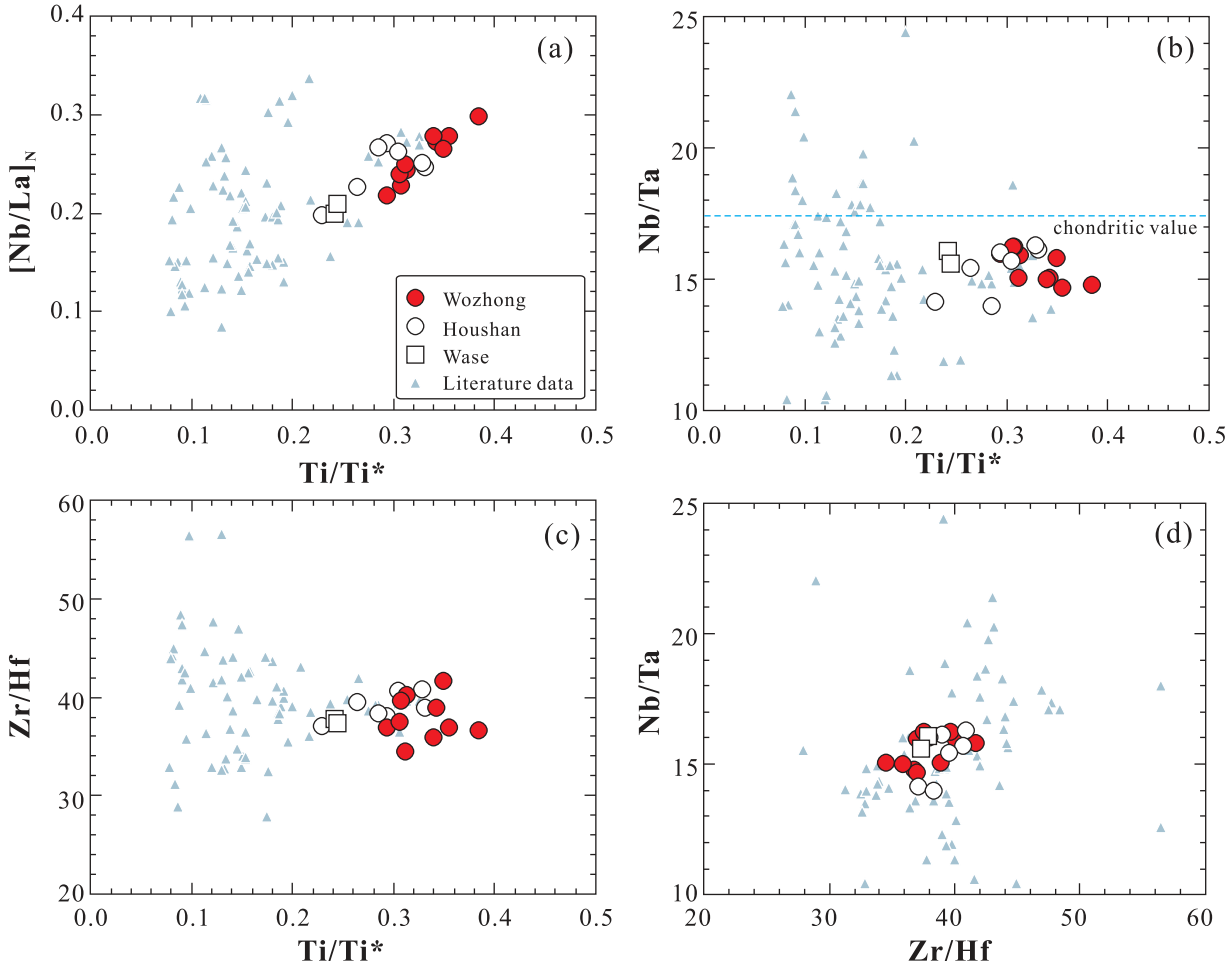

Fig. 19. (a–c) Variation of $[Nb/La]_N$, Nb/Ta and Zr/Hf vs Ti/Ti*; (d) Nb/Ta vs Zr/Hf. Data sources are as Fig. 4. Chondrite value of Nb/Ta = 17·4 is taken from Sun & McDonough (1989).

According to the biostratigraphic and sedimentological studies, the western Yangtze craton was the centre of a domal uplift associated with the Late Permian Emeishan mantle plume (Fig. 1a; He *et al.*, 2003). The mantle beneath the centre of the domal structure above the plume axis would have undergone the largest extent of melting (Xu *et al.*, 2004, 2007) and thus became highly depleted (Fig. 20a). The low-Ti lavas of the Emeishan LIP are consistent with a melting depth of 60–140 km, whereas the high-Ti lavas are interpreted to be generated at 75–100 km (Xu *et al.*, 2001*b*). It follows that the western Yunnan lithosphere must have been rather thin immediately after the Emeishan LIP volcanism (Fig. 20a). Such thin lithosphere will thicken with time because of conductive heat loss to the surface in a manner similar to that of oceanic lithosphere growth by accreting the subjacent volatile (e.g. H_2O, CO_2, etc.) and incompatible element enriched LVZ material at its base (Fig. 20b; Niu, 2008; Niu & O'Hara, 2008, 2009), a process that leads to the formation of metasomatized veins within the mantle lithosphere.

The subduction of the Palaeo-Tethys ocean (Lancanjiang) beneath South China during Devonian and early Carboniferous times provided the initial metasomatic fluids for the enrichment of the mantle beneath the western Yangtze craton and its peripheral regions. The Jinshajiang–Ailaoshan ocean between the Changdu–Simao Block and South China (Fig. 1a) developed from a back-arc extensional basin as a result of subduction of the Lancangjiang–Changning–Menglian seafloor during Early Carboniferous to Permian times (Wang *et al.*, 2000). Because the Jinshajiang–Ailaoshan ocean subducted westward beneath the eastern margin of the Changdu–Simao Block from Late Permian to middle Triassic times (Mo *et al.*, 1993; Wang *et al.*, 2000; Sun & Jian, 2004), the highly depleted mantle beneath the western Yangtze craton after its large degree melting (Xu *et al.*, 2004, 2007) (Fig. 20a) would not have been directly refertilized by the subduction of Paleo-Tethyan seafloor. However, the mantle away from the centre of the Emeishan plume could have survived to some extent the purge of the Emeishan plume and have

Downloaded from https://academic.oup.com/petrology/article/51/8/1617/1456692 by U.S. Department of Justice user on 17 August 2022

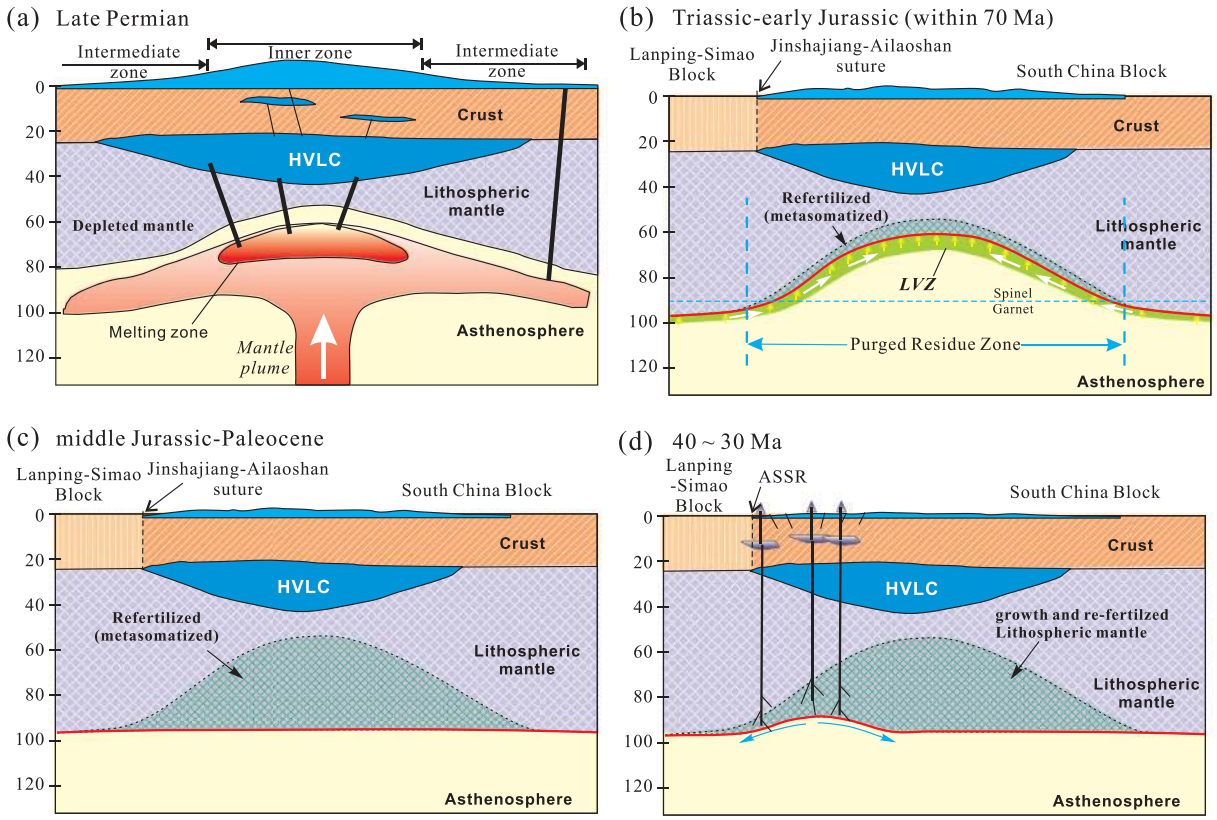

Fig. 20. Schematic illustration of the suggested model for the petrogenesis and evolution of the western Yunnan post-collisional potassic and ultrapotassic rocks. The domal structure of the Emeishan mantle plume is modified from He *et al.* (2003) and Xu *et al.* (2004, 2007). HVLC, high-velocity lower crust; LVZ, seismic low-velocity zone; ASSR, Ailao Shan–Red River fault.

retained some metasomatic imprint associated with Proterozoic subduction and the other Paleozoic Paleo-Tethyan seafloor subduction processes (Guo *et al.*, 2005). These metasomatic materials could have remelted and the resultant enriched melts concentrated towards the LVZ beneath the thin lithosphere at the centre of the domal structure above the plume (Fig. 20b). This process would also carry the trace of metasomatic fluids with some 'crust-like' features (i.e. Ta–Nb–Ti depletion relative to Ba, Rb, Cs, Th, U and REE), resembling subduction components. The lithosphere beneath the western Yangtze craton could reach its full thickness of ~95 km with time through basal accretion of LVZ material for ~70 Myr (from Triassic to early Jurassic times; Fig. 20b) similar to models of oceanic lithosphere formation (Niu, 2008; Niu & O'Hara, 2009). From middle Jurassic to Paleocene times the Neo-Tethys Ocean, represented by the Nujiang suture zone, was far away from the western Yangtze craton (Fig. 1a); thus 'normal' subduction of Neo-Tethys seafloor could not directly provide slab-fluid to metasomatize the mantle beneath the western Yangtze craton. Therefore the lithosphere beneath the western Yangtze craton with its full thickness was probably in a state of secular isolation during the period ~180–40 Ma (Fig. 20c). The very high Th, U, Rb, Sr and LREE in an isolated reservoir would facilitate in-growth of an enriched Sr–Nd–Pb isotopic signature.

Metasomatic veins in growing and thickened mantle lithosphere could not melt without perturbation of the geotherm (e.g. dT/dP change with respect to the solidus of the metasomatized mantle lithosphere); this did not occur until India–Asia collision induced intraplate extension along the western Yangtze craton close to the AilaoShan–Red River shear zone (Chung *et al.*, 1997, 2005, 2008) (Fig. 20c and d). Such lithospheric extension can trigger localized decompression melting of metasomatic lithologies that are close to their volatile-present solidi. The Ailao Shan–Red River fault zone also provides the conduit for the ascent and eruption of the potassic and ultrapotassic magmas (Fig. 20d).

CONCLUSIONS

The western Yunnan Paleogene mafic potassic and ultrapotassic rocks contain abundant olivine and clinopyroxene phenocrysts and xenocrysts. Their compositional variation

Downloaded from https://academic.oup.com/petrology/article/51/8/1617/1456692 by U.S. Department of Justice user on 17 August 2022

indicates complex magma chamber processes, including extensive fractional crystallization, crystal accumulation, and multiple replenishment by mafic magmas combined with limited crustal contamination.

Melting of metasomatically enriched mantle lithosphere, olivine (and spinel) dominated fractional crystallization and olivine accumulation together can explain the petrogenesis of the western Yunnan mafic potassic and ultrapotassic rocks. All these processes plus the potential effect of Ti-rich amphibole crystallization during melt ascent through the lithosphere can well explain the geochemistry of the western Yunnan potassic and ultrapotassic rocks.

High-Mg olivine (Fo >90 and up to 93) in the western Yunnan mafic potassic and ultrapotassic rocks crystallized from ultrapotassic magmas with high Mg-number. The high Mg-number is probably due to the high fO_2 and thus low Fe^{2+}/Fe^{3+} of the melts, inherited from high fO_2 in the metasomatized harzburgitic lithospheric mantle source.

Crustal contamination is inevitable in intra-continental plate tectonic settings but it is ineffective in explaining the Ta–Nb–Ti-depleted geochemical signatures of these rocks. Ancient subduction beneath the region is possible, but is not required to explain the petrogenesis of the ultrapotassic rocks. Instead, tectonically induced localized decompression melting of incompatible element and volatile-enriched metasomatized mantle lithosphere best explain the observations.

The metasomatism may be more recent than the Emeishan LIP magmatism in the late Permian, and may be dominated by melt from the seismic low-velocity zone beneath the lithosphere.

ACKNOWLEDGEMENTS

We acknowledge the constructive comments of M. Wilson, S. Conticelli, D. Prelević, P. Leat, J. C. M. De Hoog and S. L. Chung, which helped considerably in improving the manuscript. We also thank C. Y. Lee, D. R. Wen, X. R. Liang, H. N. Qiu and Y. S. Liu for analytical assistance. The research was supported by knowledge Innovation Project of the Chinese Academy of Sciences (KZCX2-YW-Q08-3-6, KZCX2-YW-QN106), the National Natural Science Foundation of China (NSFC projects 40721063, 40773015) and the CAS/SAFEA International Partnership Program for Creative Research Teams. This is contibution No. IS-1200 from GIGCAS.

REFERENCES

Arai, S. (1994). Characterization of spinel peridotites by olivine–spinel compositional relationships: review and interpretation. *Chemical Geology* **113**, 191–204.

Arnaud, N. O., Vidal, P., Tapponnier, P., Matte, P. & Deng, W. M. (1992). The high K_2O volcanism of northwestern Tibet: Geochemistry and tectonic implications. *Earth and Planetary Science Letters* **111**, 351–367.

Ballhaus, C., Berry, R. F. & Green, D. H. (1990). Oxygen fugacity controls in the Earth's upper mantle. *Nature* **348**, 437–440.

Barton, M. & Van Bergen, M. J. (1981). Green clinopyroxenes and associated phases in a potassium-rich lava from the Leucite Hill, Wyoming. *Contributions to Mineralogy and Petrology* **77**, 101–114.

Bernard-Griffiths, J., Fourcade, S. & Dupuy, C. (1991). Isotopic study (Sr, Nd, O and C) of lamprophyres and associated dykes from Tamazert (Moroco): crustal contamination processes and source characteristics. *Earth and Planetary Science Letters* **103**, 190–199.

BGMR. (1975). Geological map of Yunnan Province. *Sheet sheets G-47-XXIII (Dali) and G-47-XVII (Heqing), Scale 1:200000.* Kuming: Bureau of Geology and Mineral Resources.

Botcharnikov, R. E., Koepke, J., Holtz, F., McCammon, C. & Wilke, M. (2005). The effect of water activity on the oxidation and structural state of Fe in a ferro-basaltic melt. *Geochimica et Cosmochimica Acta* **69**, 5071–5085.

Cadoux, A. & Pinti, D. L. (2009). Hybrid character and pre-eruptive events of Mt Amiata volcano (Italy) inferred from geochronological, petro-geochemical and isotopic data. *Journal of Volcanology and Geothermal Research* **179**, 169–190.

Cellai, D., Conticelli, S. & Menchetti, S. (1994). Crystal-chemistry of clinopyroxenes in Italian lamproites and kamafugites: Implications on their genesis. *Contributions to Mineralogy and Petrology* **116**, 301–315.

Chung, S. L., Lee, T. Y., Lo, C. H., Wang, P. L., Chen, C. Y., Nguyen, T. Y., Tran, T. H. & Wu, G. Y. (1997). Intraplate extension prior to continental extrusion along the Ailao Shan–Red River shear zone. *Geology* **25**, 311–314.

Chung, S. L., Lo, C. H., Lee, T. Y., Zhang, Y., Xie, Y., Li, X. H., Wang, K. L. & Wang, P. L. (1998). Diachronous uplift of the Tibetan Plateau starting 40 Myr ago. *Nature* **394**, 769–773.

Chung, S. L., Chu, M. F., Zhang, Y. Q., Xie, Y. W., Lo, C. H., Lee, T. Y., Lan, C. Y., Li, X. H., Zhang, Q. & Wang, Y. Z. (2005). Tibetan tectonic evolution inferred from spatial and temporal variations in post-collisional magmatism. *Earth-Science Reviews* **68**, 173–196.

Çoban, H. & Flower, M. F. J. (2006). Mineral phase compositions in silica-undersaturated 'leucite' lamproites from the Bucak area, Isparta, SW Turkey. *Lithos* **89**, 275–299.

Coltorti, M., Beccaluva, L., Bonadiman, C., Faccini, B., Ntaflos, T. & Siena, F. (2004). Amphibole genesis via metasomatic reaction with clinopyroxene in mantle xenoliths from Victoria Land, Antarctica. *Lithos* **75**, 115–139.

Coltorti, M., Bonadiman, C., Faccini, B., Grégoire, M., O'Reilly, S. Y. & Powell, W. (2007). Amphiboles from suprasubduction and intraplate lithospheric mantle. *Lithos* **99**, 68–84.

Conticelli, S. (1998). The effect of crustal contamination on ultrapotassic magmas with lamproitic affinity: mineralogical, geochemical and isotope data from the Torre Alfina lavas and xenoliths, Central Italy. *Chemical Geology* **149**, 51–81.

Conticelli, S. & Peccerillo, A. (1992). Petrology and geochemistry of potassic and ultrapotassic volcanism in central Italy: petrogenesis and inferences on the evolution of the mantle sources. *Lithos* **28**, 221–240.

Conticelli, S., Francalanci, L., Manetti, P., Cioni, R. & Sbrana, A. (1997). Petrology and geochemistry of the ultrapotassic rocks from the Sabatini Volcanic District, Central Italy: the role of evolutionary processes in the genesis of variably enriched alkaline magmas. *Journal of Volcanology and Geothermal Research* **75**, 107–136.

Conticelli, S., Guarnieri, L., Farinelli, A., Mattei, M., Avanzinelli, R., Bianchini, G., Boari, E., Tommasini, S., Tiepolo, M., Prelević, D. & Venturelli, G. (2009). Trace elements and Sr–Nd–Pb isotopes of K-rich, shoshonitic, and calc-alkaline magmatism of the western Mediterranean region: genesis of ultrapotassic to calc-alkaline

Downloaded from https://academic.oup.com/petrology/article/51/8/1617/1456692 by U.S. Department of Justice user on 17 August 2022

magmatic associations in a post-collisional geodynamic setting. *Lithos* **107**, 68–92.

Crawford, A. J. (1989). *Boninites*. London: Unwin–Hyman, 465 p.

Cundari, A. & Salviulo, G. (1989). Ti solubility in diopsidic pyroxene from a suite of New South Wales leucitites (Australia). *Lithos* **22**, 191–198.

Deng, W. M. & Zhong, D. L. (1997). Crust–mantle transition zone and geological signification in the structure evolution of lithosphere. *Chinese Science Bulletin* **42**, 2474–2482 (in Chinese).

Deng, W. M., Huang, X. & Zhong, D. L. (1998*a*). Alkali-rich porphyry and its relation with intraplate deformation of north part of Jinsha River belt in western Yunnan, China. *Science in China (D)* **41**, 297–305.

Deng, W. M., Huang, X. & Zhong, D. L. (1998*b*). Petrological characteristics and genesis of Cenozoic alkali-rich porphyry in west Yunnan, China. *Scientia Geologica Sinica* **33**, 412–425 (in Chinese with English abstract).

DePaolo, D. J. (1981). Trace element and isotopic effects of combined wallrock assimilation and fractional crystallization. *Earth and Planetary Science Letters* **53**, 189–202.

Dick, H. J. B. & Bullen, T. (1984). Chromian spinel as a petrogenetic indicator in abyssal and alpine-type peridotites and spatially associated lavas. *Contributions to Mineralogy and Petrology* **86**, 54–76.

Ding, L., Kapp, P., Zhong, D. L. & Deng, W. M. (2003). Cenozoic volcanism in Tibet: evidence for a transition from oceanic to continental subduction. *Journal of Petrology* **44**, 1833–1865.

Dobosi, G. (1989). Clinopyroxene zoning patterns in the young alkali basalts of Hungary and their petrogenetic significance. *Contributions to Mineralogy and Petrology* **101**, 112–121.

Dobosi, G. & Fodor, R. V. (1992). Magma fractionation, replenishment, and mixing as inferred from green-core clinopyroxenes in Pliocene basanite, southern Slovakia. *Lithos* **28**, 133–150.

Donnelly, K. E., Goldstein, S. L., Langmuir, C. H. & Spiegelman, M. (2004). Origin of enriched ocean ridge basalts and implications for mantle dynamics. *Earth and Planetary Science Letters* **226**, 347–366.

Droop, G. T. R. (1987). A general equation for estimating Fe^{3+} concentrations in ferromagnesian silicates and oxides from microprobe analyses, using stoichiometric criteria. *Mineralogical Magazine* **51**, 431–435.

Duda, A. & Schmincke, H. U. (1985). Polybaric differentiation of alkali basaltic magmas: evidence from green-core clinopyroxenes (Eifel, FRG). *Contributions to Mineralogy and Petrology* **91**, 340–353.

Fang, N. (1993). View of the closure of the Palaeo-Tethys: evidence from post Permian pelagic sedimentary records in western Yunnan. In: Wang, H. Z. (ed.) *Accretion of the Asia*. Beijing: Seismological Publishing House, pp. 57–60.

Fedele, L., Zanetti, A., Morra, V., Lustrino, M., Melluso, L. & Vannucci, R. (2009). Clinopyroxene/liquid trace element partitioning in natural trachyte–trachyphonolite systems: insights from Campi Flegrei (southern Italy). *Contributions to Mineralogy and Petrology* **158**, 337–356.

Feldstein, S. N. & Lange, R. A. (1999). Pliocene potassic magmas from the Kings River region, Sierra Nevada, California: evidence for melting of a subduction-modified mantle. *Journal of Petrology* **40**, 1301–1320.

Foley, S. F., Venturelli, G., Green, D. H. & Toscani, L. (1987). The ultrapotassic rocks: characteristics, classification, and constraints for petrogenetic models. *Earth-Science Reviews* **24**, 81–134.

Francalanci, L., Davies, G. R., Lustenhouwer, W., Tommasini, S., Mason, P. R. D. & Conticelli, S. (2005). Intra-grain Sr isotope evidence for crystal recycling and multiple magma reservoirs in the recent activity of Stromboli volcano, southern Italy. *Journal of Petrology* **46**, 1997–2021.

Gallagher, K. & Hawkesworth, C. J. (1992). Dehydration melting and the generation of continental flood basalts. *Nature* **358**, 57–59.

Green, D. H. & Liebermann, R. C. (1976). Phase equilibria and elastic properties of a Pyrolite model for the oceanic upper mantle. *Tectonophysics* **32**, 61–92.

Green, D. H., Falloon, T. J., Eggins, S. M. & Yaxley, G. M. (2001). Primary magmas and mantle temperatures. *European Journal of Mineralogy* **13**, 437–451.

Guo, Z. F., Hertogen, J., Liu, J., Pasteels, P., Boven, A., Punzalan, L., He, H., Luo, X. & Zhang, W. (2005). Potassic magmatism in Western Sichuan and Yunnan provinces, SE Tibet, China: petrological and geochemical constraints on petrogenesis. *Journal of Petrology* **46**, 33–78.

Guo, Z. F., Wilson, M., Liu, J. Q. & Mao, Q. (2006). Post-collisional, potassic and ultrapotassic magmatism of the northern Tibetan plateau: constraints on characteristics of the mantle source, geodynamic setting and uplift mechanisms. *Journal of Petrology* **47**, 1177–1220.

Gurenko, A. A., Hansteen, T. H. & Schmincke, H.-U. (1996). Evolution of parental magmas of Miocene shield basalts of Gran Canaria (Canary Islands): constraints from crystal, melt and fluid inclusions in minerals. *Contributions to Mineralogy and Petrology* **124**, 422–435.

Guzmics, T., Zajacz, Z., Kodolányi, J., Halter, W. & Szabó, C. (2008). LA-ICP-MS study of apatite- and K feldspar-hosted primary carbonatite melt inclusions in clinopyroxenite xenoliths from lamprophyres, Hungary: Implications for significance of carbonatite melts in the Earth's mantle. *Geochimica et Cosmochimica Acta* **72**, 1864–1886.

Haase, K. M., Hartmann, M. & Wallrabe-Adams, H.-J. (1996). The geochemistry of ashes from Vesterisbanken Seamount, Greenland Basin: implications for the evolution of an alkaline volcano. *Journal of Volcanology and Geothermal Research* **70**, 1–19.

Hart, S. R. (1984). A large-scale isotope anomaly in the Southern Hemisphere mantle. *Nature* **309**, 753–757.

Hawkesworth, C. J., Gallagher, K., Hergt, J. M. & McDermott, F. (1993). Mantle and slab contributions in arc magmas. *Annual Review of Earth and Planetary Sciences* **21**, 175–204.

He, B., Xu, Y. G., Chung, S. L., Xiao, L. & Wang, Y. (2003). Sedimentary evidence for a rapid crustal doming prior to the eruption of the Emeishan flood basalts. *Earth and Planetary Science Letters* **213**, 389–403.

Holloway, J. R. (2004). Redox reactions in seafloor basalts: possible insights into silicic hydrothermal systems. *Chemical Geology* **210**, 225–230.

Hou, Z. Q., Tian, S. H., Yuan, Z. X., Xie, Y. L., Yin, S. P., Yi, L. S., Fei, H. C. & Yan, Z. M. (2006). The Himalayan collision zone carbonatites in western Sichuan, SW China: Petrogenesis, mantle source and tectonic implication. *Earth and Planetary Science Letters* **244**, 234–250.

Ionov, D. A. & Hofmann, A. W. (1995). Nb–Ta-rich mantle amphiboles and micas: implications for subduction-related metasomatic trace element fractionations. *Earth and Planetary Science Letters* **131**, 341–356.

Ionov, D. A., Dupuy, C., O'Reilly, S. Y., Kopylova, M. G. & Genshaft, Y. S. (1993). Carbonated peridotite xenoliths from Spitsbergen—implications for trace-element signature of mantle carbonate metasomatism. *Earth and Planetary Science Letters* **119**, 283–297.

Ionov, D. A., Bodinier, J.-L., Mukasa, S. B. & Zanetti, A. (2002). Mechanisms and sources of mantle metasomatism: major and trace element compositions of peridotite xenoliths from

Downloaded from https://academic.oup.com/petrology/article/51/8/1617/1456692 by U.S. Department of Justice user on 17 August 2022

Spitsbergen in the context of numerical modeling. *Journal of Petrology* **43**, 2219–2259.

Ishimaru, S. & Arai, S. (2008). Highly silicic glasses in peridotite xenoliths from Avacha volcano, Kamchatka arc; implications for melting and metasomatism within the sub-arc mantle. *Lithos* **107**, 93–206.

Jaques, A. L., Lewis, J. D., Gregory, G. P., Ferguson, J., Smith, C. B., Chappell, B. W. & McCulloch, M. T. (1984). The diamond-bearing ultrapotassic (lamproitic) rocks from the west Kimberley region, Western Australia. In: Kornprobst, J. (ed.) *Proceedings of the Third International Kimberlite Conference*. New York: Elsevier, pp. 225–254.

Johnson, K. T. M. (1994). Experimental cpx/and garnet/melt partitioning of REE and other trace elements at high pressures; petrogenetic implications. *Mineralogical Magazine* **58**, 454–455.

Johnson, K. T. M. (1998). Experimental determination of partition coefficients for rare earth and high-field-strength elements between clinopyroxene, garnet, and basaltic melt at high pressures. *Contributions to Mineralogy and Petrology* **133**, 60–68.

Kamenetsky, V. S., Crawford, A. J. & Meffre, S. (2001). Factors controlling chemistry of magmatic spinel: an empirical study of associated olivine, Cr-spinel and melt inclusions from primitive rocks. *Journal of Petrology* **42**, 655–671.

Klemme, S., Prowatke, S., Hametner, K. & Gunther, D. (2005). Partitioning of trace elements between rutile and silicate melts: implications for subduction zones. *Geochimica et Cosmochimica Acta* **69**, 2361–2371.

Klemme, S., Gunther, D., Hametner, K., Prowatke, S. & Zack, T. (2006). The partitioning of trace elements between ilmenite, ulvöspinel, armalcolite and silicate melts with implications for the early differentiation of the Moon. *Chemical Geology* **234**, 251–263.

Koppers, A. A. P. (2002). ArArCALC—software for Ar-40/Ar-39 age calculations. *Computers and Geosciences* **28**, 605–619.

Krishnamurthy, P., Gopalan, K. & Macdougall, J. D. (2000). Olivine compositions in picrite basalts and the Deccan volcanic cycle. *Journal of Petrology* **41**, 1057–1069.

Lambert, I. B. & Wyllie, P. J. (1968). Stability of hornblende and a model for the low velocity zone. *Nature* **219**, 1240–1241.

Lambert, I. B. & Wyllie, P. J. (1970). Low-velocity zone of the Earth's mantle—incipient melting caused by water. *Science* **169**, 764–766.

Larsen, L. M. & Pedersen, A. K. (2000). Processes in high-Mg, high-*T* magmas: evidence from olivine, chromite and glass in Palaeogene picrites from West Greenland. *Journal of Petrology* **41**, 1071–1098.

Lee, C.-T. A., Leeman, W. P., Canil, D. & Li, Z.-X. (2005). Similar V/Sc systematics in MORB and arc basalts: implications for the oxygen fugacities of their mantle source regions. *Journal of Petrology* **46**, 2313–2336.

Leloup, H., Lacassin, R., Tapponnier, P., Scharer, U., Zhong, D. L., Liu, X., Zhang, L. S., Ji, S. & Phan, T. T. (1995). The Ailao Shan–Red River shear zone (Yunnan, China), Tertiary transform boundary of Indochina. *Tectonophysics* **251**, 3–84.

Le Maitre, R. W., Bateman, P., Dudek, A., Keller, J., Lameyre, J., Le Bas, M. J., Sabine, P. A., Schmid, R., Sorensen, H., Streckeisen, A., Woolley, A. R. & Zanettin, B. (1989). *A Classification of Igneous Rocks and Glossary of Terms*. Oxford: Blackwell, 193 p.

Li, X. H., Zhou, H., Chung, S. L., Lo, C. H., Wei, G., Liu, Y. & Lee, C. Y. (2002). Geochemical and Sr–Nd isotopic characteristics of late Paleogene ultrapotassic magmatism in southeastern Tibet. *International Geology Review* **44**, 559–574.

Li, X. H., Liu, D. Y., Sun, M., Li, W. X., Liang, X. R. & Liu, Y. (2004). Precise Sm–Nd and U–Pb isotopic dating of the supergiant Shizhuyuan polymetallic deposit and its host granite, Southeast China. *Geological Magazine* **141**, 225–231.

Liang, H. Y., Campbell, I. H., Allen, C. M., Sun, W. D., Yu, H. X., Xie, Y. W. & Zhang, Y. Q. (2007). The age of the potassic alkaline igneous rocks along the Ailao Shan–Red River shear zone: implications for the onset age of left-lateral shearing. *Journal of Geology* **115**, 231–242.

Liu, J., Liu, F., He, J., Chen, H. & You, Q. (2001). Study of seismic tomography in Panxi paleorift area of southwestern China—structural features of crust and mantle and their evolution. *Science in China (D)* **44**, 277–288.

Liu, Y. S., Hu, Z. C., Gao, S., Günther, D., Xu, J., Gao, C. G. & Chen, H. H. (2008). *In situ* analysis of major and trace elements of anhydrous minerals by LA-ICP-MS without applying an internal standard. *Chemical Geology* **257**, 34–43.

McCammon, C. A., Griffin, W. L., Hee, S. H. & O'Neill, H. S. C. (2001). Oxidation during metasomatism in ultramafic xenoliths from the Wesselton kimberlite, South Africa: implications for the survival of diamond. *Contributions to Mineralogy and Petrology* **141**, 287–296.

McDonough, W. F. (1990). Constraints on the composition of the continental lithospheric mantle. *Earth and Planetary Science Letters* **101**, 1–18.

McGuire, A. V., Dyar, M. D. & Nielson, J. E. (1991). Metasomatic oxidation of upper mantle peridotite. *Contributions to Mineralogy and Petrology* **109**, 252–264.

McKenzie, D. P. (1989). Some remarks on the movement of small melt fractions in the mantle. *Earth and Planetary Science Letters* **95**, 53–72.

Melluso, L., Lustrino, M., Ruberti, E., Brotzu, P., Barros Gomes, C. E., Morbidelli, L., Morra, V., Svisero, D. P. & D'Amelio, F. (2008). Major- and trace-element composition of olivine, perovskite, clinopyroxene, Cr–Fe–Ti oxides, phlogopite and host kamafugites and kimberlites, Alto Paranaíba, Brazil. *Canadian Mineralogist* **46**, 19–40.

Menzies, M. A. (1983). Mantle ultramafic xenoliths in alkaline magmas: evidence for mantle heterogeneity modified by magmatic activity. In: Hawkesworth, C. J. & Norry, M. J. (eds) *Continental Basalts and Mantle Xenoliths*. Nantwich: Shiva, pp. 92–110.

Menzies, M. A. & Hawkesworth, C. J. (1987). *Mantle Metasomatism*. Academic Press Geology Series. London: Academic Press, 472 pp p.

Miller, C., Schuster, R., Klotzli, U., Frank, W. & Purtscheller, F. (1999). Post-collisional potassic and ultrapotassic magmatism in SW Tibet: Geochemical and Sr–Nd–Pb–O isotopic constraints for mantle source characteristics and petrogenesis. *Journal of Petrology* **40**, 1399–1424.

Mitchell, R. H. (1995). *Kimberlites, Orangeites, and Related Rocks*. New York: Plenum, 410 pp p.

Mitchell, R. H. & Bergman, S. C. (1991). *Petrology of Lamproites*. NewYork: Plenum, 447 p.

Mo, X. X., Lu, F. X., Shen, S. Y., Zhu, Q. W., Hou, Z. Q., Yang, K. H., Deng, J. F., Liu, X. P. & He, C. X. (1993). *Sanjiang Tethyan volcanism and related mineralization*. Beijing: Geological Publishing House, 267 pp p (in Chinese with English abstract).

Mo, X., Zhao, Z., Deng, J., Flower, M., Yu, X., Luo, Z., Li, Y., Zhou, S., Dong, S., Zhu, D. & Wang, L. (2006). Petrology and geochemistry of postcollisional volcanic rocks from the Tibetan plateau: Implications for lithosphere heterogeneity and collision-induced asthenospheric mantle flow. In: Dilek, Y. & Pavlides, S. (eds) *Postcollisional Tectonics and Magmatism in the Mediterranean Region and Asia. Geological Society of America, Special Papers* **409**, 507–530.

Nelson, D. R., McCulloch, M. T. & Sun, S. S. (1986). The origins of ultrapotassic rocks as inferred from Sr, Nd and Pb isotopes. *Geochimica et Cosmochimica Acta* **50**, 231–245.

Downloaded from https://academic.oup.com/petrology/article/51/8/1617/1456692 by U.S. Department of Justice user on 17 August 2022

Niida, K. & Green, D. H. (1999). Stability and chemical composition of pargasitic amphibole in MORB pyrolite under upper mantle conditions. *Contributions to Mineralogy and Petrology* **135**, 18–40.

Niu, Y. L. (2008). The origin of alkaline lavas. *Science* **320**, 883–884.

Niu, Y. L. & O'Hara, M. J. (2003). The origin of ocean island basalts (OIB): a new perspective from petrology, geochemistry and mineral physics considerations. *Journal of Geophysical Research* **108**, 2209, doi:10.1029/2002JB002048. ECV 5-1-19.

Niu, Y. L. & O'Hara, M. J. (2008). Global correlations of ocean ridge basalt chemistry with axial depth: a new perspective. *Journal of Petrology* **49**, 633–664.

Niu, Y. L. & O'Hara, M. J. (2009). MORB mantle hosts the missing Eu (Sr, Nb, Ta and Ti) in the continental crust: New perspectives on crust–mantle differentiation and chemical structure of oceanic upper mantle. *Lithos* **112**, 1–17.

Niu, Y. L., Regelous, M., Wendt, J. I., Batiza, R. & O'Hara, M. J. (2002). Geochemistry of near-EPR seamounts: importance of source vs process and the origin of enriched mantle component. *Earth and Planetary Science Letters* **199**, 327–345.

O'Hara, M. J. & Mathews, R. E. (1981). Geochemical evolution in an advancing, periodically replenished, periodically tapped, continuously fractionated magma chamber. *Journal of the Geological Society, London* **138**, 237–277.

O'Reilly, Y. S. & Griffin, W. L. (1988). Mantle metasomatism beneath western Victoria, Australia: I. Metasomatic processes in Cr-diopside lherzolites. *Geochimimica et Cosmochimica Acta* **52**, 433–447.

Peccerillo, A. (1985). Roman Comagmatic Province (Central Italy): Evidence for subduction related magma genesis. *Geology* **13**, 103–106.

Perini, G. & Conticelli, S. (2002). Crystallization conditions of leucite-bearing magmas and their implications on the magmatological evolution of ultrapotassic magmas: the Vico Volcano, Central Italy. *Mineralogy and Petrology* **74**, 253–276.

Prelević, D. & Foley, S. F. (2007). Accretion of arc–oceanic lithospheric mantle in the Mediterranean: Evidence from extremely high-Mg olivines and Cr-rich spinel inclusions in lamproites. *Earth and Planetary Science Letters* **256**, 120–135.

Qian, X. G. & Lu, B. X. (2000). The petrographic features and genesis of Cenozoic alkali volcanic rocks in the Three-River area, west Yunnan. *Yunnan Geology* **19**, 152–170 (in Chinese with English abstract).

Roeder, P. L. & Emslie, R. F. (1970). Olivine–liquid equilibrium. *Contributions to Mineralogy and Petrology* **29**, 275–289.

Rudnick, R. L. & Gao, S. (2003). The composition of the continental crust. In: Rudnick, R. L. (ed.) *The Crust, Treatise on Geochemistry, Vol.3*. Oxford: Elsevier, pp. 1–64.

Sato, H. (1977). Nickel content of basaltic magmas: identification of primary magmas and a measure of the degree of olivine fractionation. *Lithos* **10**, 113–120.

Sato, M. & Wright, T. L. (1996). Oxygen fugacities directly measured in magmatic gases. *Science* **153**, 1103–1105.

Schiano, P., Bourdon, B., Clocchiatti, R., Massare, D., Varela, M. E. & Bottinga, Y. (1998). Low degree partial melting trends recorded in upper mantle minerals. *Earth and Planetary Science Letters* **160**, 537–550.

Simkin, K. & Smith, J. V. (1978). Minor element distribution in olivine. *Journal of Geology* **78**, 304–325.

Stone, S. & Niu, Y. L. (2009). Origin of compositional trends in clinopyroxene of oceanic gabbros and gabbroic rocks: A case study using data from ODP Hole 735B. *Journal of Volcanology and Geothermal Research* **184**, 313–322.

Streck, M. J., Dungan, M. A., Bussy, F. & Malavassi, E. (2005). Mineral inventory of continuously erupting basaltic andesites at Arenal volcano, Costa Rica: implications for interpreting monotonous, crystal-rich, mafic arc stratigraphies. *Journal of Volcanology and Geothermal Research* **140**, 133–155.

Sun, S.-S. & McDonough, W. F. (1989). Chemical and isotopic systematics of oceanic basalts: implications for mantle composition and processes. In: Saunders, A. D. & Norry, M. J. (eds) *Magmatism in the Ocean Basins. Geological Society, London, Special Publications* **42**, 313–345.

Sun, X. M. & Jian, P. (2004). The Wilson cycle of the Jinshajiang Paleo-Tethys ocean, in western Yunnan and western Sichuan Provinces. *Geological Review* **50**, 333–350 (in Chinese with English abstract).

Tanaka, T., Togashi, S., Kamioka, H., Amakawa, H., Kagami, H., Hamamoto, T., Yuhara, M., Orihashi, Y., Yoneda, S., Shimizu, H., Kunimaru, T., Takahashi, K., Yanagi, T., Nakano, T., Fujimaki, H., Shinjo, R., Asahara, Y., Tanimizu, M. & Dragusanu, C. (2000). JNdi-1: a neodymium isotopic reference in consistency with LaJolla neodymium. *Chemical Geology* **168**, 279–281.

Tapponnier, P., Peltzer, G., Armijo, R., Le Dain, A. Y. & Cobbold, P. (1982). Propagating extrusion tectonic in Asia: New insights from simple experiments with plasticine. *Geology* **10**, 611–616.

Tatsumi, Y. (1986). Formation of the volcanic front in subduction zones. *Geophysical Research Letters* **13**, 717–720.

Taylor, S. R. & McLennan, S. M. (1985). *The Continental Crust: its Composition and Evolution*. Oxford: Blackwell Scientific, 312 p.

Thompson, R. N. & Gibson, S. A. (1994). Magmatic expressions of lithospheric thinning across continental rifts. *Tectonophysics* **233**, 41–68.

Thompson, R. N. & Gibson, S. A. (2000). Transient high temperatures in mantle plume heads inferred from magnesian olivines in Phanerozoic picrites. *Nature* **407**, 502–506.

Tiepolo, M., Vannucci, R., Oberti, R., Foley, S., Bottazzi, P. & Zanetti, A. (2000). Nb and Ta incorporation and fractionation in titanian pargasite and kaersutite: crystal chemical constraints and implications for natural systems. *Earth and Planetary Science Letters* **176**, 185–201.

Tiepolo, M., Bottazzi, P., Foley, S. F., Oberti, R., Vannucci, R. & Zanetti, A. (2001). Fractionation of Nb and Ta from Zr and Hf at mantle depths: the role of titanian pargasite and kaersutite. *Journal of Petrology* **42**, 221–232.

Turbeville, B. N. (1993). Petrology and petrogenesis of the Latera caldera, central Italy. *Journal of Petrology* **34**, 77–123.

Turner, S., Hawkesworth, C., Gallagher, K., Stewart, K., Peate, D. & Mantovani, M. (1996). Mantle plumes, flood basalts, and thermal models for melt generation beneath continents: assessment of a conductive heating model and application to the Paran. *Journal of Geophysical Research* **101**, 11503–11518.

Varekamp, J. C. & Kalamarides, R. I. (1989). Hybridization processes in leucite tephrite from Vulsini, Italy, and the evolution of the Italian potassic suite. *Journal of Geophysical Research* **94**, 4603–4618.

Wang, J. H., Yin, A., Harrison, T. M., Grove, M., Zhang, Y. Q. & Xie, G. H. (2001). A tectonic model for Cenozoic igneous activities in the eastern Indo-Asian collision zone. *Earth and Planetary Science Letters* **188**, 123–133.

Wang, X., Metcalfe, I., Jian, P., He, L. & Wang, C. (2000). The Jinshajiang–Ailaoshan Suture Zone, China: tectonostratigraphy, age and evolution. *Journal of Asian Earth Sciences* **18**, 675–690.

Wass, S. Y. (1979). Multiple origins of clinopyroxenes in alkali basaltic rocks. *Lithos* **12**, 115–132.

Wei, G. J., Liang, X. R., Li, X. H. & Liu, Y. (2002). Precise measurement of Sr isotopic compositions of liquid and solid base using (LP) MCICP-MS. *Geochimica* **31**, 295–305 (in Chinese with English abstract).

Wilson, M. (1989). *Igneous Petrogenesis*. London: Unwin Hyman, 466 p.

Downloaded from https://academic.oup.com/petrology/article/51/8/1617/1456692 by U.S. Department of Justice user on 17 August 2022

Xiong, X. L., Adam, J. & Green, T. H. (2005). Rutile stability and rutile/melt HFSE partitioning during partial melting of hydrous basalt: Implications for TTG genesis. *Chemical Geology* **218**, 339–359.

Xu, C., Campbell, I. H., Kynicky, J., Allen, C. M., Chen, Y. J., Huang, Z. L. & Qi, L. (2008). Comparison of the Daluxiang and Maoniuping carbonatitic REE deposts with Bayan Obo REE deposit, China. *Lithos* **106**, 12–24.

Xu, Y. G., Menzies, M. A., Thirlwall, M. F. & Xie, G. H. (2001*a*). Exotic lithosphere mantle beneath the western Yangtze craton: Petrogenetic links to Tibet using highly magnesian ultrapotassic rocks. *Geology* **29**, 863–866.

Xu, Y. G., Chung, S. L., Jahn, B. M. & Wu, G. Y. (2001*b*). Petrologic and geochemical constraints on the petrogenesis of Permian–Triassic Emeishan flood basalts in southwestern China. *Lithos* **58**, 145–168.

Xu, Y. G., Huang, X. L., Menzies, M. A. & Wang, R. C. (2003). Highly magnesian olivines and green-core clinopyroxenes in ultrapotassic lavas from western Yunnan, China: evidence for a complex hybrid origin. *European Journal of Mineralogy* **15**, 965–975.

Xu, Y. G., He, B., Chung, S. L., Menzies, M. A. & Frey, F. A. (2004). Geologic, geochemical, and geophysical consequences of plume involvement in the Emeishan flood-basalt province. *Geology* **32**, 917–920.

Xu, Y. G., He, B., Huang, X. L., Luo, Z. Y., Chung, S. L., Xiao, L., Zhu, D., Shao, H., Fan, W. M., Xu, J. F. & Wang, Y. J. (2007). Identification of mantle plumes in the Emeishan Large Igneous Province. *Episodes* **30**, 32–42.

Yaxley, G. M., Green, D. H. & Kamenetsky, V. (1998). Carbonatite metasomatism in the Southeastern Australian Lithosphere. *Journal of Petrology* **39**, 1917–1930.

Zeng, P. S., Mo, X. X. & Yu, X. H. (2002). Nd, Sr and Pb isotopic characteristics of the alkaline-rich porphyries in western Yunnan and its compression strike-slip setting. *Acta Petrologica et Mineralogica* **21**, 231–241 (in Chinese).

Zhang, Q., Zhou, D. & Chen, Y. (1996). A new type oceanic crust and its dynamic significance. *Chinese Science Bulletin* **41**, 25–27 (in Chinese).

Zhang, Y. Q. & Xie, Y. W. (1997). Chronology and Nd, Sr isotopic characteristics for the Ailaoshan–Jinshajiang alkali-rich intrusive rocks. *Science in China (Series D)* **27**, 289–293 (in Chinese).

Zhang, Z. C., Mahoney, J. J., Mao, J. W. & Wang, F. H. (2006). Geochemistry of picritic and associated basalt flows of the western Emeishan flood basalt province, China. *Journal of Petrology* **47**, 1997–2019.

Zhao, Z. D., Mo, X. X., Dilek, Y., Niu, Y. L., DePaolo, D. J., Robinson, P., Zhu, D. C., Sun, C. G., Dong, G. C., Zhou, S., Luo, Z. H. & Hou, Z. Q. (2009). Geochemical and Sr–Nd–Pb–O isotopic compositions of the post-collisional ultrapotassic magmatism in SW Tibet: Petrogenesis and implications for India intra-continental subduction beneath southern Tibet. *Lithos* **113**, 190–212.

Zhong, D., Ding, L., Liu, F., Liu, J., Zhang, J., Ji, J. & Chen, H. (2000). Multi-directional bedding-form structures of lithosphere in orogenic belt and its constraint to Cenozoic magmatic activity—for example in Sanjiang and its adjacent area. *Science in China* **30(supplement)**, 1–8 (in Chinese).

Zhu, B. Q., Zhang, Y. Q. & Xie, Y. W. (1992). Nd, Sr and Pb isotopic chracteristics of Cenozoic ultra-potassic volcanic rocks from eastern Erhai, Yunnan and their implications for subcontinent-mantle evolution in southwest China. *Geochimica* **21**, 201–212 (in Chinese with English abstract).

Zindler, A. & Hart, S. (1986). Chemical geodynamics. *Annual Review of Earth and Planetary Sciences* **14**, 493–571.

Downloaded from https://academic.oup.com/petrology/article/51/8/1617/1456692 by U.S. Department of Justice user on 17 August 2022